Università degli Studi di Firenze

Dipartimento di Fisica

Scuola di Dottorato in Scienze

High-resolution optical spectroscopy of state-of-the-art GaN-based nanostructures

Flavian Stokker-Cheregi

Tesi di Dottorato di Ricerca in Fisica

XXI ciclo

Il Candidato

Flavian Stokker-Cheregi

. . . . . .

Il Supervisore

Prof. Anna Vinattieri

. . . . . .

Il Coordinatore

Prof. Alessandro Cuccoli

. . . . . .

Firenze

2008

Contents

Introduction iii

1. Properties of GaN and related nanostructures 1

1.1. Structural properties of the nitride family of semiconductors 1

1.2. Excitonic properties of bulk GaN 4

1.3. Properties of GaN based heterostructures 9

1.3.1. The qunatum well 10

1.3.2. Strain related effects: the polarization in *wurtzite* nitride semiconductors 13

1.4. Conclusions of the chapter 18

2. Microcavities in the strong coupling regime 19

2.1. The Fabry-Pérot resonator 19

2.2. The transfer matrix formalism 23

2.3. Semiconductor microcavities 27

2.4. Polaritons and the strong coupling regime 34

2.5. Bose-Einstein condensation of polaritons 41

2.6. Conclusions of the chapter 42

3. Growth related issues 43

3.1. The growth of III-nitride heterostructures 43

3.2. The influence of strain on the design of III-nitride heterostructures 45

3.3. Conclusions of the chapter 48

4. Experimental systems 49

4.1. Reflectivity 49

4.2. Photoluminescence 50

4.3. Experimental setups 57

5. Bulk GaN microcavities and related structures 62
5.1. The GaN epilayer 62
5.2. The DBR (sample 703) 68
5.3. The half cavity (sample 808hc) 70
5.4. The weak coupling 74
5.5. The strong coupling 78
5.5.1. Thermalization issues 83
5.5.2. Suppression of the relaxation bottleneck 86
5.6. Conclusions of the chapter 91

6. Optical properties of state-of-the-art GaN/AlGaN quantum wells 93
6.1. Description of samples 93
6.2. Recombination kinetics of biexcitons 94
6.3. Impact of quantum confinement and QCSE on biexciton binding energy . . 104
6.4. *B* exciton recombination kinetics and impact of quantum confinement on *A* and *B* exciton energy splitting 110
6.5. Conclusions of the chapter 116

7. Conclusions 117

Acknowledgements 123

List of abbreviations 124

References 125

Introduction

Optoelectronics witnessed a remarkable progress during the last few decades, particularly in the fields of information technology and telecommunications. The continuous need to transmit and process increasing amounts of information faster than before drove researchers to seek new physical concepts and to develop new environments that suited these needs. Traditional silicon and metal based electronic components were found to pose certain physical limitations. The maximal vibration frequency of an electron in a semiconductor (in the microwave range) limits the capacity to modulate carrier waves without creating too much interference between different transmission channels, which restrains their applicability. On the other hand the photon, a charge free and mass free particle, can carry information faster and further, which is the reason why novel emitters and receivers use photons to transmit information through optical media. The technological advances achieved during this time allowed fabrication of more complex structures that can control the light - matter interaction in semiconductor materials. This is how the first semiconductor lasers were made in the 70s. The fundamental issues that researchers sought to improve when designing new lasers were: tunability, efficiency, and brilliance. However, the control of the electron - hole spatial separation proved to be a difficult task. In fact, one of the deficiencies of bulk materials is that they exhibit numerous non-radiative recombination channels (phonons, material defects, impurities etc.). A solution to this was sought by trying to spatially confine carriers in bidimensional structures called quantum wells. The electron - hole spatial separation is thus recovered, and the radiative recombination rate is increased. Following the same logic, uni-dimensional (quantum wires) and zero-dimensional (quantum dots) structures were created. Unfortunately, these devices were not as successful as their predecessors. The reasons for this deficiency are of technological, as well as physical nature. On one hand, using modern industrial technologies, the uncertainty on the dimensions of such nanometrical systems is comparable to their size. Thus, the strong energy dispersion cancels out the improvements achieved through spatial confinement. On the other hand, the argument for the use of low dimensionality structures is the change in the density of states, which translates not only in a better control of the spatial charge separation, but also an increased control of their energies. This argument is valid up to the point where we consider the presence of Coulomb interactions between carriers, which are inevitable in such nanostructures. As a result, the

attained densities of states are not as 'sharp' as predicted by theory. Finally, these structures are considered to less viable than their predecessors on an industrial scale. At the beginning of 1980's, another idea emerged: in order to optimize the light-matter interaction, the spatial separation of carriers is not the only element that should be taken into account. In fact, the light emission phenomenon in a semiconductor material is a three-body problem: an electron, a hole, and a photon. Hence, the idea is to equally confine the photon, as well as the carriers, by using a cavity of micrometrical dimensions. These structures are now referred to as *microcavities*. By mixing the confinement of the electromagnetic field with the carrier confinement, a quantum well based microcavity is created. This idea was behind the creation of VCSELs[1] (Vertical Cavity Surface Emitting Laser). The vertical cavity laser has many advantages over the 'classical' quantum well laser, such as a single-mode working regime due to the reduced cavity length (1 μm compared to the 500 μm of a standard quantum well laser). Moreover, the very small cone of emission leads to a reduced divergence of the beam allowing an easier coupling of the device to an optical fiber. Nevertheless, in this case no modification or control of the light - matter interaction can be achieved.

A strong modification of light - matter interaction, well known in atomic physics, is obtained in the *strong coupling* regime when an atom interacts with an electromagnetic field in a cavity. As long as the interaction between an atom and the electromagnetic field overcomes their coherence times, eigenstates of the atom + cavity system are obtained, which are mixed atom-photon states. A similar regime was first observed in 1992 in quantum well semiconductor microcavities (GaAs/AlAs based) by Claude Weisbuch *et al.* [1]. The idea behind the strong coupling in a semiconductor quantum well based microcavity is that we can consider it as a two level system. On one hand, the spatial confinement of carriers, bound by the Coulomb interaction, creates the exciton state. On the other hand, the confinement of the electromagnetic field due to the presence of the microcavity originates a principal photon mode. The translational invariance of the system gives rise to selection rules, in strict analogy with a system with two coupled levels. It is thus possible to obtain a strong coupling regime in which a perfect mix occurs between the exciton and photon states. These new eigenstates are referred to as *cavity polaritons*, and they are bosonic in nature. Because of this coupling, polaritons with a high photon fraction are less sensitive to phonon interaction than excitons, and have a very small in-plane mass, 4 to 5 orders of magnitude smaller than that of bare excitons, which results in an extremely low density of states. Finally, the lifetime of polaritons

[1] The first realization of a VCSEL with practical use was in 1988.

can be controlled by adjusting the cavity losses, i. e. the mirror reflectivity. For reflectivities of 96% - 98%, the lifetime turns out to be of the order of 1 ps, which suggests the possibility to fabricate ultra-fast devices.

Opening a new research field in physics, the strong coupling regime in semiconductor microcavities has been the subject of numerous studies during the last few decades. Thanks to the expertise on growth and fabrication of GaAs/AlAs based VCSELs acquired in the past, it is easy to understand why the first and most exhaustive studies on this topic were focused on III-V based (GaAs/AlAs, in particular) quantum well microcavities. These studies have focused on: the effect of structural inhomogeneities in the strong coupling regime [2], the measurement of the polariton dispersion [3], the optimization of the structures [4], the photoluminescence mechanisms [5] - [7], the polariton dynamics in microcavities [8] - [13].

Investigations of the recombination dynamics in the strong coupling regime showed that the relaxation of polaritons after a non-resonant excitation was not as fast as it was predicted to be. In fact, the strong dispersion of polaritons in the quantum well plane slowed their relaxation up to a few hundreds of picoseconds [9] [10] [13], giving rise to an energy interval where excitons would accumulate. Nevertheless, taking advantage of the bosonic nature of polaritons, there is a way to overcome this accumulation phenomenon, by stimulating the relaxation. This phenomenon, known as the 'Boser' effect, was described by A. Imamoglu *et al*. in 1996 [14]. It was this effect that drove the interest of the scientific community to produce a new generation of parametric optical amplifiers and ultra-low threshold lasers [15] based on the stimulated scattering of polaritons [16]. These devices are commonly referred to as *'polariton lasers'*.

GaAs based microcavities were the first structures considered for the realization of the polariton laser due to the advanced knowledge and higher optical quality of this system. However, studies have shown that, in the case of non-resonant optical excitation, acoustic phonon scattering rates from high wave vector (k) exciton states into polariton states with wave vectors corresponding to the strong coupling regime ($k \leq 5\text{-}6 \times 10^4$ cm^{-1}) are small due to the large energy transfer required compared to the typical acoustic phonon energies of 1 meV. Furthermore, the strongly coupled states have very short radiative lifetime (~1 ps) due to their high photon fraction, thus leading to a non-thermal polariton population and the occurrence of a relaxation bottleneck [17] [18]. Trying to overcome this bottleneck by increasing excitation densities in order to stimulate exciton - exciton scattering resulted in the collapse of strong coupling, and the achievement of conventional photon lasing (VCSEL) [19] [20]. A suppression of the relaxation bottleneck in GaAs based quantum well microcavities

was achieved by using both resonant and non-resonant excitation [21], but this result is of little practical use. Polariton lasing was demonstrated only recently on the discrete modes of a GaAs/GaAlAs micropillar cavity, but this result is limited to cryogenic temperatures (10 K) [22]. In fact, in spite of their very high optical quality, the ability of GaAs based systems to operate only at low temperatures is a limiting factor due to which they are currently disregarded as potential candidates for the realization of a practical polariton laser.

A suppression of the polariton relaxation bottleneck was achieved in II-VI microcavities [23] due to the increased exciton binding energy and oscillator strength. These properties allowed the observation of more pronounced strong coupling effects with respect to the III-V structures, which made these materials better candidates for the observation of a 'Boser' effect. In fact, the achievement of a polariton Bose - Einstein condensate above a threshold in non-resonant excitation in a CdTe based quantum well microcavity was demonstrated in 2006 by Kasprzak *et al.* [24], but, again, the functionality of these structures is still limited to cryogenic temperatures.

As the ability to operate at room temperature seems to be one of the main requirements for a polariton laser, scientists have looked towards other materials that would allow polariton lasing at "normal" temperatures. In this context, the nitride family of materials (GaN, AlN, InN, and their alloys) emerged as very good candidates to achieve such a goal due to the increased exciton binding energy (> 30 meV in low Al content narrow GaN/AlGaN quantum wells [25]), with respect to the materials discussed before. Such binding energies allow not only the observation of stable excitons in photoluminescence spectra at room temperatures and beyond, but also a more pronounced strong coupling with the electromagnetic field, suggesting a GaN based quantum well microcavity as the ideal system for the realization of a polariton laser operating at room temperature [26]. Other advantages of nitrides include high oscillator strengths, the ability to control the n-type and p-type doping, and more importantly the wide range tunability by modification of the alloy composition in order to cover the entire UV - visible spectrum. Nevertheless, given their remarkable excitonic properties, why wasn't a nitride based heterostructure used from the very start to realize a polariton laser? The answer is very one sided: GaN related heterostructures were not considered initially for this end because of a lack of technology and *know-how* on the actual growth of high quality nitride heterostructures. GaN based nanostructures are at the basis of large classes of blue and ultraviolet optoelectronic devices since the early 1990s [27]. Although these devices exhibit impressive performances, in depth physical studies have been hindered by their poor optical quality, which is far from being ideal. The lattice mismatch between standard substrates and

heteroepitaxially grown materials produces structural defects with a density 6 orders of magnitude larger than in their GaAs counterparts [28]. Consequently, the concentration of non-radiative centers in nitrides is non-negligible [29], thus reducing the recombination lifetime. In fact, even for GaAs based quantum well microcavities, several years were needed to achieve a satisfactory sample quality [30]. In the case of GaN quantum wells, large inhomogeneous broadening of the optical spectra is also usually observed as a consequence of strain, interface, and alloy fluctuations [31]. Finally, the quantum confined Stark effect associated with the huge piezo and spontaneous polarization fields reduces the radiative recombination rate and, eventually, may even inhibit the excitonic recombination [32]. All these limiting factors had to be overcome by the evolution of growth technology in order for GaN based microcavities to be considered as potential candidates for the realization of a polariton laser.

In this thesis I will present results obtained through high-resolution optical spectroscopy measurements that relate directly to the evolution of GaN based nanostructures, in view of the achievement of a nitride based room temperature polariton laser. In fact, during my Ph.D. thesis, I had the opportunity of participating in a European project with this main objective. Therefore, my results illustrate the improvements made by the growers in achieving more complete and higher quality heterostructures.

Chapter §1 discusses general structural and optical properties of nitrides, with a special emphasis GaN based nanostructure. Chapter §2 is an overview of microcavities and the strong coupling regime. Growth issues related to the nanostructures described in chapters §5 and §6 are discussed in Chapter §3. The various experimental techniques that were used to investigate the samples are presented in Chapter §4. As the technological deficiencies related to the growth of GaN quantum wells would have out weighted the theoretical benefits of a better carrier confinement and increased exciton binding energy, it was the growers' decision to use bulk GaN as active medium inside the microcavities at this stage, rather than quantum wells. The evolution of bulk GaN semiconductor microcavities, from weak coupling to strong coupling, is presented in Chapter §5. Chapter §6 presents results on state-of-the-art GaN/AlGaN quantum wells with low Al content in the barriers that are expected to be used as active media in a next generation of microcavities. Owing to their improved optical qualities, with respect to previous samples, these quantum wells offer insight on physical phenomena that could not be previously observed in similar samples.

1. Properties of GaN and related nanostructures

This chapter will be devoted to the review of the main structural and optical properties of nitrides, with a special emphasis on GaN related materials and nanostructures that will be discussed in this work. We will start with a general overview of the fundamental properties of the nitride family (section §1.1), after which we will focus on the excitonic properties of bulk GaN (section §1.2). Issues related to the structural properties of GaN related heterostructures will be expanded in section §1.3.

1.1. Structural properties of the nitride family of semiconductors

The group III nitrides can be synthesized in two different stable lattice structures: the *wurtzite* and the *zinc-blende* structure. The terms *hexagonal* and *cubic*, respectively, are commonly used when referring to these crystal symmetries. *Wurtzite* and *zinc-blende* lattices are shown in Fig. 1.1.

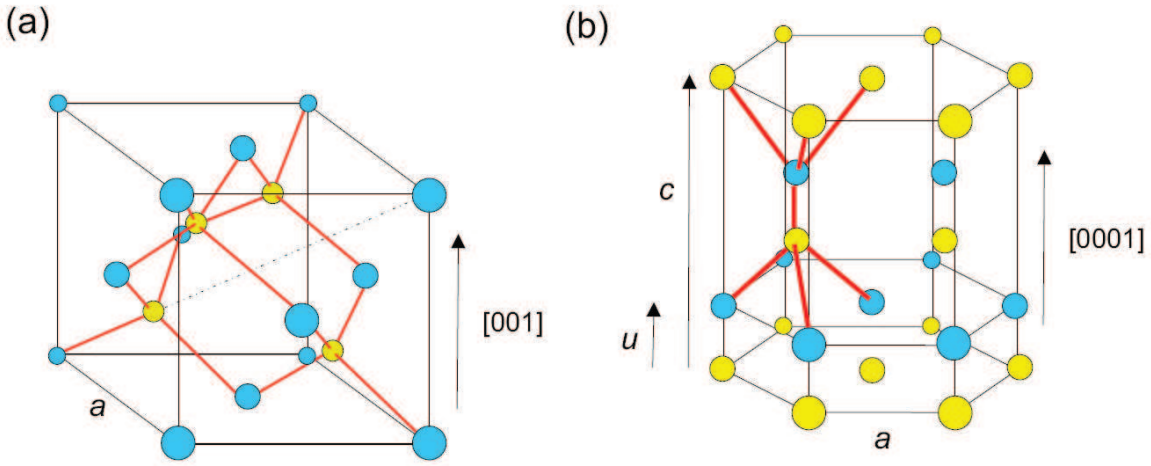

Figure 1.1. (a) Cubic *zinc-blende* and (b) hexagonal *wurtzite* structure.

The *zinc-blende* structure, shown if Fig. 1.1 (a), is constituted of two face centered cubic sub-lattices, each one made up by atoms of the group III or V, that are shifted of the quantity $a/4$ along the main diagonal, where a is the cube side. As a result, one atom of the group III is coordinated with four atoms of the group V, and vice versa, in a tetrahedral

arrangement, as in the well known diamond crystal. In this way, the three lattice directions [100], [010], and [001] are equivalent.

The *wurtzite* structure, shown in Fig. 1.1. (b), can be viewed as a series of alternating layers of group III and group V atoms, with in-plane hexagonal arrangement. Each atomic layer, with the hexagon side *a*, is facing a corresponding layer made up by atoms of the other group and located at a distance *u*. Each couple of planes is shifted respect to the neighbouring couple to reproduce a periodic structure, with period *c*, along the [0001] direction orthogonal to the hexagonal planes. As in the case of the *zinc-blende*, each atom is linked with four atoms of the other atomic type in a tetrahedral arrangement, except the tetrahedron is not regular in the case of a *wurtzite*, and two lattice constant, *a* and *c*, are necessary in order to describe it. GaN, InN, AlN, and their alloys can crystallize in both *wurtzite* and *zinc-blende* lattice forms, and the corresponding band structures are quite distinct due to differences in the underlying symmetries.

The main parameter that determines the optical and electronic properties of a massive (*bulk*) semiconductor is represented by the energy difference (E_g) between the top of the valence band (*VB*) and the bottom of the conduction band (*CB*), a region which is known as the *forbidden band*. In an ideal semiconductor, this band is not allowed to be populated by electrons, and the value of E_g is termed *energy gap* or *band gap*.

The band gap values for GaN, AlN, and InN have been extensively studied. The work of I. Vurgaftman and J. R. Meyer [33] is a comprehensive review of band parameters for all nitrogen-containing III-V semiconductors. The values recommended by the authors have suffered little modifications ever since. Figure 1.2 depicts energy gap values at T = 0 K for the *wurtzite* and *zinc-blende* nitride semiconductors as a function of the lattice constant, according to ref. [33].

When considering uniform ternary alloys of the type $A_xB_{1-x}C$, where *x* is the molar fraction of *A* with respect to the total molar fraction of *A* + *B* in the ternary compound, Vegard's law is a straightforward approximation used to determine a physical property *P* as the linear interpolation between the values of this property of the two binary compounds *AC* and *BC*. So we have:

$$P(A_xB_{1-x}C) = xP_{AC} + (1-x)P_{BC} \tag{1}$$

This relation holds quite well for most of the structural and mechanical parameters, but in some cases it is not satisfactory. In fact, big deviations from the linear behaviour are observed for some important physical properties, such as the band gap. For the ternary alloys AlGaN, GaInN, and AlInN, the band gap dependence is assumed to follow the simple quadratic form:

$$E_g\left(A_xB_{1-x}C\right) = xE_g\left(AC\right) + \left(1-x\right)E_g\left(BC\right) - x\left(1-x\right)b\,, \tag{2}$$

where the so-called bowing parameter b accounts for the deviation from a linear interpolation between the two binary compounds AC and BC.

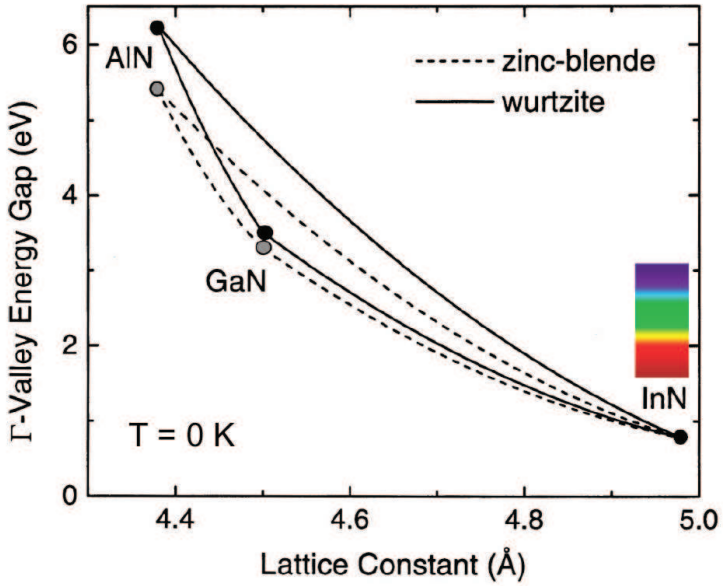

Figure 1.2. Energy gap values at T = 0 K of wurtzite (solid curves) and zinc-blende (dashed) nitride semiconductor alloys and binaries (points), as a function of lattice constant, reproduced from [33]. The visible spectrum energy interval is also represented.

The bowing parameter is always positive for these materials, which reflects a reduction of the alloy energy gaps with respect to Vegard's law. The bowing effect is clearly evident in the curves connecting the binary end points. The reason of the non linear behaviour expressed in eq. (2) can be mainly attributed to the existence of local strain due to mismatch between the AC and BC compounds. Extensive experimental and theoretical studies have been devoted to the determination of the bowing factor b [33], and usually a linear interpolation of the existing measurements on the energy gaps of various ternary alloys with different x is employed.

The temperature dependence of the energy gap of GaN, AlN, and InN can be parameterized using the commonly employed Varshni formula [33]:

$$E_g(T) = E_{g0} - \frac{\alpha T^2}{T + \beta}\ , \tag{3}$$

where E_{g0} is the value of the energy gap at T = 0 K, and α and β are the so-called *Varshni coefficients* related to the specific semiconductor.

In the following, our discussions will focus on the *wurtzite* structure, as this was the symmetry of choice for the samples discussed in this thesis. Table 1.1 summarizes some of the main structural parameters of the *wurtzite* nitride binaries discussed so far: the elementary cell parameters a, c, and u, the energy gaps E_g, and the Varshni coefficients α and β, following ref. [33].

Parameters	GaN	AlN	InN
a (Å) at T = 300 K	3.189	3.112	3.545
c (Å) at T = 300 K	5.185	4.982	5.703
u (Å) at T = 300 K*	0.376	0.38	0.377
E_g (eV) at T = 0 K	3.51	6.25	0.78
α (meV/K)	0.909	1.799	0.245
β (K)	830	1462	624

Table 1.1. Band structure parameters for wurtzite nitride binaries, as recommended by ref. [33]. (*) Taken from ref. [34].

1.2. Excitonic properties of bulk GaN

In general, the optical transitions in semiconductors are the result of a process in which a hole and an electron are created (recombine) as a result of the absorption (emission) of a photon. The excited carriers in the lattice are relatively free to move, although they still interact with the lattice background made up by the ionized and neutral atoms. Such interaction is defined in the shape of the conduction and valence bands, and it plays a fundamental role in the determination of the recombination and absorption dynamics. In a simplified picture, the influence of the lattice on carriers is represented by means of the

introduction of electron and hole *effective masses* that are related to the band curvature at the $\vec{k}$ transition. For direct band gap semiconductors, with non-degenerate and isotropic bands, the dispersions of the valence and conduction bands are approximated as being parabolic. This approximation is satisfactory in the vicinity of the Brillouin zone center ($\vec{k} = 0$).

Band structure of GaN

The band structure for *wurtzite* GaN is represented in Fig. 1.3.

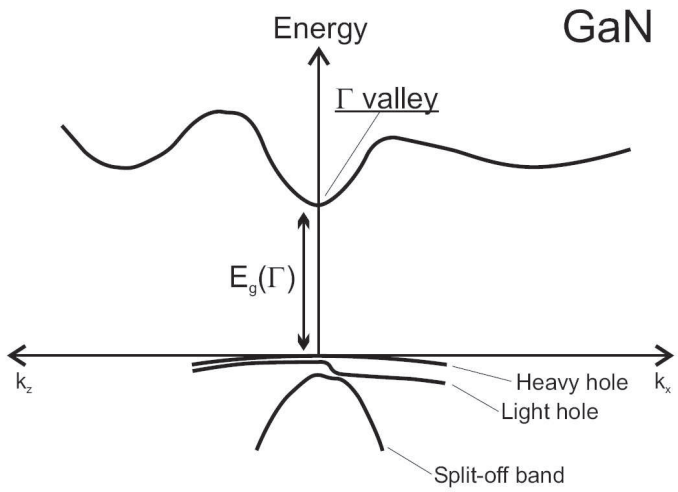

Figure 1.3. Illustration of the band structure of GaN.

GaN, as well as the other nitrides in the *wurtzite* phase, presents a direct band gap structure, in which the minimum of the conduction band and the maximum of the valence band occur at the Γ point in the $\vec{k}$ space. In a direct band gap semiconductor, the absorption (emission) of light requires energy and momentum conservation between the photon and the electron in the valence (conduction) band. Due to the fact that the photon momentum, $\vec{k}_0$, in the visible range is of the order of 10^4 cm^{-1}, negligible with respect to the extreme of the Brillouin zone ($10^7 \div 10^8$ cm^{-1}), the optical transition is almost vertical. Therefore, direct band gap semiconductors are more efficient concerning radiative recombinations with respect to indirect band gap ones.

The Coulomb interaction between the excited electron and hole gives rise to the formation of bound electron-hole pairs. These two-particle systems, called *excitons*, lead to sharp optical features that appear at an energy equal to the carrier-carrier transition energy diminished by the electron-hole binding energy E_b^x, also known as *exciton binding energy* (see Fig. 1.4).

Excitons can be described in two limit cases: *Frenkel excitons* and *Wannier-Mott excitons* (or simply *Wannier*) [35]. The first case is that in which there is a strong attractive force between electron and hole (e. g. ionic crystals), and there is a strong binding force between the two particles within the same unit cell, or within the adjacent cells at most [35]. We shall not discuss this case however, and we will focus on the Wannier excitons, which are typical for most III-V semiconductors. In this case, the Coulomb interaction between electron and hole is screened by the polarization of the medium that surrounds the charges, caused by all the virtual transitions of the excited states. As a result, electrons and holes are weakly bound, and separated by a distance of the order ten times the lattice constants.

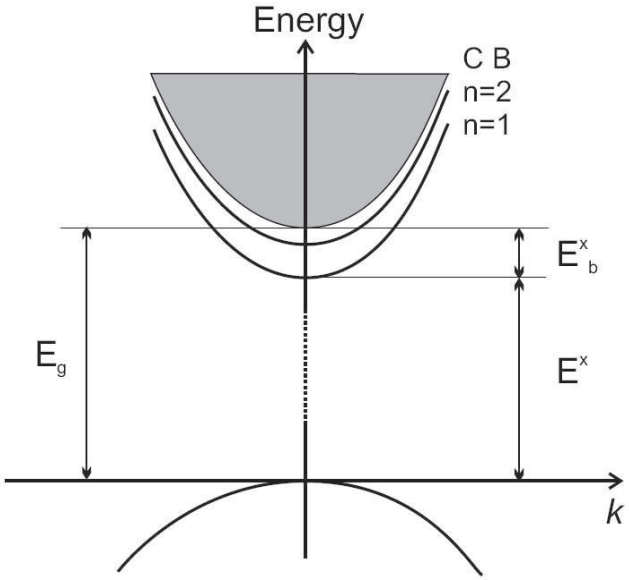

Figure 1.4. Schematic representation of the excitonic levels.

A simple model to describe Wannier excitons is the hydrogen atom model, leading to a discrete levels structure, so that the excitonic transition energy at $k = 0$ is given by [36]:

$$E_n^x = E_g - E_b^x \frac{1}{n^2} \qquad E_b^x = 13.6eV \frac{\mu}{\varepsilon^2}, \tag{4}$$

where n is the principal quantum number, $\mu = \mu_e \mu_h / (\mu_e + \mu_h)$ is the reduced mass, with μ_e and μ_h the electron and hole effective masses in mass units, respectively, and ε is the dielectric constant (typically $\varepsilon \sim 10$ in the case of semiconductors). Similarly, the excitonic radius is given by:

$$r^x \cong 0.53\text{Å}\frac{\varepsilon}{\mu} \tag{5}$$

Free excitons

The case discussed above is a simplified model which assumes non-degenerate conduction and valence bands. The case of GaN is more complex however, because even though in the Γ point the conduction band is indeed non-degenerate, the valence band is more complex because of the perturbation generated by the crystal field (Δ_{cf}) and the spin-orbit interaction (Δ_{so}), as depicted in Fig. 1.5.

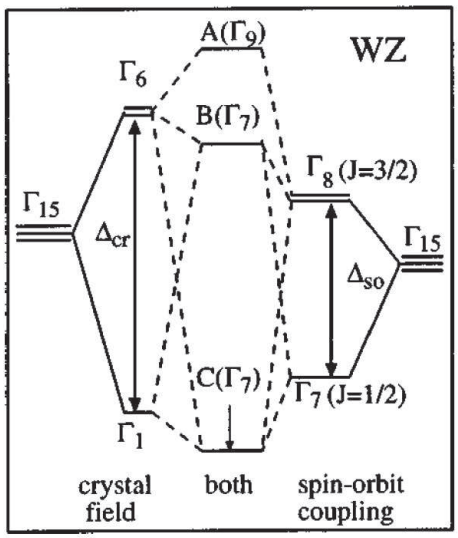

Figure 1.5. Effect of crystal field splitting and spin-orbit coupling on the valence band (near the Γ point) of wurtzite GaN [37]. At $k = 0$, the valence band is split by the combined action of crystal field and spin-orbit coupling into $A(\Gamma_9)$, $B(\Gamma_7)$, and $C(\Gamma_7)$ states.

The radiative recombinations between the electrons in the conduction band (Γ_7) and the holes in the three valence band states Γ_9 (or *HH*, as it is associated to a heavy hole state), Γ_7 (or *LH*, as it is associated to a light hole), and Γ_7 (*CH* - associated to the presence of the crystal field) give rise to the formation of three excitonic transitions termed *A*, *B*, and *C*, respectively, in the order of their increasing energy. For bulk GaN, the electron effective mass is $m_e = 0.2m_0$ [33], while the value obtained for the average "bare" hole mass is $m_h = 0.476m_0$ [38], where m_0 is the free electron mass. However, due to the crystal field splitting and spin-orbit interaction, m_h assumes different values for each of the valence bands that can be calculated using Luttinger parameters [38].

Usually, the recombination of the *A* exciton is the most prominent, while that of the *C* exciton is the weakest. Owing to an uncertainty in the hole mass, the theoretical range for the

A exciton binding energy in bulk GaN is 23-28 meV [39], values that have been largely retrieved by experimental groups [33]. This value, to be compared to that of 5 meV of GaAs [36], assures its stability even at room temperature, and it is the main reason why GaN related structures are so interesting for practical purposes.

Bound excitons

Although the *A*, *B*, and *C* excitons are systems made up by two bound particles, they can however move freely in the sample plane, which is the reason why they are described as being *free excitons*. In general, in the band gap energy region, apart from the free exciton recombination, there are also other recombinations possible which have an extrinsic character. Such recombinations are those of the *bound excitons*. In this case, one of the two particles that makes up the free exciton can interact with an impurity or an imperfection of the crystalline lattice. Due to this interaction, the exciton remains confined in a region which is close to the defect, and hence a bound exciton is formed. For instance, one of the most common situations encountered for GaN layers is that in which an exciton can interact with a neutral donor (acceptor), so that the electron (hole) remains bound to the impurity; in such a case we have a so called *donor bound exciton* DBE (*acceptor bound exciton* ABE) [40] - [42].

The presence of defects in the material and the subsequent formation of bound excitons, leads to the appearance of new optical transitions, at lower energies than the free exciton to which they are associated. This energy difference accounts for the localization energy of the exciton and depends on the specific defect.

Biexcitons

Besides from being a two-particle bound system, being delocalized in an ideal crystal, and exhibiting a sharp optical transition, free excitons are similar to an atomic gas also in the sense that they can interact with each other to produce exciton molecules, also known as *biexcitons*. Biexcitons, however, are extremely sensitive to structural disorder, as the presence of disorder in the sample causes the excitons to localize before any further interaction between them is possible. In order for biexcitons to form, the rate at which free excitons localize must be reduced as much as possible, and this can only be achieved by increasing the optical quality of the sample. Therefore, the presence of a biexcitonic recombination in a semiconductor structure is considered a 'trademark' of its high optical quality, which is the reason why the study of biexcitons will be one of the main foci of chapter §6.

Line broadening

A very important aspect in our study of the excitonic transitions is the spectral broadening of the absorption and recombination bands. Generally, two types of broadening mechanisms can be distinguished: the *homogeneous broadening* and the *inhomogeneous broadening*. The homogeneous broadening is related to the interaction between excitons and phonons. When considering the contribution of acoustic phonons, dominant at high T, the broadening is proportional to k_BT; hence, it increases with temperature. The homogeneous contribution can be accounted for by considering a Lorentzian distribution of states. On the other hand, the inhomogeneous broadening is associated to various defects that can be present in the crystalline lattice, such as strain related defects, impurities, and variations of material composition. Its contribution can be accounted for assuming a Gaussian line shape; it is temperature independent and therefore, when both inhomogeneous and homogeneous broadenings contribute to the line shape, the weight of the inhomogeneous part tends to diminish with increasing temperature [43].

1.3. Properties of GaN based heterostructures

The production of semiconductor based devices needs the realization of different semiconductor, conductor and insulating layers. The design and realization of these structures needs the comprehension of the effects derived by the presence of interfaces between materials with different lattice constants, lattice symmetry and, in general, different optical and electronic properties. Although the investigation of these effects is beyond the objectives of this thesis, they have a huge impact on the data presented in chapters §5 and §6, which is why we chose to give a description of these effects in this section.

A semiconductor heterostructure is obtained when different semiconductor materials are grown successively on the same substrate. The required lattice symmetry for a nitride heterostructure can be induced by the choice of an appropriate, hexagonal or cubic, growth substrate. For III-nitrides semiconductors, and for the samples discussed in chapters §5 and §6 in particular, the *wurtzite* structure can be obtained for instance by growing on the (001) plane of a Sapphire crystal (Al_2O_3) or the (111) plane of a Silicon crystal. Due to a lattice mismatch between the layers that make up the heterostructure (see Fig. 1.2), as well as the substrate itself and these layers, mechanical strain is accumulated at the interfaces between different

materials. The effects of strain are addressed in more detail in section §1.3.2, while in section §1.3.1 these effects are largely neglected, and the emphasis is placed on illustrating the effects of quantum confinement.

1.3.1 The quantum well

The sequential growth of different semiconductor materials results in a structure whose conduction and valence band profiles vary with position along the growth direction. The single *quantum well* structure (studied in chapter §6) is obtained by the growth of a thin layer of a certain semiconductor material between two other layers, called *barriers*, with higher band gaps. In this work we will refer to the so-called type-I quantum well, where the small band gap material (*A*) has both its electron and hole levels confined by a wider band gap material (*B*) [44]. The Hamiltonian for the electron (hole) contains an additional term due to the confinement potential. As a consequence of the break of the symmetry along the growth direction, the optical and electronic properties of the structure change substantially with respect to that of the massive constituents. In particular, transition energies blue shift and the radiative efficiency is increased.

The energy levels in the conduction band can be calculated quite easily in the *approximation of the envelope function* [45], using a Kane model [46] for describing the electron and hole states of the parent *A* and *B* materials [47]. It can be shown [45] that the electron wave function takes approximately the form:

$$\psi = \sum_{A,B} e^{i\vec{k}_\perp \cdot \vec{r}} u_{c\vec{k}}^{A,B}(\vec{r}) \chi_n(z), \tag{6}$$

where z is the growth direction, $\vec{k}_\perp$ is the transverse electron wave vector, $u_{c\vec{k}}(\vec{r})$ is the Bloch wave function in the *A* or *B* material, assumed equal for *A* and *B*, and $\chi_n(z)$ is the envelope wavefunction, which satisfies the Schrödinger-like equation [45]:

$$\left(-\frac{\hbar^2}{2m^*(z)} \frac{\partial^2}{\partial z^2} + V_c(z) \right) \chi_n(z) = \varepsilon_n \chi_n(z), \tag{7}$$

where $m^*(z)$ is the electron effective mass of the *A* or *B* material, $V_c(z)$ represents the energy level of the bottom of the conduction bands, and ε_n is the so-called confinement energy of the carriers. Moreover, the continuity conditions at the interfaces are that $\chi_n(z)$ and $[1/m^*(z)][\partial\chi_n(z)/\partial z]$ should be continuous.

Fig. 1.6 is a schematized reproduction of an 'ideal' single symmetric quantum well (QW) of type-I, in which strain effects are ignored, and hence the electrons and holes are confined in the same semiconductor slab.

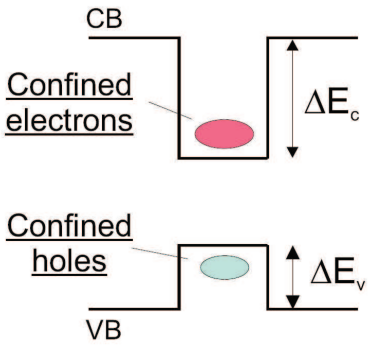

Figure 1.6. Schematized representation of a single symmetric quantum well.

The definition of the band profile in the growth direction requires the knowledge of the conduction band discontinuity ΔE_c (or equivalently the ΔE_v) at the well-barrier interface. Usually, this quantity is given in terms of the ratio *f* between ΔE_v and the difference between the gaps:

$$f = \frac{\Delta E_v}{\Delta E_g} \tag{8}$$

The different alignment of the conduction and valence bands depends on a variety of factors, such as the chemical potentials of the two facing materials, whose value depends on the doping in the sample. The determination of *f* can be quite difficult because of the fact that very often it depends on the particular sample and the unintentional doping due to substitutional impurities or other defects of the crystalline lattice incorporated during the growth. Also, strain affects the band alignment, and in the case of interest, for a GaN/AlN interface, the value of *f* was calculated to be around 0.3 [48].

The quantum well structure provides a 1-dimensional (1D) confinement in the growth direction, leaving electrons and holes free to move in the growth plane. We will not discuss

other cases where further reductions of the dimensionality of the confining structure lead to *quantum wire* and *quantum dot* structures that provide 2D and 3D confinement, respectively.

The reduction of the number of degrees of freedom of carriers strongly modifies the optical and electronic properties of the structure. In particular, the modification of the *density of states* (DOS) can lead to the creation of a series of discrete energy levels.

In Fig. 1.7 the density of states is schematized for the *bulk* (0D confinement,) and the *quantum well* (1D confinement).

In general, the reduction of dimensionality produces an enhancement of the singularities of the density of states as a function of the carrier energy E. The reduction of the degrees of freedom from 3 to 2 makes the density of states change from $(E - E_g)^{1/2}$ to a step function given by $n\theta(E - E_n)$, where $\theta(E)$ is the Heavyside function, and n identifies the n-th excited state with energy E_n. The quantity $E_n - E_g$ is the *confinement energy* of the electron. An analogous definition holds for the hole in the valence band.

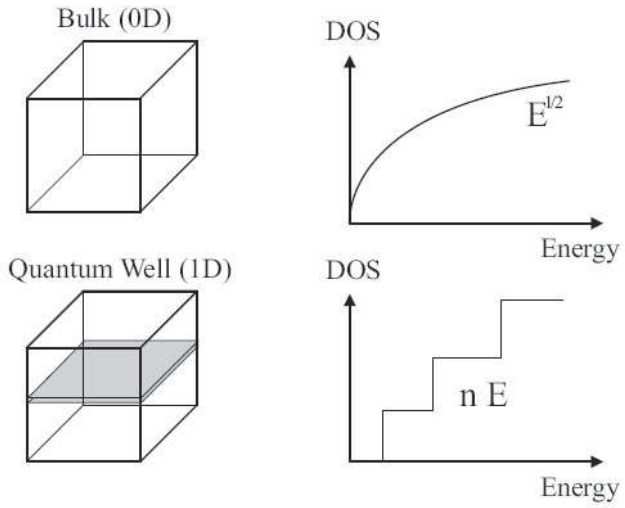

Figure 1.7. Schematic representation of the density of states for 0D (bulk) and1D (quantum well).

The following relations report the energy dependence for the density of states $D(\omega)$ for the two confinements considered here:

$$\text{bulk:} \quad D(E) \propto (E - E_n)^{1/2} \tag{9}$$

$$\text{well:} \quad D(E) \propto n\theta(E - E_n) \tag{10}$$

Since the density of states is involved in the optical transition probability, which determines the radiative efficiency and the spectral features of the absorption and emission of

light, the quantum confinement turns out to deeply modify the carrier behaviour and the properties of the semiconductor heterostructures. In a massive semiconductor, the energy threshold for light absorption is simply given by the energy gap E_g. The introduction of a spatial confinement increases the transition energy, and a series of E_n bands are obtained, with $n = 1$ corresponding to the band with the lowest energy.

The density of states of each excitonic branch, numbered n = 1, 2..., follows substantially the behaviour of the bulk density shown in Fig. 1.7. This remains true when introducing a quantum confinement. The density of states shown in Fig. 1.7 for each confining structure is simply applied to each excitonic branch. Concerning the excitonic transition energy at the bottom of the excitonic band (namely at $\vec{k} = 0$), the interdiction of one degree of freedom, in the limit of a perfectly 2-dimensional quantum well with infinite barriers and well width tending to zero, introduces the following changes:

$$\text{bulk:} \quad E_n^x = E_g - E_b^x \frac{1}{n^2} \qquad \text{well:} \quad E_n^x = E_g + E_C - E_b^x \frac{1}{(n-1/2)^2}, \tag{11}$$

with E_C being the confinement energy. For the first excitonic level (n=1) this implies an increase of the exciton binding energy of a factor 4. However, as it will be seen in chapter §6, in the case of a quantum well with finite width and finite barrier height that is also subject to strain effects, this increase is much smaller.

1.3.2. Strain related effects: the polarization in *wurtzite* nitride heterostructures

Although a rigorous analysis of strain is beyond the scope of this thesis, its presence in GaN based heterostructures is without a doubt the biggest limiting factor that prevents the achievement of samples with an optical quality equivalent to their GaAs counterparts. Hence, a qualitative description of the most important strain related effects will be given in this subsection.

The presence of strain due to lattice mismatch can influence the optical and electrical properties of the material in many ways. The growth of a GaN heterostructure that obeys a *wurtzite* symmetry can be imposed by choosing an appropriate substrate, with a similar crystalline structure. For GaN, the most commonly employed substrates are the *c*-plane of a

sapphire (Al_2O_3) crystal and Silicon (111). Although they have the same crystal symmetry, the lattice mismatch between Sapphire (0001) and GaN is 16% [49]. This value increases to 17% for a Silicon (111) - GaN interface. Although a higher defect density is expected in the case of a growth on a Silicon (111) substrate, this material is more interesting for applications due to the ease with which Silicon based technologies can be integrated in electronics. The strain accumulated during the growth process can relax, leading to the presence of defects in the lattice structure, such as cracks and dislocations. Such dislocations are shown in the cross-section transmission micrograph of a high efficiency blue light emitting diode (Fig. 1.8) [50].

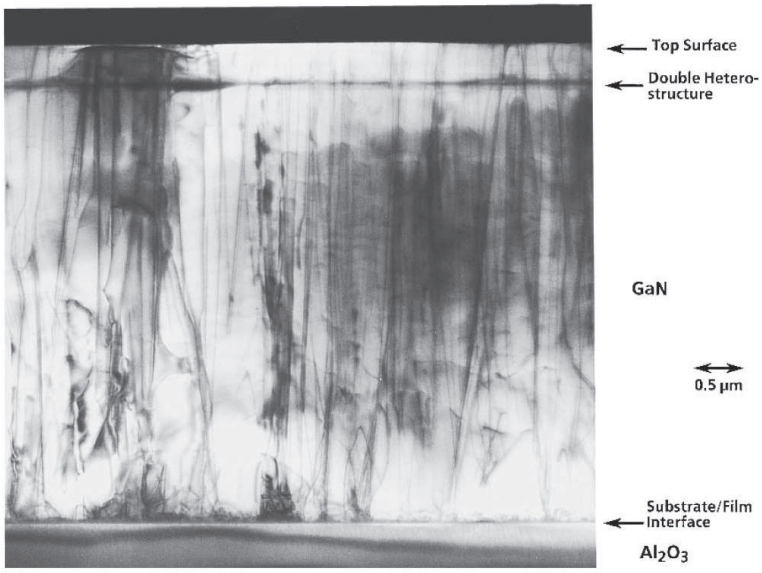

Figure 1.8. Cross-section transmission electron micrograph of a high efficiency blue light emitting diode [50].

Although the purpose of the GaN buffer layer is to relief the strain accumulated due to a lattice mismatch with the sapphire substrate, strain gives rise to threading dislocations, with a density of ~10^{10} cm^{-2} [50], that cross the active region of the device, as shown in Fig. 1.8. This value is 6 orders of magnitude higher than the ~10^4 cm^{-2} dislocation density associated to III-V arsenide systems [49]. Such defects lower the optical quality of the material by inducing variations of the band gap, and hence increasing the inhomogeneous broadening of the absorption and recombination bands. Also, they influence the recombination dynamics by acting as localization centers for the excited carriers or by giving rise to non-radiative recombination channels, reducing the overall optical efficiency of the structure. Moreover, the unrelaxed strain can lead to the presence of electric fields in the structure that modify the spatial distribution of the excited charges by modulating the conduction and valence band

profiles. In the case of quantum confined structures, the presence of the electric field modifies the optical and electronic properties of the sample.

Of particular importance for the samples described in chapter §6 is the built-in electric field. In these structures the presence of an electric field is due to two factors. The first one is linked to the presence of strain in the structure leading to the presence of *piezoelectric* polarization. This induces a piezoelectric charge distribution that generates a static electric field in the heterostructure. The second factor is related to the presence of a lack of symmetry in the crystal structure that is present in the semiconductors with a *wurtzite* lattice symmetry. This factor induces a *spontaneous* polarization ($\vec{P}_{sp}$), even in ideal strain free structures.

The presence of $\vec{P}_{sp}$ in nitride semiconductors is due to the lower symmetry of the hexagonal *wurtzite* structure with respect to that of the cubic *zinc-blende* lattice. It is very difficult to separate experimentally the spontaneous polarization and the piezoelectric polarizations, because they both lead to the presence of an electric field built in the semiconductor. The spontaneous polarization has been addressed from a theoretical point of view by Bernardini *et al.* [34]. The authors found very large values for the spontaneous polarization and, in particular, there is a large difference in $\vec{P}_{sp}$ between AlN and GaN [34]. As we will see in chapter §3, this factor was a major decision maker for the growers when they had to decide a design for the structures presented in chapters §5 and §6.

The *piezoelectric* effect is represented by the induction of an electric field inside a material when a strain field is applied to it. In this way an electric dipole is induced, leading to a macroscopic piezoelectric polarization ($\vec{P}_{pz}$). The induction of the $\vec{P}_{pz}$ vector depends on the particular lattice structure and on the lattice direction along which the strain field is applied. As $\vec{P}_{pz}$ is zero in the case of a perfect lattice matching between the different layers of a semiconductor heterostructure, theoretically its contribution can be canceled out by using quaternary alloys in order to achieve lattice matching. However, in practice this approach has its drawbacks, as it will be explained in chapter §3.

Finally, the total polarization of a material ($\vec{P}$) is expressed as the sum of the spontaneous and piezoelectric contributions:

$$\vec{P} = \vec{P}_{sp} + \vec{P}_{pz} \tag{12}$$

The Quantum Confined Stark Effect (QCSE)

The electric field that is due to the presence of built-in polarization can influence the electron and hole dynamics when they are subject to quantum confinement. In a heterostructure that provides a quantum confinement, the spatial separation of the excited charges together with the reduction of the transition energy due to the presence of an electric field is called *Quantum Confined Stark Effect* (QCSE).

In the case of quantum well structures, such as those studied in chapter §6, because the electric field due to polarization is parallel to the growth direction z, we have a so-called *longitudinal* QCSE. In the absence of an electric field (Fig. 1.9 (a)), the conduction and valence profiles are flat, and the electron and hole wavefunctions are symmetric and spatially centered in the middle of the well. By applying a longitudinal electric field, the average positions of the electrons (holes) start to move towards negative (positive) values of z (Fig. 1.9 (b)).

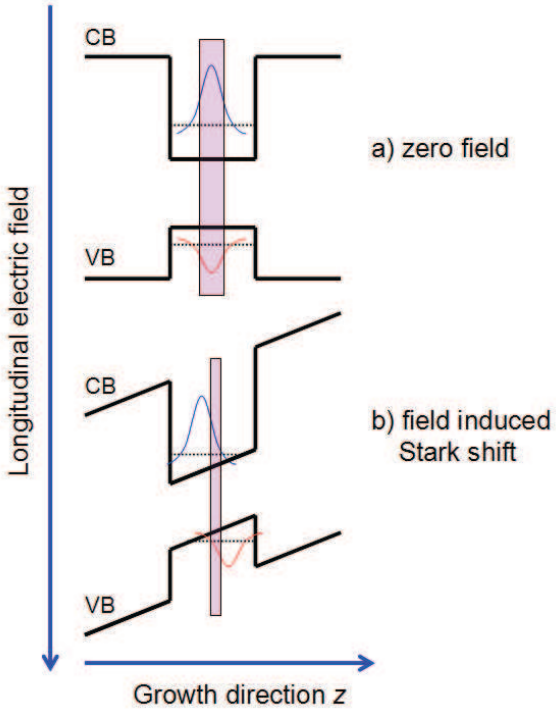

Figure 1.9. Deformation of band profiles and decrease of carrier superposition with increasing longitudinal electric field from (a) zero field to (b) strong field.

In nitride multilayers, the value of the built-in electric field is of the order of ~1 MV/cm [48]. The field induced bending of the band edges causes a spatial separation of confined electrons and holes within the well region (see Fig. 1.9), and has therefore important consequences on the optical properties of nitride-based heterostructures. The most important

consequences of the QCSE are: (i) the red shift of the transition energy with increasing well width and (ii) the blue shift of the transition energy with increasing excitation power, also know as the *screening of the electric field* [51] [52]. Electrons and holes are separated by the polarization field, but the free carrier induced field is opposite to the polarization field. The two fields tend to cancel each other out for high carrier densities, produced by high excitation densities, hence the carriers tend to recover their central positioning in the well region. This translates not only in the blue shift of the transition energy, but also into an increase of the recombination rate of electrons and holes as a result of an increased overlap between their wavefunctions in the well region, consequent to the screening of the electric field. The combined action of the well width and excitation power variation on the transition energy and recombination rate of the C1 - V1 recombination in a GaN/InGaN quantum well is presented in Fig. 1.10 [53], C1 and V1 being n = 1 level for electrons and holes, respectively.

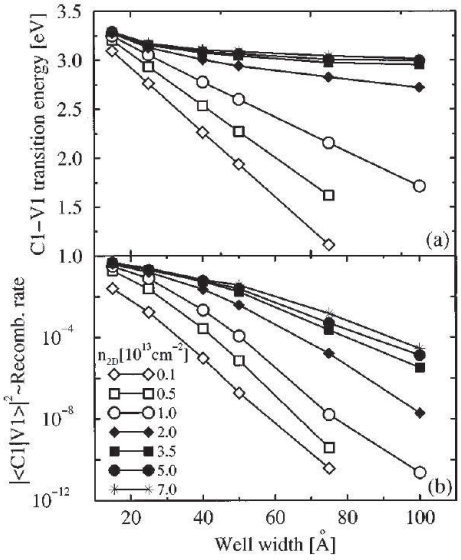

Figure 1.10. C1 - V1 transition energy and recombination rate versus well width for several n_{2D} densities in a GaN/InGaN quantum well [52].

Given these considerations, it is easy to see why the presence of QCSE in nitride heterostructures is an unwanted effect. Because a spontaneous polarization will always be present in these structures, QCSE cannot be completely eliminated, and special care must be taken when designing nitride structures in order to minimize the QCSE and account for its effects. In chapter §6 we will use these concepts to discuss the influence of the joint impact of quantum confinement and QCSE on the excitonic properties of GaN/AlGaN quantum wells with low Al content in the barriers.

1.4. Conclusions of the chapter

Looking at the structural properties of nitrides, and bulk GaN related materials in particular, the advantages they seem to offer over conventional III-V semiconductors (such as GaAs related structures) appear to be overwhelming. The existence of a direct band gap at the Γ valley that favours optical transitions, the possibility of tuning the emission from IR to deep UV when ternary and quaternary alloys are considered, and a large binding energy that allows excitons to be stable up to room temperature (and beyond) suggest that GaN related materials are indeed the best choice for the realization of next generation optoelectronic devices.

However, as these devices are in fact complex heterostructures, they are subject to numerous unwanted effects. The presence of strain causes cracks and dislocations that act as non-radiative recombination centers for carriers, and as scattering centers for photons, thus lowering the optical quality of the device. Also, the QCSE resulting from the natural presence of spontaneous polarization in *wurtzite* semiconductors combined with the piezoelectric field generated by strain between layers with different lattice constants can cause a spatial charge separation large enough to cancel out the advantages of confining carriers in a quantum well structure.

In chapter §3 we will discuss how these deciding factors influenced the approach of the growth process for the samples discussed in chapters §5 and §6.

2. Microcavities in the strong coupling regime

In Chapter §1 we concluded that the advantages exhibited by GaN related materials, and especially their large exciton binding energy allowing excitons to be stable up to room temperature and beyond, make them prime candidates for the study of light - matter interaction in semiconductor microcavities. In order to observe this interaction however, high quality resonators are needed that provide sharp photon resonances and allow an efficient coupling with the excitons of the GaN based active medium. In this chapter we will discuss the principles of such resonators. We will begin by describing the general principles of a Fabry-Pérot resonator (section §2.1) and the *transfer matrix formalism* that allows us to extract relevant parameters, such as reflectivity and transmission, of an optical resonator (section §2.2), after which we will refer to the peculiarities of a semiconductor microcavity (section §2.3). We will then discuss formation of cavity polaritons and the strong coupling regime in a semiconductor microcavity (section §2.4), and we will refer to the condensation of polaritons as the idea behind realizing a polariton laser (section §2.5).

2.1. The Fabry-Pérot resonator

The Fabry-Pérot resonator is a system composed by two mirrors M1 and M2 separated by a medium with a refractive index n_{cav} and a length L_{cav} (Fig. 2.1). An electromagnetic field incident at an angle θ_1 on M1 will travel back and forth inside the cavity, giving rise to a reflected field and a transmitted field on each side of the cavity. This will result into multiple interference inside and outside the cavity, which is dependent of L_{cav}. In order to simplify the problem and to better relate to our case of semiconductor microcavities (§2.3), we will consider that the mirros M1 and M2 are made of dielectric materials with reflectivity coefficients r_1 and r_2 and transmission coefficients t_1 and t_2, and that $n_1 = n_2 = 1$.

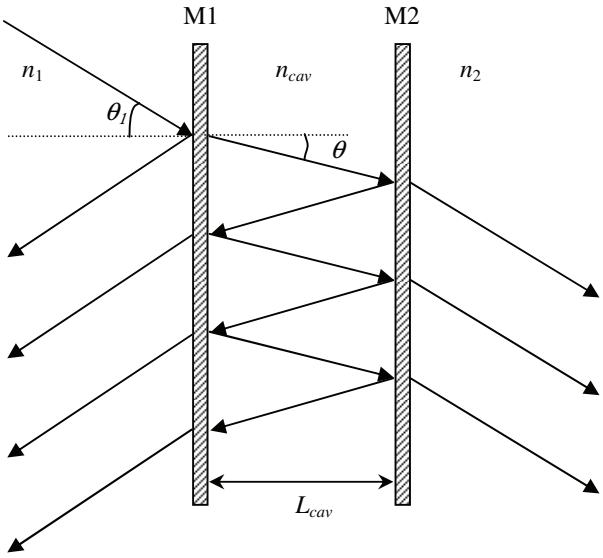

Figure 2.1. Representation of a Fabry-Pérot resonator.

The incident electric field (plane wave) can be expressed as $E_i = E_0 e^{ikz}$, with $k = 2\pi/\lambda$, where λ is the wavelength of the incident field. The amplitude of the total transmitted electric field E_t can be written as the sum of all the waves that are transmitted out of the resonator, taking into account the phase variation due to the different optical paths [54]:

$$E_t = E_0 t_1 t_2 e^{i\varphi} \sum_{m=0}^{\infty} (r_1 r_2)^m e^{-2im\varphi}, \tag{13}$$

where $\varphi = 2\pi n_{cav} L_{cav} \cos(\theta)/\lambda$, where θ is related to θ_1 through Snell's law. Eq. (13) is a geometrical series, which gives:

$$E_t = E_0 t_1 t_2 \frac{e^{-2i\varphi}}{1 - r_1 r_2 e^{-2i\varphi}} \tag{14}$$

The transmission of the Fabry-Pérot resonator can be written as [54]:

$$T_{FP} = \frac{t_1^2 t_2^2}{1 - 2r_1 r_2 \cos 2\varphi + r_1^2 r_2^2} \tag{15}$$

Considering the reflectance and transmission coefficients $R_i = |r_i|^2$ and $T_i = |t_i|^2$, with $R_i + T_i = 1$ in the case of an ideal resonator (no losses induced by absorption, scattering etc.). Eq. (15) can be rewritten as:

$$T_{FP} = \frac{(1-R_1)(1-R_2)}{\left(1-\sqrt{R_1 R_2}\right)^2} \frac{1}{1+\frac{4\sqrt{R_1 R_2}}{\left(1-\sqrt{R_1 R_2}\right)^2}\sin^2\varphi} \tag{16}$$

In Fig. 2.2 we show the variation of T_{FP} as a function of φ for different values of R_1 and R_2, with $R_1 = R_2$.

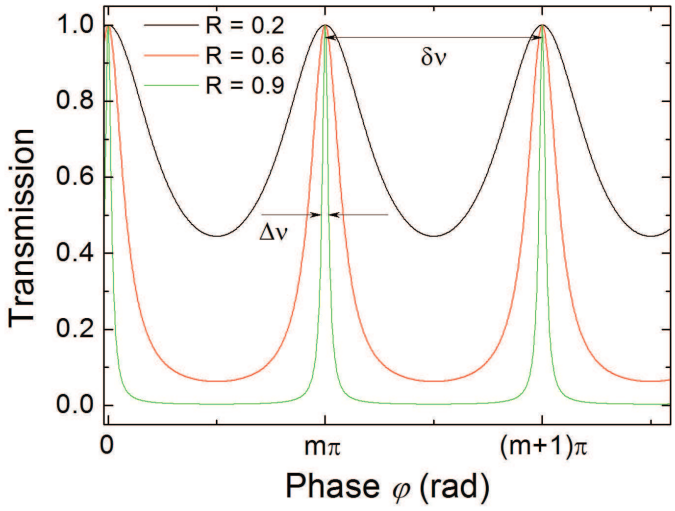

Figure 2.2. Transmission of a Fabry-Pérot resonator for R_1=R_2.

We see that the transmission reaches its maximum for:

$$\varphi = \frac{2\pi n_{cav} L_{cav} \cos\theta}{\lambda_m} = m\pi\,, \tag{17}$$

or:

$$\nu_m = \frac{mc}{2n_{cav} L_{cav} \cos\theta} \tag{18}$$

where m = 1, 2, 3... is the mode order. The *free spectral* range, *i. e.* the separation between two modes is:

$$\nu_{m+1} - \nu_m = \delta\nu_m = \frac{c}{2n_{cav}L_{cav}\cos\theta} = \frac{\nu_m}{m} \tag{19}$$

The mode broadening is given by:

$$\Delta\nu_m = \frac{c}{2\pi n_{cav}L_{cav}\cos\theta}\frac{\left(1-\sqrt{R_1R_2}\right)^{1/2}}{\sqrt[4]{R_1R_2}} \tag{20}$$

An important parameter that defines the quality of a Fabry-Pérot resonator is the *finesse*, which is the ratio between the free spectral range and the mode broadening at half maximum:

$$F = \frac{\delta\nu_m}{\Delta\nu_m} = \frac{\pi\sqrt{R_1R_2}}{1-\sqrt[4]{R_1R_2}} \tag{21}$$

Similarly, the quality of a Fabry-Pérot resonator can be quantized through the so-called *quality factor Q*, which can be expressed for each of its resonating modes *m*:

$$Q_m = \frac{\nu_m}{\Delta\nu_m} = m\pi\frac{\sqrt{R_1R_2}}{1-\sqrt[4]{R_1R_2}} = mF \tag{22}$$

We can define the photon's average lifetime τ_c inside the cavity:

$$\tau_c = \frac{L_{cav}}{c\left(1-R_1R_2\right)} \tag{23}$$

A longer photon lifetime inside the cavity ensures a better coupling of the photons with the excitons of the active medium, so it is obvious that in order to increase Q_m (and subsequently τ_c), one needs to use mirrors with the highest possible reflectivities.

2.2. The transfer matrix formalism

The mirrors usually employed for the realization of semiconductor microcavities are dielectric mirrors called *Distributed Bragg Reflectors* (DBRs), which are multilayered structures made of semiconductor materials of alternating high and low refractive index. As a result, semiconductor microcavities are structures usually made out of several tens of layers with varying refractive indexes, and a proper approach is needed to simulate and tailor their optical properties. The *transfer matrix formalism* [55] is a tool that helps us to study the propagation of light through such layered structures.

The idea is to rewrite the Snell-Descartes laws in a matricial form. We shall first consider an interface that separates two media with refractive indexes n_1 and n_2. We can describe the electric and magnetic fields of a plane wave incident on the interface at an angle θ_1, with respect to normal incidence, using the equations:

$$\vec{E} = \vec{E}_i e^{i(\omega t - k_x x - k_z z)} \tag{24}$$

$$\vec{H} = \vec{H}_i e^{i(\omega t - k_x x - k_z z)}, \tag{25}$$

where ω is the pulsation, k_x and k_z are the components of the wave vector $\vec{k}$, so that $k_x^2 + k_z^2 = |\vec{k}|^2 = k^2$, $k_z = k\cos\theta_1$ and $k_x = k\sin\theta_1$ (Fig. 2.3).

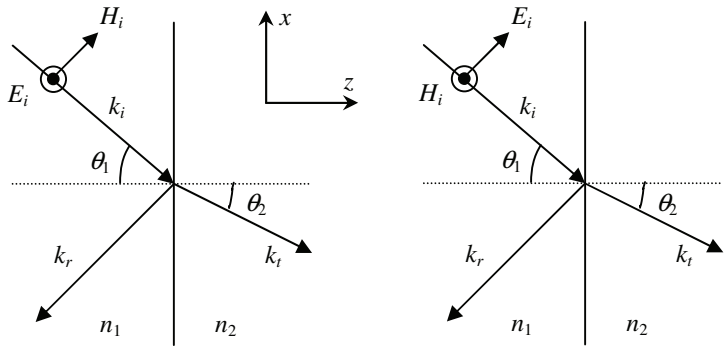

TE case TM case

Figure 2.3. Definition of the TE and TM modes.

Two types of polarizations can be distinguished. The TE polarization (or "s-wave") is associated with the waves that propagate with an electric field $\vec{E}$ perpendicular to the plane of incidence (described by normal to the surface and incident wave vector). The TM polarization (or "p-wave") is associated with the waves that propagate with an electric field $\vec{E}$ parallel to the plane of incidence. In a homogeneous and isotropic medium, TE and TM make up a base in which any form of polarization can be described.

Now let us consider the amplitudes a_1, b_1, a_2, and b_2 of the incident field, reflected field, transmitted field, and the field incident from the opposite direction on the considered interface (Fig. 2.4).

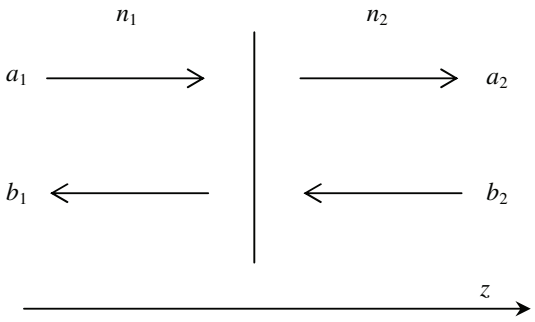

Figure 2.4. Field amplitudes used in describing the transfer matrix formalism.

The continuity conditions for the fields across the interface can be written as, in the TE case:

$$(a_1 + b_1) = (a_2 + b_2) \tag{26}$$

$$n_1 \cos\theta_1 (a_1 - b_1) = n_2 \cos\theta_2 (a_2 - b_2), \tag{27}$$

and for the TM case:

$$(a_1 + b_1)\cos\theta_1 = (a_2 + b_2)\cos\theta_2 \tag{28}$$

$$(a_1 - b_1)n_1 = (a_2 - b_2)n_2 \tag{29}$$

These conditions can be rewritten under the following matricial formulation:

$$D_1\begin{bmatrix} a_1 \\ b_1 \end{bmatrix} = D_2\begin{bmatrix} a_2 \\ b_2 \end{bmatrix} \tag{30}$$

Hence, for the TE polarization the continuity conditions become:

$$D_i^{TE} = \begin{bmatrix} 1 & 1 \\ n_i\cos\theta_i & -n_i\cos\theta_i \end{bmatrix}, \tag{31}$$

while for the TM case they are written as:

$$D_i^{TM} = \begin{bmatrix} \cos\theta_i & \cos\theta_i \\ n_i & -n_i \end{bmatrix} \tag{32}$$

Finally, one can write:

$$\begin{bmatrix} a_2 \\ b_2 \end{bmatrix} = D_2^{-1}D_1\begin{bmatrix} a_1 \\ b_1 \end{bmatrix} \tag{33}$$

In fact, the field amplitudes on one side and the other of the interface are related through the so called *transfer matrix* D_{ij}, where $D_{ij} = D_i^{-1}D_j$ and has the form:

$$D_{ij} = \begin{bmatrix} d_{11} & d_{12} \\ d_{21} & d_{22} \end{bmatrix} \tag{34}$$

We can write the transfer matrix explicitly for the TE and TM cases:

$$D_{12}^{TE} = \begin{bmatrix} \dfrac{n_2\cos\theta_2 + n_1\cos\theta_1}{2n_2\cos\theta_2} & \dfrac{n_2\cos\theta_2 - n_1\cos\theta_1}{2n_2\cos\theta_2} \\ \dfrac{n_2\cos\theta_2 - n_1\cos\theta_1}{2n_2\cos\theta_2} & \dfrac{n_2\cos\theta_2 + n_1\cos\theta_1}{2n_2\cos\theta_2} \end{bmatrix} \tag{35}$$

$$D_{12}^{TM} = \begin{bmatrix} \dfrac{n_1\cos\theta_2 + n_2\cos\theta_1}{2n_1\cos\theta_2} & \dfrac{n_2\cos\theta_1 - n_1\cos\theta_2}{2n_1\cos\theta_2} \\ \dfrac{n_2\cos\theta_1 - n_1\cos\theta_2}{2n_1\cos\theta_2} & \dfrac{n_1\cos\theta_2 + n_2\cos\theta_1}{2n_1\cos\theta_2} \end{bmatrix} \tag{36}$$

Similarly, one can calculate the Fresnel coefficients that give the fractions of the reflected and transmitted fields on each side of the interface. These coefficients are:

TE case: $$r_{12} = \frac{n_1\cos\theta_1 - n_2\cos\theta_2}{n_1\cos\theta_1 + n_2\cos\theta_2} \quad \text{and} \quad t_{12} = \frac{2n_1\cos\theta_1}{n_1\cos\theta_1 + n_2\cos\theta_2} \tag{37}$$

TM case: $$r_{12} = \frac{n_1\cos\theta_2 - n_2\cos\theta_1}{n_1\cos\theta_2 + n_2\cos\theta_1} \quad \text{and} \quad t_{12} = \frac{2n_1\cos\theta_2}{n_1\cos\theta_2 + n_2\cos\theta_1} \tag{38}$$

By identifying these coefficients with those of the transfer matrices, we obtain:

$$r_{12} = -\frac{d_{21}}{d_{11}} \quad \text{and} \quad t_{12} = \frac{1}{d_{11}}, \tag{39}$$

which allows us to rewrite the transfer matrix in a form which is independent of polarisation:

$$D_{12} = \begin{bmatrix} \dfrac{1}{t_{12}} & -\dfrac{r_{12}}{t_{12}} \\ -\dfrac{r_{12}}{t_{12}} & \dfrac{1}{t_{12}} \end{bmatrix} \tag{40}$$

Therefore, the reflectivity R and transmission T can be extracted directly from the transfer matrix:

$$R = |r|^2 = \left|\frac{d_{21}}{d_{11}}\right|^2 \quad \text{and} \quad T = \frac{n_2}{n_1}\left|\frac{1}{d_{11}}\right|^2 \tag{41}$$

Hence, the transfer matrix formalism allows a simple calculation of the reflectivity and the transmission of a multilayered structure, and it is particularly suitable for numerical calculations. As a consequence, the simulated reflectivity and transmission spectra of the

various layered structures (DBRs, microcavities) that will be presented in the following sections and chapters were obtained using a Matlab program that uses the transfer matrix formalism to calculate these coefficients.

2.3. Semiconductor microcavities

The Bragg reflectors

As we have previously mentioned, distributed Bragg reflectors (DBRs) are periodic layered structures, usually composed of two alternating semiconductor materials with refractive indexes n_1 and n_2, and thicknesses d_1 and d_2, so that $n_1 d_1 = n_2 d_2 = \lambda_0 / 4$, where λ_0 is the vacuum wavelength of the resonant cavity mode.

The role of these layers is to recover through an interplay of constructive interferences the transmitted part of the electromagnetic wave incident on each of the interfaces (Fig. 2.5). In this approach, a plane wave reflected at a n_0/n_1 or n_2/n_1 interface ($n_1 > n_2 > n_0$) undergoes a π phase change, while that reflected at a n_1/n_2 interface suffers no change of phase. Every time the electromagnetic wave traverses a layer, its phase is increased by $\pi/2$. In the end, the phase difference between the light that goes out through the incident surface and the incident beam is always π, which gives rise to constructive interference between the two waves.

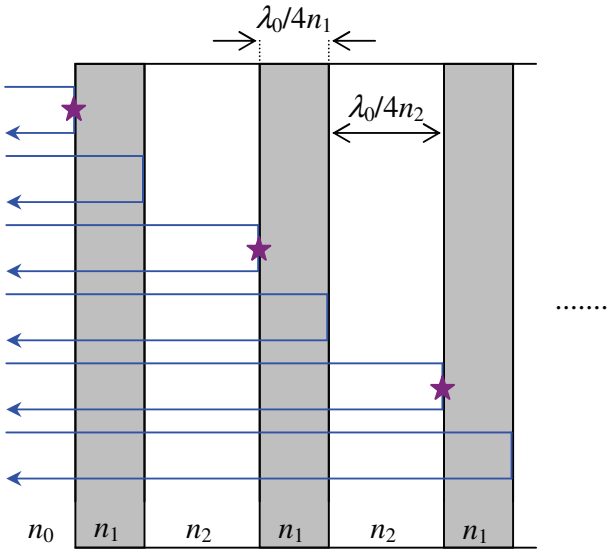

Figure 2.5. Schematic representation of a DBR.

In analogy with the principle of operation of a Fabry-Pérot resonator, the condition of constructive interference determines an increase of the reflection coefficient, and, with a convenient choice of layer parameters, reflectivity values close to unity can be obtained. Thanks to the transfer matrix formalism described in the previous section, the optical response of a DBR can be easily resolved numerically. For a DBR composed of 2N layers, we can write the field at the last interface as a function of the field on the first interface:

$$\begin{bmatrix} a_N \\ b_N \end{bmatrix} = \prod_{i=2}^{2N} P_i D_{i-1,i} \begin{bmatrix} a_1 \\ b_1 \end{bmatrix}, \tag{42}$$

where $D_{i-1,i}$ is the transfer matrix at the interface between the medium i-1 and the medium i, and P_i is the propagation matrix across the medium i. Following this procedure, in Fig. 2.6 we present the simulated reflectivity spectra of an 8 pair $Al_{0.2}Ga_{0.8}N$/AlN DBR grown on a Si (111) substrate, optimized for a central energy ν_0 of 3.49 meV (~355 nm). The parameters used in this simulation are: the refractive index of the incident medium (air), n_0 = 1; the refractive index of AlN (n_{AlN} = 2.165) and $Al_{0.2}Ga_{0.8}N$ ($n_{Al0.2Ga0.8N}$ = 2.52) at 355 nm [56]; the refractive index of the Si (111) substrate (n_{Si} = 5.64) at 355 nm [57]. For the sake of simplicity, no energy dependence of the refractive indexes was assumed, and no absorption effects in the DBR layers were considered.

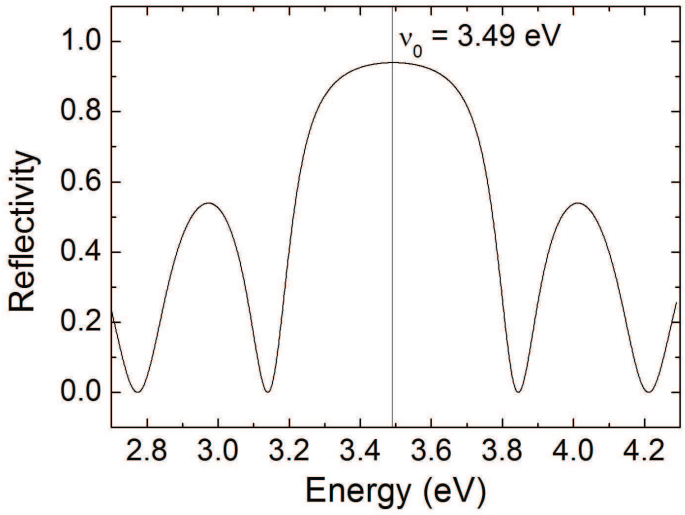

Figure 2.6. Theoretical reflectivity spectrum of a DBR made out of 8 pairs of $Al_{0.2}Ga_{0.8}N$/AlN λ/4 layers grown on Si (111).

The maximum reflectivity of this DBR is $R \cong 0.94$, at the central energy ν_0. We define as *stop band* the spectral range centered at ν_0 where $R > 0.9$. Its presence can be explained by considering the DBR as a one-dimensional periodical system. The wave pattern in such a structure must obey the Bloch theorem. In analogy with electrons in a crystal, a zone of forbidden solutions for the wave vectors is thus created: the *gap*. This stop band is the spectral range of forbidden photonic modes in the structure. For a sufficiently high number of layers (*N*), the width $\Delta\nu$ of the stop band is proportional to the refractive index difference $\Delta n(\nu_0) = n_1(\nu_0) - n_2(\nu_0)$, $n_1 > n_2$ [58]:

$$\frac{\Delta\lambda}{\lambda_0} = \frac{\Delta\nu}{\nu_0} = \frac{2\Delta n}{\pi n}, \tag{43}$$

where n is the average value of the refractive index. For the structure simulated above, the stop band width is ~34 nm, which corresponds to a stop band of ~335 meV in this spectral range. The reflectivity of a DBR can be evaluated analytically for $\nu = \nu_0$ [58]:

$$R = \left(\frac{1 - \frac{n_s}{n_0}\left(\frac{n_2}{n_1}\right)^{2N}}{1 + \frac{n_s}{n_0}\left(\frac{n_2}{n_1}\right)^{2N}} \right)^2, \tag{44}$$

where n_s is the refractive index of the substrate and n_0 is the index of the incidence medium. We see that if the contrast between the refractive indexes of the Bragg layers is small, *N* must be increased in order to recover the desired reflectivity at the central energy.

Following eq. (22), in order to have a cavity with a quality factor of several hundreds, both mirrors' reflectivity needs to be higher than 95%. In Fig. 2.7 we show the dependence of reflectivity on the number of pairs of $\lambda/4$ layers for a $Al_{0.2}Ga_{0.8}N$/AlN DBR, using the refractive indexes quoted for the theoretical reflectivity spectra presented in Fig. 2.6. It thus becomes obvious that since in our case the ratio between the layers of the DBR is $n_1 / n_2 = 1.164$, at least 9 pairs of $\lambda/4$ layers must be used for the Bragg reflector in order to achieve a reflectivity higher than 95%.

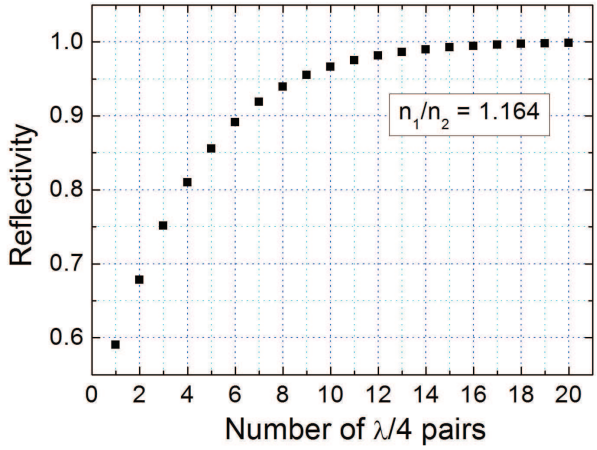

Figure 2.7. Reflectivity as a function of the number of λ/4 pairs (2*N*) for an $Al_{0.2}Ga_{0.8}N$/AlN DBR.

The semiconductor microcavity

A semiconductor microcavity is a structure obtained through specific growth techniques, which will be discussed in more detail in the following chapter. As a result, due to constrains on the growth process, semiconductor microcavities are generally of the type shown in Fig. 2.8. A bottom DBR (DBR2) with N_2 pairs of λ/4 layers is first grown on a substrate; after that a thicker layer that forms the actual cavity and contains the active region is deposited on top of DRB2; the microcavity is completed by the deposition of a top DBR (DBR1) made out of N_1 pairs of λ/4 layers.

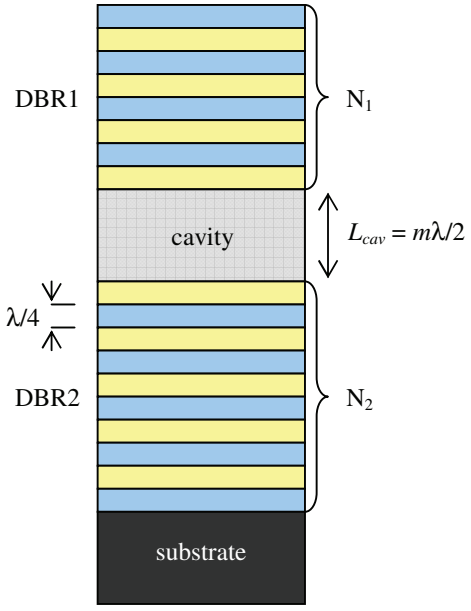

Figure 2.8. Schematic representation of a semiconductor microcavity.

Qualitatively, the semiconductor microcavity is very similar to a simple Fabry-Pérot structure with planar mirrors, and many of the standard Fabry-Pérot results for reflectivity, transmission, quality factor etc. apply. In order to achieve a resonance with a desired photonic mode at normal incidence, the length of the cavity region (L_{cav}) must be a multiple integer of half λ/2, where λ is the desired resonant wavelength. In the case of a Fabry-Pérot resonator with metallic mirrors, L_{cav} will be the length of the entire resonator. However, since the DBRs are mirrors in which the electric field penetrates, the Fabry-Pérot cavity length has to be replaced by a significantly larger cavity length [4] [59]:

$$L_{eff} = L_{cav} + L_{DBR}\,, \tag{45}$$

where L_{DBR} is the penetration length into the DBRs and is given by [4]:

$$L_{DBR} = \frac{\lambda}{2n_{cav}} \frac{n_L n_H}{n_H - n_L}, \tag{46}$$

in which λ is the wavelength of light in the cavity, n_{cav} is the refractive index of the cavity, and n_L and n_H are the refractive indexes of the low and high index λ/4 layers, respectively.

In order to calculate the optical response of this system, we can use the same simple method that we used for a DBR. If we consider the fact that the cavity is a 'perturbation' in the periodicity of the layers that form the DBR, we can make an analogy between this perturbation and the defects of a crystalline matrix. These defects introduce certain levels within the semiconductor forbidden band. Analogously, the presence of the cavity will introduce a new 'level' in the stop band of the Bragg reflectors, i. e. a spectral region in which reflectivity exhibits a sharp decrease. By carefully choosing the cavity length L_{cav} to be an multiple integer of half of the DBR's working wavelength λ, we can conveniently place this new level in the center of the stop band [60].

In Fig. 2.9 we present the theoretical reflectivity spectrum of a semiconductor microcavity with AlN/$Al_{0.2}Ga_{0.8}N$ DBRs (N_1 = 10, N_2 = 10), and a λ/2 cavity length. The background refractive index of GaN [56] (n_{cav} = 2.4) was used as the refractive index of the cavity region.

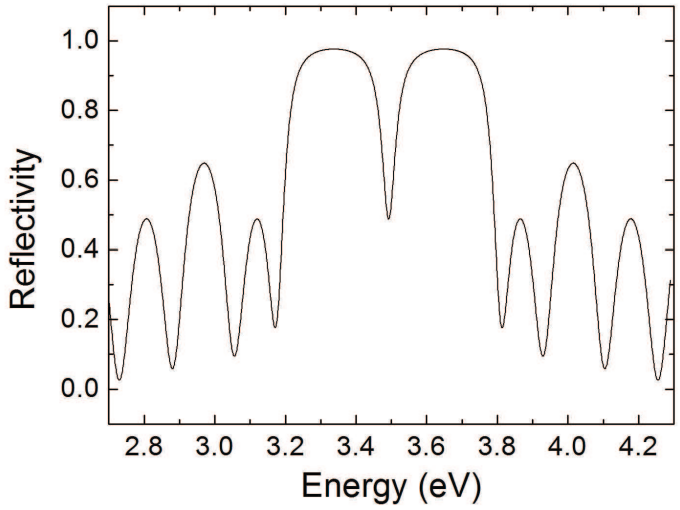

Figure 2.9. Theoretical reflectivity of a λ/2 microcavity with top and bottom DBRs made of 10 pairs of AlN/$Al_{0.2}Ga_{0.8}N$ λ/4 layers.

Since the mirrors have finite transmission, the cavity mode has a finite width Δ_{cav} (full width at half-maximum), given by, for $R \to 1$ [60]:

$$\Delta_{cav} = \frac{\hbar c(1-R)}{n_{cav} L_{eff}} \tag{47}$$

This width can be considered as the homogeneous (or lifetime) broadening of the confined cavity mode, related to the losses through the mirrors.

As we can see, the confinement of photons in such a microcavity is achieved in the growth direction. This means that there is no lateral confinement, which gives these structures the name of *planar microcavities*. The wave vector of a photon inside the cavity can be separated in two parts: k_z (the component perpendicular to the layers of the structure) and $k_{\parallel}$ (the component parallel to the layers), so that $k^2 = k_z^2 + k_{\parallel}^2$, where k is the wave vector modulus of the considered photon. k_z is discrete due to the effect of the cavity in the z direction, and we have:

$$k_z = \frac{m\pi}{L_{cav}}, \tag{48}$$

where m is the order of the mode. The energy of a photon can be written as:

$$E = \frac{\hbar ck}{n_{cav}} = \frac{\hbar c}{n_{cav}}\sqrt{k_z^2 + k_{\parallel}^2} \tag{49}$$

Due to the axial confinement of the mirrors, we have $k_z >> k_{\parallel}$, and therefore eq. (49) becomes:

$$E = \frac{\hbar ck_z}{n_{cav}}\left(1+\frac{k_{\parallel}^2}{2k_z^2}\right) = E_0 + \frac{\hbar ck_{\parallel}^2}{2n_{cav}k_z} = E_0 + \frac{\hbar^2 k_{\parallel}^2 c^2}{2n_{cav}^2 E_0}, \tag{50}$$

with $E_0 = \hbar ck_z / n_{cav}$. Now the energy equation can be written under the form:

$$E = E_0 + \frac{\hbar^2 k_{\parallel}^2}{2M}, \qquad \text{with} \quad M = \frac{n_{cav}^2 E_0}{c^2} = m\frac{\hbar\pi n_{cav}}{L_{cav}c} \tag{51}$$

For small $k_{\parallel}$ the dispersion of the cavity mode is parabolic, and it can be described by a cavity photon effective mass *M*. For a microcavity similar to the one presented in Fig. 2.9 this mass is calculated to be very small, around ~10^{-4} - $10^{-5} m_e$, where m_e is the free electron rest mass. Hence, the cavity photon modes of a microcavity have a strong in-plane dispersion, which is not quantized. Following eq. (51), the energy of a photon with wave vector $k_z = 2\pi / L_{cav}$ and in-plane wave vector $k_{\parallel}$ in the medium, is given by:

$$E(k_{\parallel}) = E_0\left(1+\frac{\hbar^2 c^2 k_{\parallel}^2}{E_0^2 n_{eff}^2}\right)^{1/2}, \tag{52}$$

where n_{eff} is the effective refractive index of the structure [61] and $E_0 = hc / n_{eff} L_{cav}$ is the photon energy for $k_{\parallel} = 0$. $k_{\parallel}$ is related to the external angle of incidence θ by:

$$k_{\parallel} = \frac{E(k)}{\hbar c}\sin\theta, \tag{53}$$

and, as a result, a particular $k_{\|}$ mode can be selected simply by varying the external angle of incidence θ. Elimination of $k_{\|}$ between (52) and (53) leads to the following expression for the energy of the cavity mode as a function of θ:

$$E(\theta) = E_0 \left(1 - \frac{\sin^2 \theta}{n_{eff}^2} \right)^{-1/2} . \tag{54}$$

The determination of the energy dispersion modes by varying the external angle of incidence q is a very practical experimental technique that will be further detailed in chapters §4 and §5.

2.4. Polaritons and the strong coupling regime

As mentioned in the introduction, the first coupling phenomenon in a semiconductor microcavity was observed by Weisbuch *et al*. in 1992 [1], and since then the physics of microcavities in the strong coupling regime has been investigated with growing interest. Very soon after the first observation of cavity polaritons in reflectivity measurements (Fig. 2.10), the basic theoretical framework for the description of the polariton modes was developed.

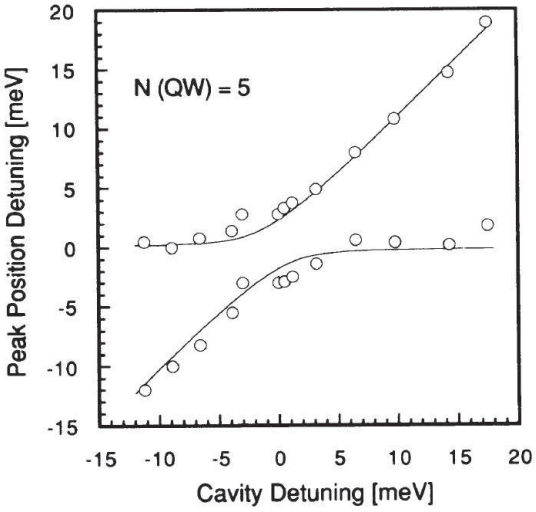

Figure 2.10. The first observation of polariton dispersion curves obtained from reflectivity measurements on a GaAs based QW microcavity [1].

The general concept of "polariton" was first described by J. J. Hopfield in 1958 [65] as the formation of a quasiparticle resulting from the strong coupling of electromagnetic waves with an electric or magnetic dipole-carrying excitation. In this thesis we will discuss microcavity polaritons resulting from the interaction between a cavity photon and an exciton.

The appearance of a vacuum-field Rabi splitting in the polariton spectrum was understood in terms of a simple linear dispersion model [62], in analogy to what had been applied to the case of the atom - cavity vacuum Rabi splitting [63]. In this mode, the exciton linear response function is described in terms of a Lorentz resonance, and the overall response of the cavity is evaluated within the linear response theory of the classical electromagnetic field. Hence, the susceptibility for an excitonic resonance $\omega_{ex}\left(\vec{k}\right)$ can be written as:

$$\chi\left(\vec{k},\omega\right)=\frac{n_0 e^2}{m_e}\frac{f}{\omega^2-\omega_{ex}^2\left(\vec{k}\right)+2i\eta\omega}, \tag{55}$$

where η is the damping of the resonance and $f=\left(2m_0/\hbar\right)\omega_{ex}\mu^2$ the oscillator strength of the excitonic transition, with μ the dipole matrix element of the transition. The dielectric function is:

$$\varepsilon\left(\vec{k},\omega\right)=\varepsilon_\infty+\omega_{pl}^2\frac{f}{\omega^2-\omega_{ex}^2\left(\vec{k}\right)+2i\eta\omega}, \tag{56}$$

where ε_∞ is the background dielectric constant that accounts for all the other resonances of the medium and $\omega_{pl}=\sqrt{4\pi n_0 e^2/m_e}$ is the plasma frequency, with n_0 the refractive index of the medium.

In order to account for the presence of an electrical dipole inside the cavity region of a semiconductor microcavity, the transfer matrix of the structure must be rewritten to include the effect of $\varepsilon\left(\vec{k},\omega\right)$. This can be achieved by expressing the refractive index of the cavity region n_{cav} as:

$$n_{cav}=\sqrt{\left(n_{cav}^{\infty}\right)^2+\varepsilon_{LZ}\left(\vec{k},\omega\right)}, \tag{57}$$

where n_{cav}^{∞} is the background refractive index, and ε_{LZ} only accounts for the presence of an electric dipole described as a Lorentz oscillator. As we will see from transfer matrix simulations, the inclusion of an electric dipole in the cavity region, *i. e.* the *active region*, of a semiconductor microcavity results in a strong modification of its reflectivity and transmission properties. This approach gives a simple and elegant description of the so called *bulk microcavity* structure, to be extensively discussed in chapter §5.

However, this approach does not give a detailed description of the coupling between photons and excitons. In order to achieve a more complete description of the system we will first consider the dipole as an oscillator characterized by an energy E_x and a wave vector $\vec{k}_x$. Similarly, we will consider a photon with an energy E_c and a wave vector $\vec{k}_c$. As long as the two oscillators are in resonance, they can couple if $\vec{k}_x = \vec{k}_c$. The states resulting from this coupling are called *polaritons*, and they are non-degenerate. These polaritons are linear combinations of the photon state and the dipole state [65].

The simplest way of describing the microcavity system is to consider photons corresponding to the cavity mode and excitons inside the *bulk* active region as coupled harmonic oscillators with the same $k_{\parallel}$. This allows us not only to calculate the optical response of the system using the transfer matrix formalism, but also to develop a quantum treatment for a better qualitative description of its main characteristics. We will describe the microcavity as a two level system, under the form |exciton> |photon>, so that: $|e\rangle|0\rangle$ is the state describing the presence of an exciton in the active region and 0 photons in the cavity, and $|g\rangle|1\rangle$ is the state describing the presence of a photon in the cavity and 0 excitons in the bulk. Let *V* be the coupling term (interaction potential) of the two oscillators $|e\rangle|0\rangle$ and $|g\rangle|1\rangle$. Moreover, we take into account the damping of the oscillators: let Γ_x be the damping term of the $|e\rangle|0\rangle$ oscillator (*i. e.* the average lifetime of the exciton), and Γ_c the damping of the $|g\rangle|1\rangle$ oscillator (*i. e.* the average photon lifetime inside the cavity). In fact, Γ_x and Γ_c describe the homogeneous broadenings of the two uncoupled modes [64]. We can write the Hamiltonian of this simplified system in the form of a 2x2 matrix:

$$H_{k_{\parallel}} = \begin{bmatrix} E_x(k_{\parallel}) - i\Gamma_x(k_{\parallel}) & V(k_{\parallel}) \\ V(k_{\parallel}) & E_c(k_{\parallel}) - i\Gamma_c(k_{\parallel}) \end{bmatrix} \tag{58}$$

Here, E_x and E_c are the energies of the uncoupled exciton and cavity modes. The eigenstates of this matrix are noted $|u\rangle$ and $|l\rangle$, and they describe the so called *upper* and *lower polariton* states, respectively, whereas E_u and E_l are their corresponding eigenvalues. After diagonalizing $H_{k_\parallel}$ we obtain:

$$E_{u,l} = \frac{E_x + E_c - i(\Gamma_x + \Gamma_c)}{2} \pm \sqrt{V^2 + \frac{1}{4}\left(E_x - E_c - i(\Gamma_x - \Gamma_c)\right)^2} \tag{59}$$

By indicating $E_m = (E_x + E_c)/2$, $\Gamma_m = (\Gamma_x + \Gamma_c)/2$, $\delta = E_c - E_x$, and $\Delta = \Gamma_x - \Gamma_c$, we can rewrite eq. (59) as:

$$E_{u,l} = (E_m - i\Gamma_m) \pm \sqrt{V^2 + \frac{1}{4}(-\delta - i\Delta)^2} \tag{60}$$

δ is referred to as the *detuning* between the two uncoupled modes. Following its definition, δ will assume negative values if the energy of the uncoupled photon mode is smaller then that of the bare exciton; in this case we will have a *negative detuning*. Conversely, if $E_c > E_x$, δ will be positive and we will refer to the so-called *positive detuning*. At resonance, $E_c = E_x \rightarrow \delta = 0$, we have *zero detuning* between the uncoupled exciton and photon modes.

Being a linear superposition of bosons, *i. e.* an exciton and a photon with the same in-plane wavenumber $k_\parallel$, polaritons are also bosons. The exciton and photon fractions in each of the polariton states $|u\rangle$ and $|l\rangle$, respectively, are given by the amplitude squared of $c_c^{u,l}$ and $c_x^{u,l}$, which are referred to as the Hopfield coefficients [65]:

$$\begin{vmatrix} u \\ l \end{vmatrix} = c_c^{u,l} |g\rangle|1\rangle \pm c_x^{u,l} |e\rangle|0\rangle, \tag{61}$$

where:

$$c_c^{u,l} = \sqrt{\frac{W(2W \pm \delta) - V^2}{W(2W \pm \delta)}} \qquad \text{and} \qquad c_x^{u,l} = \frac{V}{\sqrt{W(2W \pm \delta)}}, \tag{62}$$

with $W = \sqrt{\delta^2/4 + V^2}$. From eqs. (62) we see that the exciton and photon fraction of each polariton state satisfies:

$$\left|c_c^{u,l}\right|^2 + \left|c_x^{u,l}\right|^2 = 1 \tag{63}$$

In the resonance condition (for $\delta = 0$), $\left|c_c^{u,l}\right|^2 = \left|c_x^{u,l}\right|^2 = \frac{1}{2}$, so that upper polariton and lower polariton are exactly half photon, half exciton. Also, for $\delta = 0$, eq. (60) simplifies, and we see that the term under the square root can assume either positive or negative values.

If $4V^2 > \Delta^2$, then the value of the term under the square root remains positive, and we obtain two solutions which give two values corresponding to the energy of the upper polariton E_u, and the lower polariton E_l, respectively. In this case, the microcavity is in the so-called *strong coupling regime*. The energy separation between the two polariton states is:

$$E_u - E_l = \Omega_{Rabi} = h\nu_{Rabi} = 2\sqrt{V^2 - \frac{1}{4}\Delta^2}, \tag{64}$$

where ν_{Rabi} is the Rabi frequency. The energy separation of the two modes at resonance ($\delta = 0$) is called *Rabi splitting*. More intuitively, since Γ_x and Γ_c can be expressed as the broadenings of the uncoupled exciton and photon modes, respectively, the condition to observe the Rabi splitting is the presence of an interaction potential *V* that overcomes the damping effect Γ_x and Γ_c, so that $V^2 > (\Gamma_x - \Gamma_c)^2/16$. In Fig. 2.11 we give a schematic representation of the energy dispersion of the two polariton states, $|u\rangle$ and $|l\rangle$, as a function of the uncoupled exciton - photon detuning δ. The dispersion curves were obtained by considering a constant exciton energy $E_x(k_\parallel) = 3.49$ eV, and $E_c(k_\parallel)$ having a linear variation in the Hamiltonian of eq. (58). We can see that for $\delta >> 0$, the upper polariton $|u\rangle$ tends towards the uncoupled cavity mode, while the lower polariton $|l\rangle$ tends towards the bare

exciton mode. Conversely, for $\delta << 0$, $|u\rangle$ tends towards the excitonic state, and $|l\rangle$ towards the cavity mode.

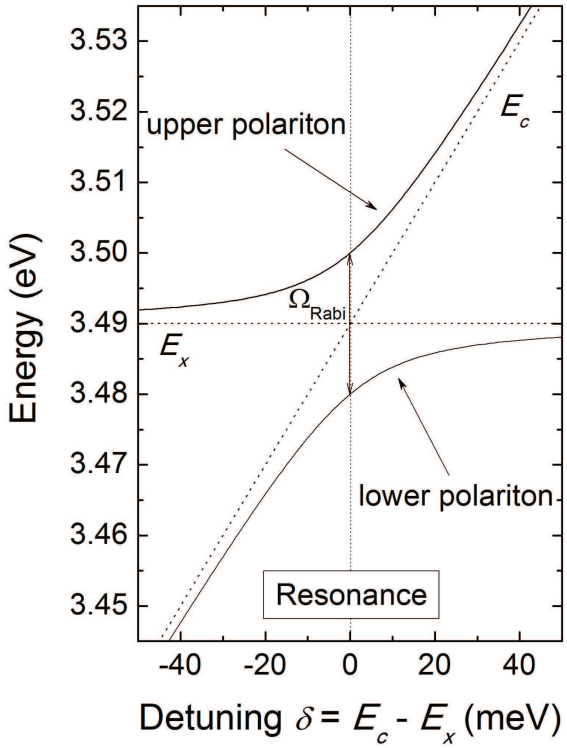

Figure 2.11. Energy dispersion of the upper and lower polariton states (full lines) in the strong coupling regime as a function of exciton - cavity mode detuning. The dotted lines refer to the uncoupled modes.

If $4V^2 < \Delta^2$, the quantity under the square root in eq. (60) is negative. Hence, the solution is imaginary, and no Rabi splitting can be observed. Only the lifetimes of the oscillators are modified in this case, and this condition is termed as *weak coupling regime*.

As previously mentioned, the reflectivity spectra of a bulk microcavity in the strong coupling regime can be simulated by including the effect of the exciton (dipole) in the dielectric response of the cavity medium. Nevertheless, in eq. (57) ε_{LZ} only accounts for the homogeneous broadening of the exciton. In a real bulk microcavity however, an inhomogeneous broadening of the exciton mode is also present due to the presence of disorder in the active medium. This broadening can be accounted for by considering a Gaussian distribution of Lorentz oscillators, with a full width at half maximum equal to the inhomogeneous broadening of the excitonic transition.

Following the formalism described in section §2.2, Fig. 2.12 presents the simulated reflectivity spectrum of a bulk GaN microcavity similar to the one presented in Fig. 2.9, but

with the inclusion of the exciton in the cavity region. The spectrum was simulated for a sample temperature of ~10 K corresponding to a ~1 meV homogeneous broadening, and an inhomogeneous exciton broadening of 5 meV. Also, a 1 meV longitudinal transverse splitting (which expresses the strength of the coupling of the exciton with the electromagnetic field) was considered, which is the approximate value found for the *A* exciton of bulk GaN [66]. The value of the oscillator strength in GaN is one order of magnitude higher than in GaAs, where the longitudinal transverse splitting is only 0.08 meV [66], proving once again the potential of GaN based microcavities over their GaAs counterparts. At resonance, the degeneracy between the uncoupled cavity and exciton modes is removed by the coupling, which gives rise to the two polaritonic states: LP and UP.

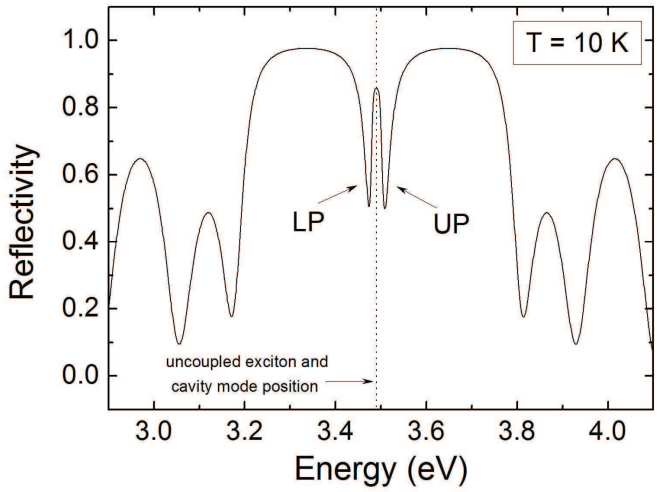

Figure 2.12. Simulated reflectivity spectra of a λ/2 bulk GaN microcavity with AlN/$Al_{0.2}Ga_{0.8}N$ DBRs.

The Rabi splitting in Fig. 2.12 is $\Omega_{Rabi} = 35\,\text{meV}$, which is in good agreement with the value measured for a similar microcavity [67]. The large Rabi splitting, to be compared with that of only ~5 - 7 meV for GaAs based microcavities [18], is a determining factor for the observation of the strong coupling at room temperature and beyond in GaN based microcavities, which is of utmost practical importance for the realization of a polariton laser operating at room temperature.

As suggested by eq. (61), the energy broadening of the polariton modes can be simply defined as:

$$\Gamma_{u,l} = \left|c_x^{u,l}\right|^2 \Gamma_x + \left|c_c^{u,l}\right|^2 \Gamma_c , \tag{65}$$

which means that at resonance $\Gamma_{u,l} = (\Gamma_x + \Gamma_c)/2$.

The study of the exciton - photon coupling in bulk GaN microcavities will be addressed in more detail in chapter §5.

2.5. Bose-Einstein condensation of polaritons

The ultimate goal of realizing a high-quality GaN based microcavity is to favour a Bose-Einstein condensation (BEC) of polaritons at room temperature. Bosons can show a spectacular transition to a peculiar condensed phase: the Bose-Einstein condensate [68], an accumulation of a macroscopic number of bosons in the ground state of a system.

Due to their bosonic properties, a variety of quantum phases have been predicted for polaritons, including BEC, superfluidity, crossover from BEC to Bardeen-Cooper-Schrieffer states etc. [69] [70]. Compared to other BEC systems, such as atomic gases and excitons, polaritons have vastly different length, energy, and time scales [69]. Besides, as an essentially different system of fundamental interest, polaritons also possess many unique advantages for BEC research.

First of all, the critical temperature of polariton condensation ranges from a few Kelvin to above room temperature, which is four orders of magnitude higher than that of excitons, and eight orders of magnitude higher than that of atoms. It originates from the very light effective mass of polaritons due to the mixing with cavity photons.

From the experimental point of view, the microcavity polariton is a very accessible system. There exists a one-to-one correspondence between an internal polariton in mode $k_{\parallel}$ and an external photon with the same energy and in-plane wavenumber, propagating at an angle θ respect to the growth axis.

The polariton laser as an application to the BEC of polaritons was proposed for the first time by Imamoglu *et al.* [14] in 1996. The idea of generating a coherent optical wave using final-state stimulation of exciton-phonon scattering in the $k \cong 0$ region of the lower polariton branch sparked a strong interest in the scientific community to produce a new generation of parametric optical amplifiers and ultra-low threshold lasers [15]. However, this approach is only valid in the low-excitation density limit, where the excitons (and polaritons) satisfy bosonic commutation relations [14]. Together with the disorder present in semiconductors, this limitation posed serious problems in achieving a cavity polariton

condensate, and it was only in 2006 that the condensation of polaritons resulting in a coherent emission from the $k \cong 0$ region was demonstrated in a CdTe microcavity at low temperature [24].

The pursuit of achieving a coherent emission from a room temperature polariton condensate was and continues to be the driving force behind the study of GaN based microcavities [26], and related nanostructures.

2.6. Conclusions of the chapter

In this chapter we discussed the working principles of a Fabry-Perot resonator as an instrument able to provide a good confinement of the electromagnetic field between two mirrors and a discretization of its oscillating modes. The multilayered structure of microcavities however required the introduction of a proper formalism that allows a simple and elegant treatment of the propagation of an electromagnetic field through these structures; hence, the transfer matrix formalism was described. This formalism was first applied to describe basic properties of the DBRs and the bare cavity, such as the reflectivity and the energy dispersion of a photon in the absence of coupling with the medium in which propagation occurs.

The introduction of an electric dipole (the exciton) in the cavity region proved to strongly modify the optical properties of the structure due to the coupling between the exciton and photon modes, and to give rise to a new particle - the polariton - which is a linear superposition of the two uncoupled states. Hence, in the strong coupling regime, the uncoupled exciton and photon dispersion curves are replaced with two polariton dispersion curves (upper and lower polariton, respectively), which at resonance exhibit a Rabi splitting of several tens of meV for a GaN based microcavity. Such a large value for the Rabi splitting assures the stability of polaritons at room temperature, providing a perspective to achieve a polariton condensate at this temperature.

The study of exciton - photon coupling in bulk GaN microcavities will be the main focus of chapter §5.

3. Growth related issues

After having presented a general theoretical description of the main properties of semiconductor microcavities in chapters §1 and §2, we will now give a brief description of the factors that decided the approach towards the growth of the samples studied in chapters §5 and §6.

3.1. The growth of III-nitride heterostructures

As already mentioned in chapter §1, the growth of a GaN heterostructure that obeys a *wurtzite* symmetry can be imposed by choosing an appropriate substrate, with a similar crystalline structure. Although a lot of the samples discussed in the following chapters are not complete GaN microcavities, growers, when designing and creating all of these structures, focused on identifying the optimal growth parameters and materials. The underlying idea was the realization of a high optical quality GaN based semiconductor microcavity to permit the observation of the strong coupling regime, and eventually allow for a condensation of polaritons in the low k region. Finally, the possible integration into more sophisticated optoelectronic devices was desired. Hence, the purpose was not only to achieve a high quality structure, but also one that would be proven useful for practical purposes.

The ideal substrate to grow GaN on, for instance, would be of course another GaN crystal obeying the same symmetry. *Wurtzite* GaN however, and group III nitrides in general, do not occur in nature, and must be obtained using special growth techniques called ultrahigh vacuum (UHV) techniques [71]. Due to their complexity [72], the cost of producing very high quality III-nitride substrates through these techniques is however very high, and hence more cost effective alternatives are usually employed.

As already discussed in section §1.3.2, the most commonly employed substrates for the growth of III-nitride heterostructures are c-plane sapphire (Al_2O_3) crystal and Silicon (111). Although they have the same crystal symmetry, the lattice mismatch between Sapphire (0001) and GaN is 16% [49]. This value increases to 17% for a Silicon (111) - GaN interface. Despite the fact that a higher defect density is expected in the case of a growth on a Silicon

(111) substrate, this material is more interesting for applications since Silicon based technologies can be easily integrated in electronics. In the case of the samples presented in this thesis, both of these substrates have been employed.

The use of UHV techniques for the deposition of semiconductors offers several desirable features. The absence of gas phase interactions allows for precise control of both thickness and composition beyond what can be achieved by other growth methods. In addition, the use of substrate rotation produces excellent uniformity across large areas, up to 4" in diameter [71]. These advantages have *molecular beam epitaxy* (MBE) the dominant method for the growth of a number of semiconductor structures, particularly those which require abrupt interfaces and a high degree of compositional control. For the most part, the samples presented in this thesis have been grown using MBE, by our collaborators. The term "epitaxy" refers to the ordered growth of a crystalline structure on a monocrystalline substrate with similar crystal symmetry. Such a growth doesn't necessarily require the same lattice constant for the substrate and the film (as in the case of GaAs based heterostructures). The epitaxial growth can be realized even in the presence of strain [71]. A schematic representation of an MBE system is shown in Fig. 3.1.

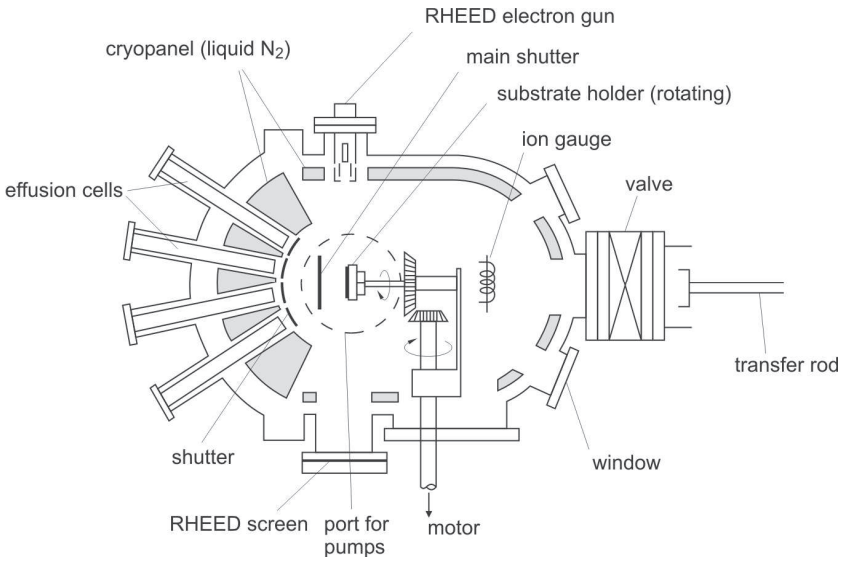

Figure 3.1. Schematic view of an MBE system, taken from ref. [73].

Solid state materials contained in the effusion cells evaporate after being electrically heated. Under UHV conditions, a molecular (or atomic) beam builds from the evaporated materials. The epitaxial film grows from the molecular beams impinging on the substrate, which, for III-nitride compounds, is heated up to around 1000° C. The beams from different sources (cells), which have conic distribution directed to the heated substrate, can be

independently controlled by means of shutters. In the transition from gas-phase to solid-phase, the reciprocal interaction between the molecules causes the crystal formation and the growth takes place. Under optimal conditions, the growth rates, which are typically of the order of ~1 monolayer per second (ML/s), are low enough to allow surface migration of the impinging species and the formation of smooth surfaces. Being such a slow process, the UHV (of the order of 10^{-8} Pa) is a crucial requirement in order to avoid the contamination of the surface with impurities, which would lower the crystalline quality of the film [73]. The homogeneity of the deposited layers along the wafer can be improved by adjusting the growth rate and the substrate holder rotation. The growth rate and crystal quality of the sample can be controlled in-situ with the help of a *Reflection High-Energy Electron Diffraction* (RHEED) cannon. The electron beam produced by this device hits the sample at a very high angle, with respect to the normal, and the real time diffraction figure makes it possible to control the growth with a precision of a single atomic layer. We do not discuss other epitaxial growth techniques that allow for realization of quantum dots, such as Stranski-Krastanov, or techniques such as pendo-epitaxy used for nitrides as it is out of the main scope of the thesis.

3.2. The influence of strain on the design of III-nitride heterostructures

The term "heterostructure" is derived from the concept of "heteroepitaxy", which refers to the growth of different crystalline structures on top of each other on a substrate. Given the fact that there will be a mismatch between the first layer of the heterostructure and the substrate, growers will always have to take into consideration the presence of strain in the structure. In sub-section §1.3.2 we already mentioned how the effects of relaxed and unrelaxed strain can have a crucial impact on the performances of nitride based heterostroctures. We will expand this idea in the following.

Three main types of heterostructures will be discussed in chapters §5 and §6: GaN epilayers, microcavities, and quantum wells.

The epilayer

We name "epilayer" a thick GaN layer (~few μm) grown in order to analyze its optical properties. The growth of the epilayer can be done either directly on the substrate, or by the introduction of several so-called "buffer" layers between the last GaN layer and the substrate

in order to relief the strain caused by the lattice mismatch between the substrate and the buffer layers. The analysis of the optical properties of epilayers obtained under different growth conditions, substrates and/or buffer layers, is a useful tool that allows growers to infer an optimal set of growth parameters for the GaN layers that will serve as active media in microcavities. Results on several epilayers, grown in different conditions and with different structures will be presented in section §5.1.

The microcavity

When tackling the design of a GaN based microcavity, the first issue that arises is the type of active medium that should be used. More specifically, a choice needs to be made between using a layer of bulk GaN or placing several GaN quantum wells (QWs) in the cavity region.

As already discussed in section §1.3, the increased binding energy and oscillator strength of excitons confined in quantum well structures with respect to bulk excitons would suggest a stronger coupling with the cavity photons and a higher temperature stability for the polaritons when the active layer is realized with QWs. At the time this work started however (end of 2005, beginning of 2006), the state of GaN based quantum wells was not too good. Studies of GaN/$Al_xGa_{1-x}N$ QWs showed a huge impact of the piezoelectric field on the excitonic properties of these structures. With the growth techniques and *know-how* available at that time, typical low temperature photoluminescence (PL) linewidths for GaN/AlGaN QWs grown by MBE with Al content between 10% and 30% were around 20 meV when silicon or sapphire were used as substrates [31] [74], as a consequence of strain, interface, and alloy fluctuations. This value was much larger than the one previously obtained for high quality GaN epilayers (<5 meV) at low temperature on the same substrates [39] [75]. For QW heterostructures, such as LEDs, even broader emissions were obtained [76] [77], which questioned the viability of GaN based QWs as active media in semiconductor microcavities at that time. The large inhomogeneous broadening present in GaN/AlGaN QWs at low temperature was a cause of concern, as the additional thermal broadening of the excitonic recombination at room temperature would not allow the existence of a strong coupling between the exciton and photon modes. Moreover, as a result of the polarization field effect, the exciton oscillator strength was found to decrease dramatically with the increase of the QW width, below the values measured for excitons in bulk GaN [78]. Finally, the spatial separation of the carriers in the conduction and valence bands caused by the QCSE results in a

reduced radiative recombination rate, and a reduced optical efficiency of the structure (see section §1.3.2).

In order to eliminate the piezoelectric polarization caused by the mismatch between the barrier layers and the well layer, the incorporation of In in the barriers was considered as a possible solution to obtain lattice matched interfaces. Unfortunately, the emission broadening of $In_xAl_yGa_{1-x-y}N$ quaternary alloys proved to be very high (several tens of meV [79] [80]) even for very low In contents, showing the large alloy potential fluctuation due to the compositional inhomogeneity in the presence of indium [51]. Given these considerations, the option of realizing a GaN based QW microcavity exhibiting strong coupling at room temperature was discarded in favour of a bulk GaN structure.

The second issue concerning the design of a GaN microcavity was the structure of the DBRs. Once again, a decision had to be made between using $Al_xGa_{1-x}N/Al_yGa_{1-y}N$ DBRs, or using lattice matched DBRs by incorporating indium in the DBR with a higher band gap in order to reduce its lattice constant. As discussed in the previous paragraph, the option of using In in such a structure would only lead to very large band gap variations of the respective layers, which would decrease the optical quality of the mirrors and introduce an additional broadening of the cavity mode, thus lowering the quality factor of the resonator and decreasing the photon lifetime in the cavity. Moreover, the reduced refractive index contrast between lattice matched $Al_xGa_{1-x}N/In_yAl_zGa_{1-y-z}N$ layers would give rise to a reduced stop band that would render the probing of the energy dispersion of the polariton modes quite difficult. Hence, for the samples discussed in chapter §5 starting with section §5.2, the chosen materials for the realization of the DBRs were $AlN/Al_{0.2}Ga_{0.8}N$ $\lambda/4$ layers. Due to a difference of ~2.75 eV between the band gaps of these materials, a high refractive index contrast is assured resulting in a large stop band that allows a simple extraction of the polariton dispersion curves from angle resolved measurements (see section §2.3).

Finally, the choice of the substrate and buffer layers was made keeping in mind the practical purposes of the microcavity. Although the growth on a Si (111) substrate introduces a larger tensile strain than a Sapphire (0001) substrate due to the higher difference of thermal expansion coefficients, silicon substrates have several advantages such as large-size wafers, lower cost, and good electrical conductivity combined with easy realization of ohmic contacts [81] - [83], which make them favourite for optical and electronic applications. Also, should further processing of the microcavity structure be necessary, the removal of the substrate through common etching processes is much easier for silicon than for sapphire, which is an insulator. Given these practical considerations, the microcavity and the related

heterostructures were deposited directly on a Si (111) substrate, without using any buffer layer.

The quantum wells

The study of GaN/AlGaN quantum wells with low Al content in the barriers was triggered by the limitations exhibited by the bulk GaN microcavity (see chapter §5). The feedback provided to the growers during the stages that ultimately led to the realization of a bulk GaN microcavity in the strong coupling regime proved useful in acquiring a *know-how* on the optimization of growth parameters for GaN heterostructures. As strain was *a priori* a limiting factor of these devices, the control of its effects took a few years to master. In the meantime, the growth of GaN/AlGaN exhibited significant progress in the sense of reducing emission linewidth and controlling the QCSE in these structures, which revived the interest of using them as active media in GaN based microcavities. The significant reduction of several negative effects caused by strain and the presence of polarization, which were discussed in the previous paragraphs, made possible the study of a whole new dimension of physical phenomena that could not be observed previously in similar quantum well structures. A detailed study of these state-of-the-art GaN/AlGaN QWs is provided in chapter §6.

3.3. Conclusions of the chapter

In this short chapter we outlined the limiting factors that determined the design and evolution of nitride based heterostructures, from epilayers and DBRs, to complete microcavities in the strong coupling regime and state-of-the-art quantum wells. The results presented in chapters §5 and §6 provided growers a continuous feedback that helped them for the achievement of more complete and higher quality heterostructures.

4. Experimental systems

Physical processes observed in semiconductor heterostructures need to be studied in both time and energy domain. The analysis of the samples presented in chapters §5 and §6 was conducted using two optical spectroscopy investigation techniques: *reflectivity* and *photoluminescence* (PL). For each of these techniques, we will start by referring to the underlying phenomena that allows us to extract relevant information about the physics of our system through these experimental techniques. Afterwards we will describe the setups used to carry out various types of measurements.

4.1. Reflectivity

The principle of a reflectivity measurement is very simple: we illuminate the sample with a beam of light having a sufficiently broad emission spectrum in order to cover all the spectral features of interest; then we measure the intensity of the reflected light as a function of wavelength (energy).

Reflectivity is one of the standard techniques for spectroscopy of intrinsic excitons. This means that only resonances associated with the transitions of free excitons can be probed with this technique. Hence, the features present in the reflectivity spectra can be assigned to the absorption of light by electric dipoles present in the material (at energy positions corresponding to the free excitonic transitions), which are not subject to localization effects.

Although different geometries should be used to characterize the selection rules and polarization properties of free excitons [84], the investigation of the fine structure for the samples presented in the following chapters is beyond the scope of this thesis, and hence for our measurements an unpolarized geometry was employed.

We would like to stress out at this point several problems of reflectivity measurements that may prevent a correct interpretation of the data without a proper correlation with photoluminescence spectra. In the case of nitride based heterostructures, the exact spectral positions and shapes of the features observable in reflectivity have been found to be strongly dependent on the strain present in the various samples [40] [66] [84] - [88]. Hence, the fitting

of these spectra often requires the use of more than just a simple Lorentz oscillator model to describe the exciton (see eq. (56)). Instead, either analytical [89] [90] or semi-empirical [66] models are used to account for the influence of strain on the variation of the dielectric constant $\varepsilon(k,\omega)$. Moreover, in the case of microcavity polaritons, existence of a structure in reflectivity does not make the distinction between absorption and a change in the reflectivity/transmission balance [30], and hence reflectivity spectra should be interpreted carefully.

4.2. Photoluminescence

The measurement of light emission resulting from the radiative recombination of photoexcited carriers, *i. e.* photoluminescence, is a fundamental tool for the study of physical processes in crystals. In a semiconductor non equilibrium carriers can be excited by means of light absorption, usually from a coherent light source such a laser (see Fig. 4.1). These carriers (namely electrons), excited above the electronic state with the lowest energy, relax towards this state losing energy, typically by phonon interactions. The carrier relaxation can be classified into four temporally overlapping regimes, occurring on different time scales [91]. First, we have a *coherent regime*, which occurs on a sub-picosecond scale, corresponding to the excitation of the semiconductor with an ultrashort laser pulse. In this regime there is a well-defined phase relationship between the carriers that are created at high k and the electromagnetic field that created the excitation. The destruction of this coherence through dephasing is a very fast process in semiconductors, giving rise to a *non-thermal regime* which takes place on a picosecond scale. Various processes such as carrier-carrier or exciton-exciton scattering will bring the non-thermal distribution to a hot, thermalized distribution that defines the *hot-carrier regime*. The carrier temperature in this regime can be, and usually is, higher than the lattice temperature. The thermalization times depend strongly on many factors, such as carrier density and material type, and usually occur on a time scale of 1 - 100 ps. The processes that dominate this regime are hot-carrier - phonon interactions, decay of optical phonons, and carrier - acoustic phonon scattering. Finally, in the *isothermal regime* the excess of electrons and holes, compared to the thermodynamic equilibrium, will recombine either radiatively or non-radiatively, returning the semiconductor to the thermodynamic equilibrium and giving rise to the PL signal.

The time scale for each event depends very strongly on parameters such as band structure, excess energy, the nature of the excitation (free carrier vs. exciton), the density of excitation, the lattice temperature and so on. While the carrier relaxation processes in GaAs nanostructures, for instance, take place on a time scale of the order of several hundreds of picoseconds [91], in the following chapters we will see that the radiative recombination of carriers is much faster for GaN based heterostructures, suggesting a very efficient energy relaxation of the carriers, especially in the hot-carrier regime.

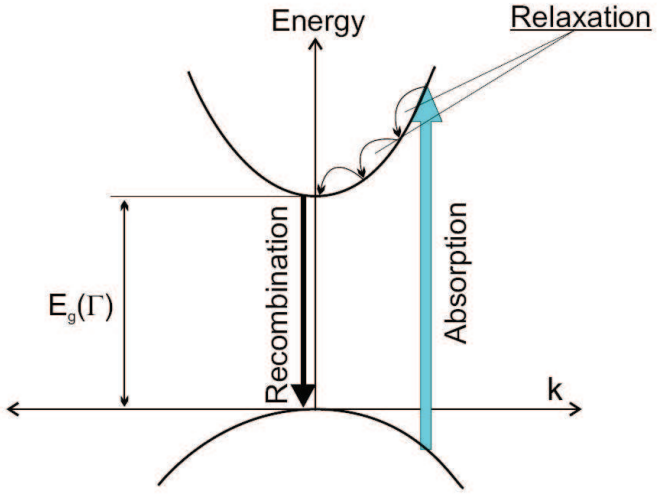

Figure 4.1. Schematic representation of the excitation, relaxation, and recombination processes in PL measurements.

Fig. 4.1 is a simplified picture of the main processes involved in the photoluminescence mechanism. As discussed in the previous chapters, there are several factors that affect the recombination of electrons in the conduction band with holes in the valence band. They range from extrinsic effects related to the properties of the material, such as localization of the emission due to the presence of impurities and defects or variation of the energy gap caused by the presence of strain, to effects induced as a consequence of carrier confinement or coupling of the excitons with a photon field. These effects must be equally taken into account when analyzing the emission spectra of a sample. We will give a brief description of the recombination processes for the main types of samples presented in this work.

Bulk PL

The typical mechanisms involved in the recombination processes in a bulk semiconductor material after a non-resonant excitation can be generally described by the picture presented in Fig. 4.2.

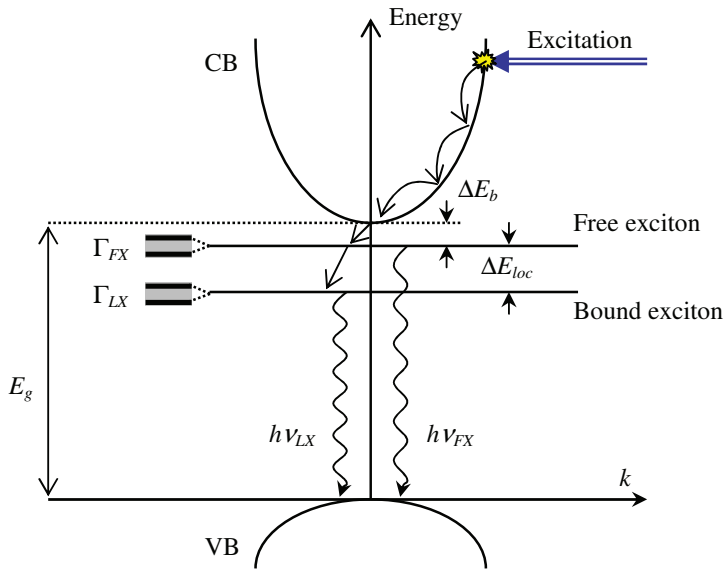

Figure 4.2. Schematic of the recombination process in a bulk semiconductor.

The measurement of photoluminescence is perhaps the simplest and most direct way to gain access to the optical properties of a semiconductor. The light source usually employed to carry out the excitation of the medium is a laser source tuned at a significantly higher energy than the band gap of the material that we want to probe ($h\nu_{exc} >> E_g$). As mentioned before, the carriers (electrons/holes) created at high k after the absorption of the exciting photons will quickly relax towards the Γ point of the k space after losing their energy through various types of interactions, described in the previous paragraphs. At this point the carriers in the conduction band will spend a certain amount of energy ΔE_b to couple with holes in the valence band giving rise to *free excitons*. Depending on the quality of the bulk material, but also on the lattice temperature, free excitons can mainly undergo several processes: (i) radiative recombination resulting in the emission of a photon $h\nu_{FX}$; (ii) localization of the exciton at an impurity or an imperfection of the crystalline lattice followed by the emission from, e. g., a donor-bound DBE or an acceptor-bound exciton ABE (see section §1.2); (iii) non-radiative recombination with various types of structural defects. For high quality samples, the radiative recombination of the free excitons will be dominant with respect to the other processes. Conversely, for materials with low optical quality and a high density of structural

defects, the non-radiative mechanisms and localization effects will dominate the recombination process.

As discussed in section §1.2, optical transitions are subject to various broadening mechanisms, so that radiative recombination bands in the PL spectra are characterized by a certain spectral width (Γ_{FX} and Γ_{LX} in Fig. 4.2). The presence of structural defects caused by strain, impurities, and fluctuations of the band gap gives the inhomogeneous contribution Γ_{inh} to the total broadening Γ_{tot}, while the interaction with acoustic phonons gives a homogeneous contribution Γ_{hom} which is proportional to $k_B T$. Thus, the total broadening of a recombination band is a convolution of the two contributions:

$$\Gamma_{tot} = \Gamma_{inh} \otimes \Gamma_{hom} \tag{66}$$

The inhomogeneous broadening, dominant at low *T*, is best described by a Gaussian line shape, while the homogeneous contribution increases with temperature and is generally accounted for by considering a Lorentzian distribution, so that the recombination bands in the PL spectra assumes a Voigt profile [92].

Increasing the lattice temperature can result in strong modifications of the recombination dynamics. Namely, if Γ_{hom} becomes comparable to the localization energy of free excitons ΔE_{loc}, the interaction of the localized states with acoustic phonons, which is a much faster process than the radiative recombination, will result in a *delocalization* of the emission of the bound states due to the energy transfer from the phonons. Further increase of Γ_{hom} to values comparable to the exciton binding energy ΔE_b will result in the population of the *continuum of states* in the conduction band, which is not discretized and obeys a Boltzmann distribution of states. In this case an ionization of the exciton occurs. The radiative recombination of the electrons from the continuum with the holes in the valence band gives rise to a *thermal tail* on the higher energy side of the PL band, with a contribution proportional to $\exp(-E/k_B T)$.

The recombination kinetics of excitons can be described by rate equations that need to account for all the contributions of radiative or non-radiative recombination processes, which depend on the optical quality of the material. For materials with high optical quality, the radiative recombination of exciton molecules (biexcitons) also needs to be considered, as it can give a significant contribution to the PL spectrum. Moreover, the exchange of interaction

between the biexciton and exciton populations can result in a strong modification of their recombination rates. These rates can be extracted through the measurement of decay times of the various spectral features observable in the time-resolved photoluminescence spectra, and the assignment of these features must be made in correlation with their energy positions and taking into account the various broadening and localization mechanisms.

Quantum well PL

All the mechanisms that affect the recombination of excitons in a bulk semiconductor also apply in the case of quantum wells. In Fig. 4.3 we give a schematic description of the recombination mechanism in a QW following a non-resonant excitation, without including the effects described in the previous subsection.

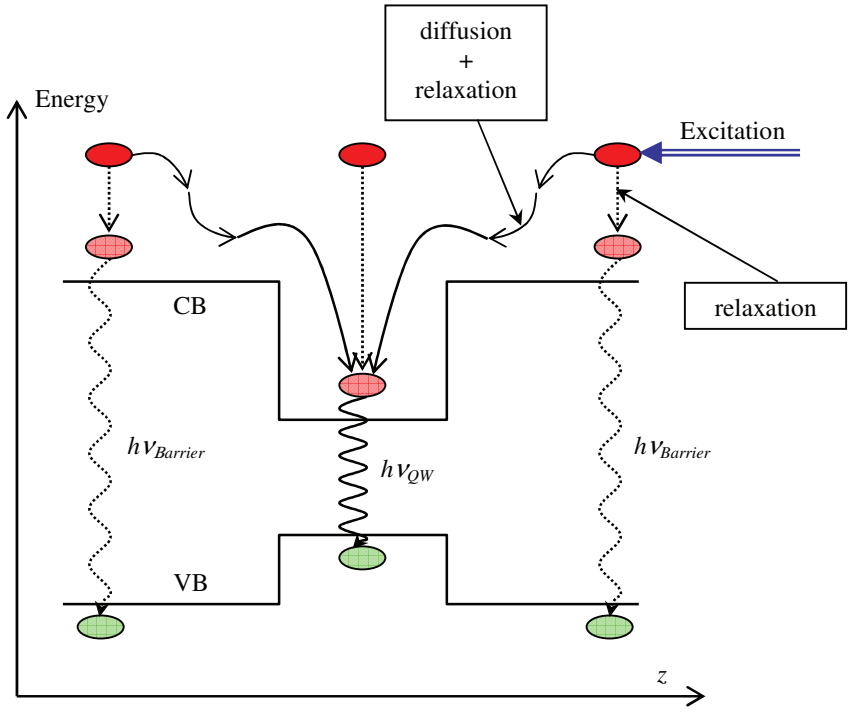

Figure 4.3. Representation of the exciton recombination process in a QW.

In the case of a QW structure, the non-resonant excitation is usually carried out with a laser pulse having a higher energy than the band gap of the barrier layers. In this way carriers are created throughout the heterostructure, in both the well and the barrier regions. Carriers created in the well region at high k relax very quickly towards the Γ region of the k space through interactions with phonons, where they are subject to all the effects discussed for bulk excitons. However, the effect of discretization of their energy levels due to the presence of

confinement and QCSE due to the strong polarization present in nitride heterostructures, which were described in section §1.3, also need to be considered. For the carriers created at high k in the barriers however, two relaxation mechanisms become possible. First, a relaxation towards the Γ region of the barrier's k space is possible, where they couple with holes in the valence band giving rise to 3D excitons. The radiative recombination of these excitons will give a "bulk" contribution in the PL spectra. However, this relaxation mechanism is not dominant. For the most part, carriers injected into the barrier region of a high-quality quantum well structure are eventually captured into the quantum wells, through a combined relaxation and diffusion process, because the QW states represent the lowest energy state of the system. The capture from the barrier into the well is mediated primarily by the emission of optical phonons [91]. The transport of carriers in quantum wells has been described as an exchange of phonons between the 2D and 3D electrons which supply the necessary momentum difference in the direction perpendicular to the well [93]. The study of these phenomena is not the scope of this thesis. We would like however to underline that the rate at which hot carriers are captured by the quantum well is much higher than the rate for relaxation to form 3D excitons in the barriers. First, as a result of the very efficient capture process, the contribution from the radiative recombination of QW excitons in the PL spectra is much higher than the contribution given by the recombination of "bulk" barrier excitons. Second, since the barrier is usually made of a ternary alloy, such as $Al_xGa_{1-x}N$, it will have a lower crystalline quality than the binary GaN that makes up the well region, resulting in a reduced optical efficiency.

Polariton PL

The excitation and relaxation mechanisms of microcavity polaritons along the two polariton branches are graphically depicted in Fig. 4.4. In the case of non-resonant excitation, a high energy laser pulse is used to populate the electron-hole continuum with a free carrier thermal reservoir. The population of the two polariton branches comes as a result of various scattering processes, mainly by acoustic and optical phonons emission or absorption [7]. High wave vector (k) excitons in the thermal region (TR) relax towards the strong coupling region (SCR) and populate the LP and UP branches mainly by emission and absorption of acoustic phonons, respectively. However, at low temperature and for low excitation power densities, the acoustic phonon scattering rate into polariton states corresponding to the strong coupling regime ($k \leq 5\text{-}6 \times 10^4$ cm^{-1}) are small due to the large energy transfer required compared to the typical acoustic phonon energies, which gives rise to a bottleneck region (BR). Polaritons

undergo radiative recombination in this region due to the fact that their escape rate from the cavity is shorter than the scattering rate into lower *k* states. The study of the "bottleneck" effect in a bulk GaN microcavity will be detailed in the following chapter.

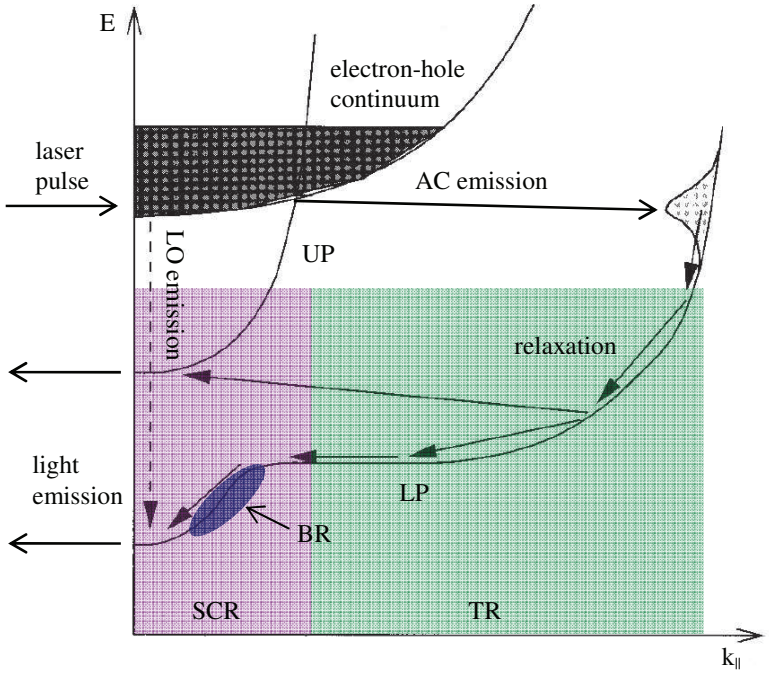

Figure 4.4. Graphical representation of the polariton dispersion curves and their population through various scattering mechanisms [7]. UP: upper polariton; LP: lower polariton; TR: thermal reservoir (green); SCR: strong coupling region (magenta); BR: bottleneck region (violet). AC and LO indicate acoustic phonon and longitudinal optical phonon processes, respectively.

The radiative recombination of polaritons from the various optically accessible *k* states of the LP and UP branches is governed by their escape times out of the microcavity, which are related to their respective exciton and photon fractions. Therefore, we can describe the luminescence process just by the knowledge of the distribution of the cavity polaritons along the dispersion curves, and by the outside transmission coefficient of such cavity polaritons. If we assume no broadening mechanism, as both the exciton and the cavity mode energies only depend on $k_{\parallel}$, the in-plane *k* selection rule reduces the photoluminescence spectrum to a sum of two delta functions [3]:

$$I(E,\theta_{out})\mathrm{d}\Omega_{out} = \sum_{i=LP,UP} I_i(E,\theta_{in})\delta(E - E(\vec{q}\sin\theta_{out}))\mathrm{d}\Omega_{in}, \qquad (67)$$

where the sum is over the upper and lower branch of the polariton, the propagation directions θ_{in} and θ_{out} and solid angles $d\Omega_{in}$ and $d\Omega_{out}$ are related by the Snell-Descartes law, and $\vec{q}$ is the photon wave vector. Therefore, the emission spectrum for a fixed incidence angle exhibits two lines whose positions are directly related to the cavity polariton dispersion curve. In the presence of homogeneous or inhomogeneous broadening the delta functions are replaced by Lorentzian or Gaussian line shapes, but their energy position is not changed as long as the broadening is smaller than the energy separation of both lines. This allows us to extract the dispersion curves of the cavity polariton from angle-resolved photoluminescence spectra of a semiconductor microcavity in the strong coupling regime [3].

4.3. Experimental setups

Three main types of experimental techniques were used for the optical characterization of the various types of samples: reflectivity, time integrated photoluminescence (TI-PL), and time resolved photoluminescence (TR-PL). Measurements were performed as a function of sample temperature, position of the excitation spot on the sample, excitation energy/density, and angle. All these measurements require a system that is primarily made up by an excitation source (CW lamp for reflectivity, laser for PL), optics used as wave guides (lenses, mirrors, filters, beam splitters, optical fiber), a cryogenic system that allows the control of the sample temperature, and an acquisition system made up by a spectrometer and a detector (charged coupled display (CCD) for reflectivity and TI-PL, or Streak camera for TR-PL). We will give a description of the main setups used for the optical investigation of the samples presented in the following chapters.

Reflectivity and/or TI-PL

A simple setup that is particularly interesting in the sense that it allows us to measure simultaneously the reflectivity and TI-PL in the same spot of the sample is presented in Fig. 4.5.

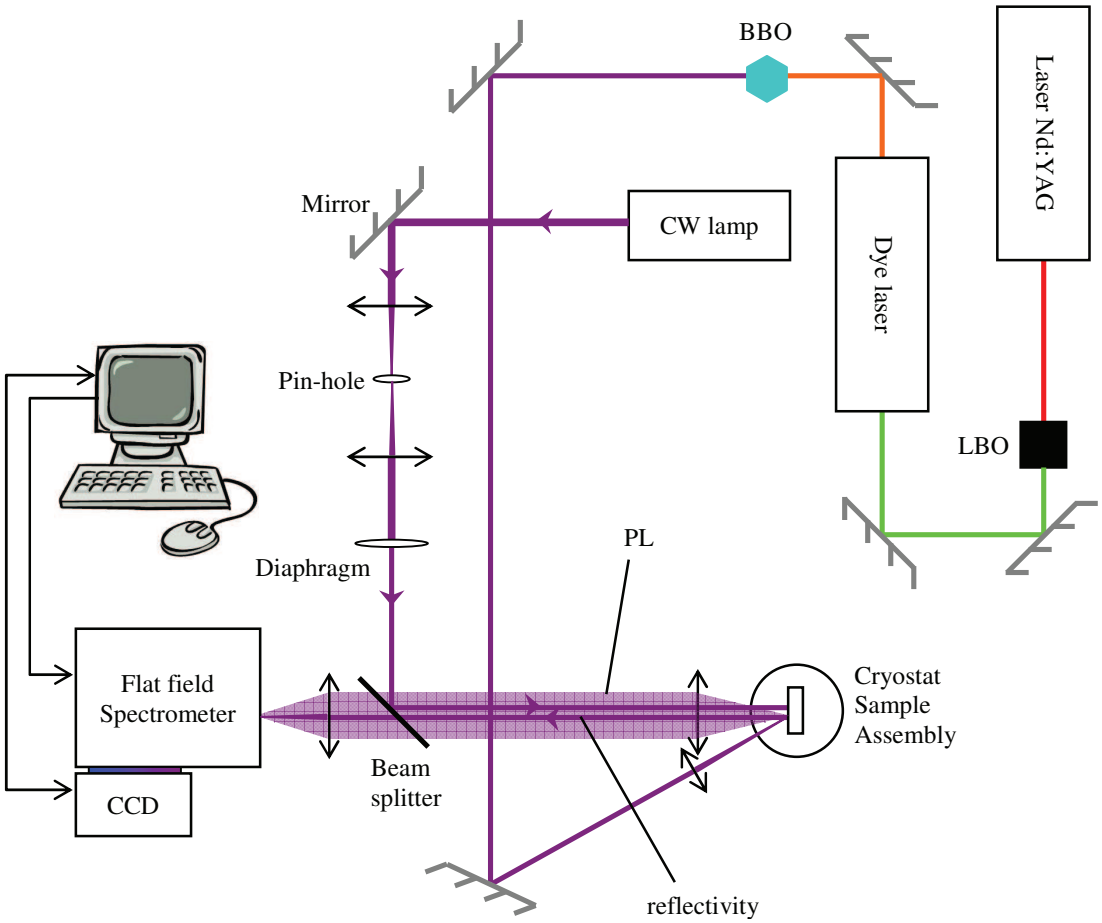

Figure 4.5. Experimental setup for the simultaneous measurement of reflectivity and TI-PL.

For the PL measurement, the excitation is provided by a Q-switched Nd:YAG solid state laser generating pulses at a wavelength of 1064 nm, with a pulse duration of ~100 ps at a repetition rate of 76 MHz. The infrared laser beam is doubled in frequency (532 nm) by a non-linear LBO crystal. The resulting green beam is used to pump a dye laser (Rhodamine 6G) which in our case is tuned to generate laser pulses at a wavelength of ~600 nm having a duration of 3 ps. This beam is doubled in frequency by a non-linear BBO crystal (~300 nm) and is used for the excitation of the sample.

For the measurement of reflectivity, the excitation is provided by a CW lamp having a broad emission band in the UV region. Through a convenient use of optics, the excitation beams from both of these sources can be focused on the same spot on the sample, allowing the measurement of its photoluminescence and reflectivity at normal incidence. The emitted light is collected through the same system of optics for both signals and focus on the entrance slit of a spectrometer. The spectral resolution of this system is ~1 meV, which is well below the spectral width of the excitonic features that we want to probe.

Angle-resolved PL

As mentioned in the previous subsection, the energy curves of the cavity polariton can be obtained by extracting the energy positions of the polariton peaks in angle-resolved PL spectra. This is achieved using the setup presented in Fig. 4.6.

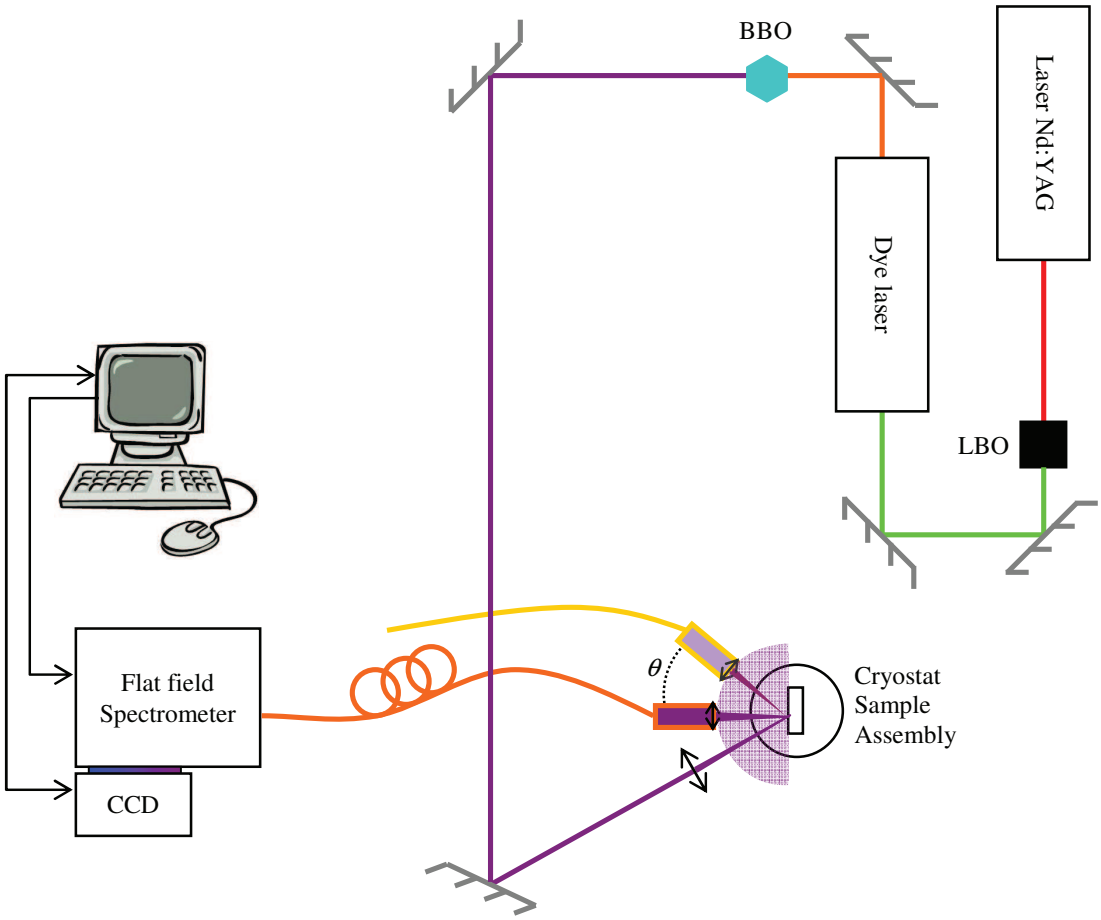

Figure 4.6. Experimental setup for the measurement of angle-resolved TI-PL.

For the excitation of the sample we use the same laser system described in the previous setup. The peculiarity of this setup is the collection of the optical signal, which in this case is done by an optical fiber system mounted on a rotating arm. Although the PL from the sample is emitted in π solid angle, the limited aperture of the objective used to collect the emitted light (2°) and to focus it in the core of the optical fiber allows us to probe light emitted in small solid angles. The external emission angle θ is varied by rotating the arm on which the fiber is mounted. By measuring the optical signal at each angle θ and identifying the polariton peaks in the resulting TI-PL spectra we can achieve a reconstruction of the polariton dispersion curves as a function of θ, which is related to $k_{\parallel}$ through eq. (53).

TR-PL

A different system is needed to characterize the fast recombination dynamics of the PL signal. This system is described in Fig. 4.7.

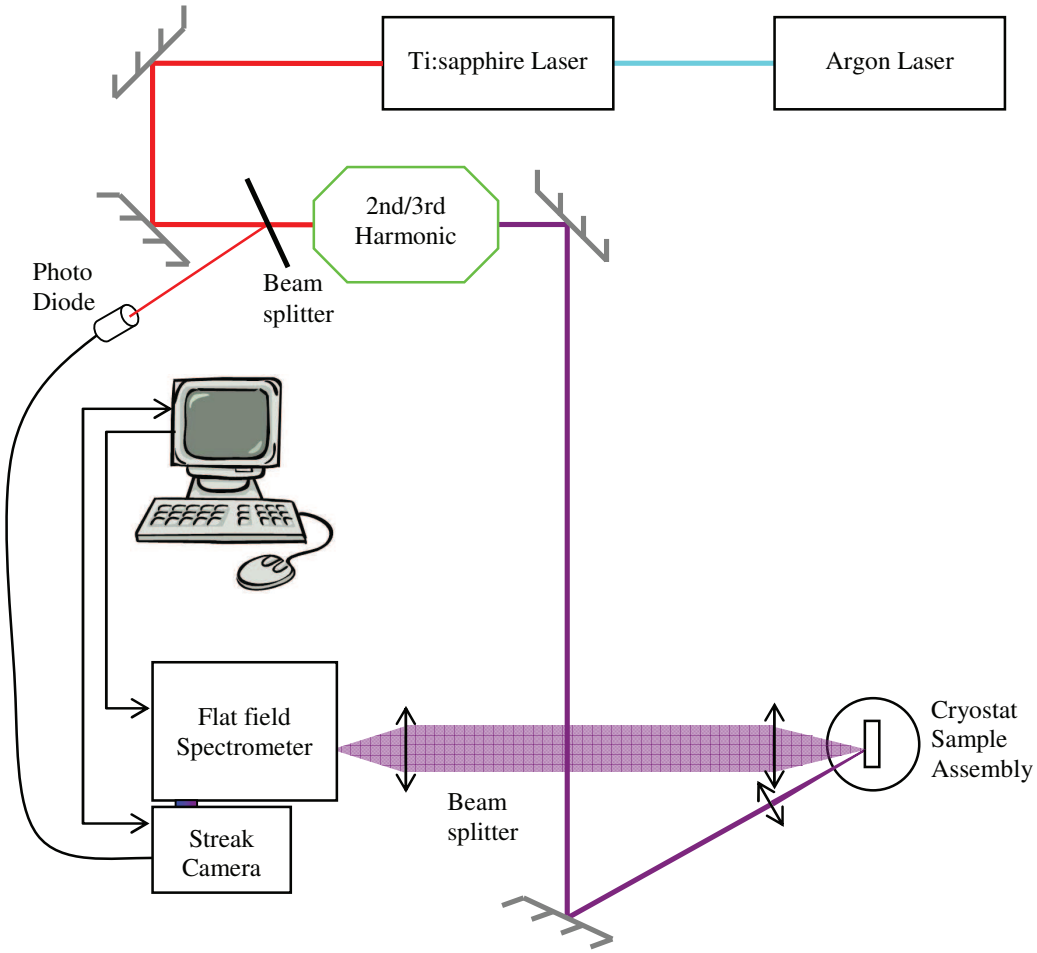

Figure 4.7. Experimental setup for the measurement of TR-PL.

The excitation mechanism is similar to the one used for the measurement of TI-PL, however the detection system can reveal the intensity of the PL signal as a function of wavelength (energy), as well as time. The beam generated by a CW Argon laser is used for the optical pumping of a *mode-locked* Ti:sapphire laser, which is tunable in the range 700 ÷ 900 nm, and has a pulse duration of 1.2 ps at a repetition rate of 81 MHz. A photodiode is used to synchronize the phase of the laser beam with the streak camera. A system of non-linear crystal(s) is used to generate either the 2nd or the 3rd harmonic of the beam emitted by the Ti:sapphire laser, depending on the optical properties that we want to investigate. This beam is then focused on the sample, much like in the setup described for the TI-PL

measurement, while the collected PL signal is similarly focused on the entrance slit of a flat field spectrometer. The detection of the signal is done with the use of a streak camera, giving us access to the recombination dynamics in the selected spectral region.

The instrumental resolution of this system is approximately 1 meV in energy, while for the time axis the resolution is ~4 ps.

5. Bulk GaN microcavities and related structures

In this chapter we will discuss the evolution of GaN based heterostructures that culminated with the achievement of a bulk GaN microcavity in the strong coupling regime. All the samples that will be presented in this chapter were provided to us by our colleagues at the CHREA-CNRS research center in Valbonne, France, as part of a project related to the study of polariton emission and strong coupling in GaN based microcavities, supported by E.U. funding. We will start by briefly discussing the influence of the sample structure on the resulting optical quality of several GaN epilayers (section §5.1). Then we will describe the evolution of GaN based microcavities, from the DBR (section §5.2) and the half-cavity (section §5.3), to the complete microcavity in weak coupling (section §5.4) and strong coupling regime (section §5.5). In section §5.5 we will discuss several aspects of the strong coupling regime and polariton recombination kinetics in a bulk λ/2 GaN microcavity.

5.1. The GaN epilayer

As mentioned in section §3.2, the quality of the λ/2 layer of GaN acting as active medium inside the microcavity is a crucial element in the achievement of strong coupling in such a structure. While tensile strain between the active GaN layer and the underlying DBR layers cannot be eliminated, the defect density introduced during the growth process should be low enough to give rise to a small inhomogeneous broadening of the exciton in PL and a low concentration of non-radiative recombination centers that would otherwise inhibit the achievement of the strong coupling regime.

The results presented in this subsection refer to four samples with different substrate and/or buffer choice, all grown by MBE. The idea is to illustrate the influence of the substrate and buffer choice on the resulting optical quality of the epilayer. A schematic representation of the structure of these four samples is given in Fig. 5.1. As can be seen, three out of four of these samples have some sort of buffer layer introduced in order to relief the strain caused by the lattice mismatch between the substrate and the epilayer.

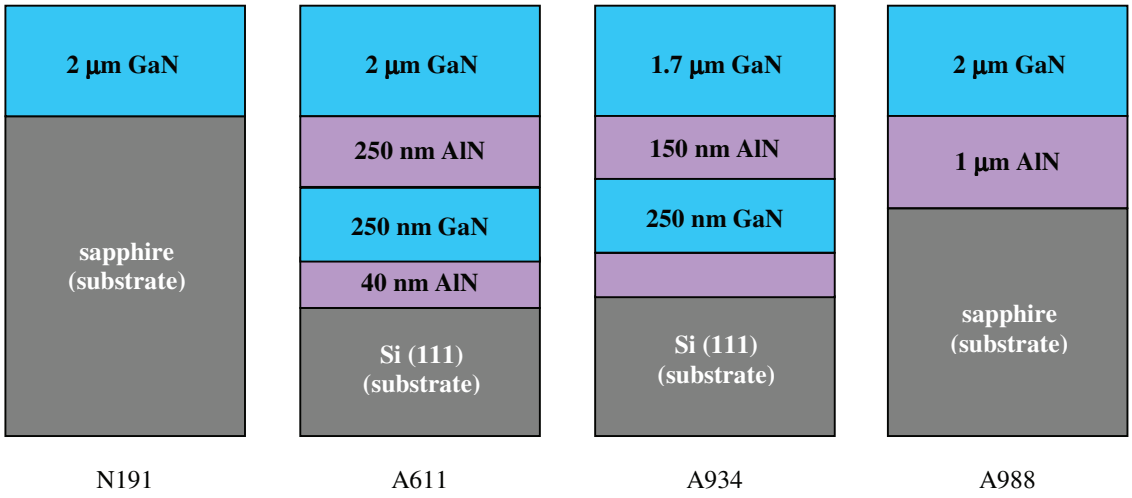

Figure 5.1. Schematic representation of the structure of four GaN epilayers with different substrate and/or buffer layers.

The optical quality of the four epilayers presented in Fig. 5.1 was checked through TR PL measurements, giving us access to the exciton recombination kinetics in these samples. These results helped growers to understand which design and growth parameters were more appropriate for the growth of a higher quality GaN active medium on an underlying DBR.

In Fig. 5.2 we show in semi-logarithmic scale the TR PL spectra corresponding to each of the four epilayers at a temperature of 10 K. The spectra were recorded using the streak camera apparatus using the setup described in section §4.3. The non-resonant excitation of the samples was carried out using the 3rd harmonic of the Ti:sapphire laser (~280 nm), with an excitation power density of approximately 3.5 W/cm^2. The time window between each individual spectrum is 70 ps. In Fig. 5.2, the bands designated with FX correspond to the recombination of the free exciton, while the LX bands correspond to various types of localized recombinations. We will not discuss the spectral features observable at higher energies than the FX recombination band. The corresponding LO bands in the lower energy side of the spectra are the respective optical phonon replica of the various types of recombinations. These emissions are due to the interaction of the exciton with the crystalline lattice. The energy difference between the exciton bands and their corresponding phonon replicas is equal to the energy of the phonon involved in the interaction, which in the case of GaN is of the order of 90 meV. The peculiarity of the LO bands resides in the fact that their recombination kinetics reproduce very precisely those of their respective exciton bands. Given the fact that these bands are generally associated to the free exciton recombination (see Fig. 5.2), and are hence mainly unaffected by the presence of a localized exciton emission

band, the lifetime of the free exciton can be extracted directly from the decay time of its associated LO band [93].

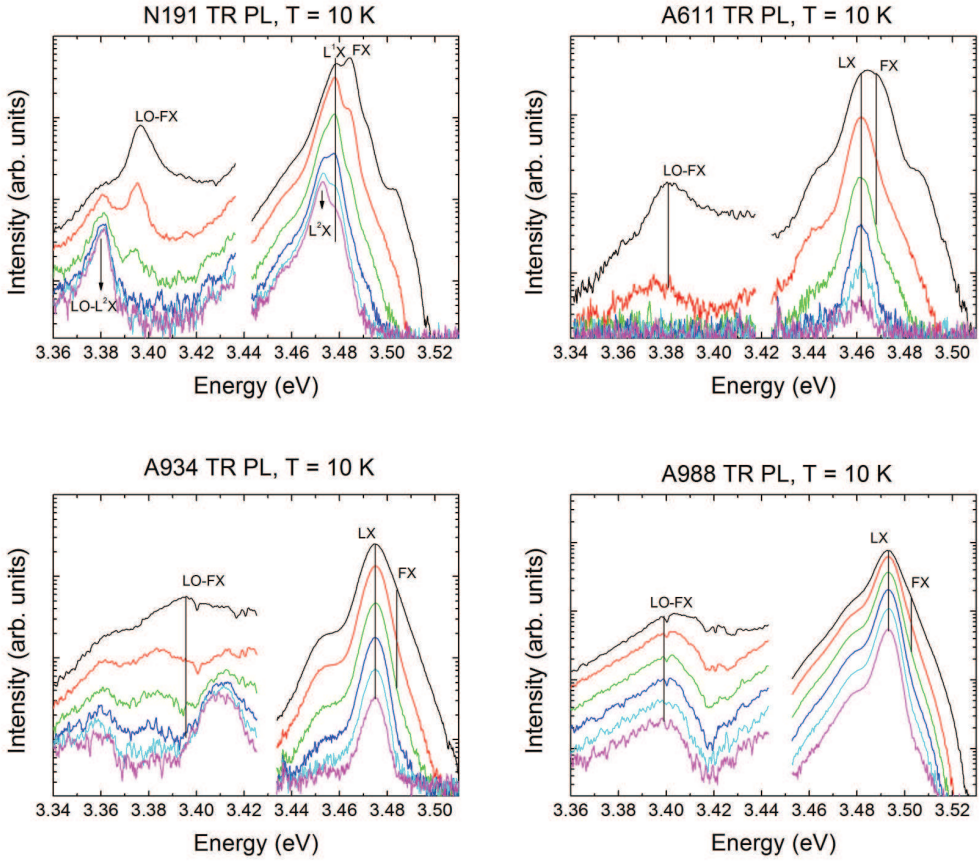

Figure. 5.2. Semi-logarithmic representation of the TR PL spectra at T = 10 K for the samples described in Fig. 5.1, with a time window of 70 ps. The intensity scale of the phonon replicas (lower energy) is different from that of the main excitonic emission (higher energy). Spectra are shifted in intensity for a clear viewing.

The results presented in Fig. 5.2 can be summarized as follows:

- All samples exhibit similar features such as a recombination of the free (FX) and localized (LX) *A* exciton, as well as the optical phonon replica of the free *A* exciton (LO-FX). The recombination band LX in these samples is most likely caused by the presence of impurities. An additional localized exciton recombination (L^2X) can be seen in sample N191, along with its phonon replica LO-L^2X. For a general review of the different kinds of exciton recombinations in GaN see Ref. [93].
- As a result of the different values of the tensile strain present in the epilayers, the emission of the FX appears at different values in the range of 3.468 - 3.502 eV

(3.478 eV for N191, 3.468 eV for A611, 3.484 for A934, and 3.502 eV for A988). The FX emission has been determined with an error of ±1 meV. The emission energy variation of ~34 meV between different samples caused by strain effects is not trivial and must be very well accounted for when deciding the energy at which the cavity should be in resonance with the active medium, and hence the effective thickness of the λ/4 layers making up the DBRs.

- There are also non-trivial differences in the emission linewidths. The FWHM of the FX in sample N191 is 6 meV, denoting a very small inhomogeneous broadening. In the other samples the inhomogeneous broadening is far greater and hard to estimate due to the presence of the localized emission, denoting a lower optical quality of the sample. The huge inhomogeneous broadening is also clearly visible in the phonon replicas.
- The decay times of the FX recombinations are hard to estimate at this point due to the significant contribution of the LX emissions that remain dominant at longer delays.

Following the PL mechanism described for bulk semiconductors in section §4.2, in order to gain access to the decay times of the free exciton emission a solution would be to increase the temperature of the sample to a value comparable to the localization energy of the LX recombination band. In Fig. 5.3 we present in semi-logarithmic scale the change in the PL spectra of the sample N191 at short delay (70 ps) after increasing the temperature from 10 K to 60 K. The temperature increase results in the disappearance of the localized emission bands (L^1X and L^2X), and consequently of the phonon replica LO- L^2X. A small red-shift of the FX emission band is also noticeable as a result of the reduction of the material band gap with increasing temperature (see eq. (3)).

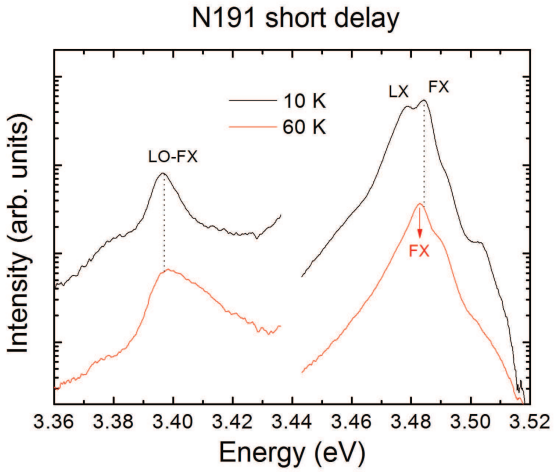

Figure 5.3. Semi-logarithmic representation of the PL for sample N191 at short delays for T = 10 K and T = 60 K. Spectra are shifted for a clearer viewing.

The disappearance of the localized emission band and the red-shift of the FX band are also visible in the other three epilayers (not shown here). For all samples, a broadening of the free exciton emission can be observed. At T = 60 K, the measured FWHMs of the FX bands in the four samples are: 8.9 meV for N191, 13.8 meV for A611, 18.3 meV for A934, and 16.2 meV for A988 (±0.3 meV). The differences between the broadenings are about of a factor 2 at 60 K, which denotes once again major discrepancies in the crystalline quality of the epilayers.

Finally, due to the disappearance of the localized sidebands at T = 60 K, the radiative lifetimes (τ) of the free exciton recombination bands can be properly extracted from their PL decay profiles. The decay profiles of the FX recombination bands are presented in Fig. 5.4 in semi-logarithmic scale (with peak intensities normalized to unity), and were found to be identical to those of their corresponding phonon replicas. The recombination lifetimes of the FX bands are extracted from their decay profiles following a fitting procedure which assumes an exponential decay of the free exciton populations.

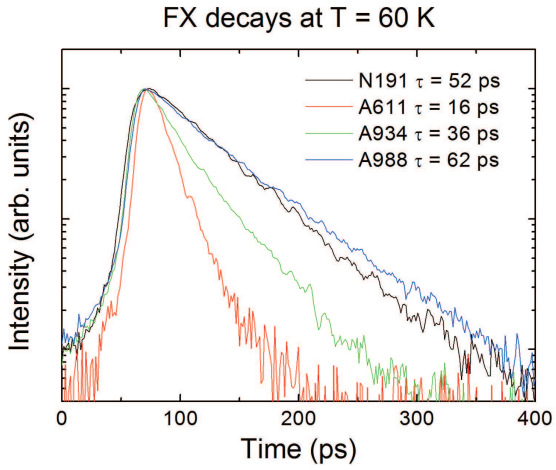

Figure 5.4. Free exciton decay profiles in semi-logarithmic scale for all samples. Intensities are normalized for a clearer viewing.

Once again, the differences found between the free exciton lifetimes for the various samples suggest that the growth conditions have a huge impact on the presence of non-radiative recombination centers in the resulting heterostructures. A summary of the various parameters characterizing the free exciton emission band at T = 60 K of the four samples that we discussed in this section is presented in Table 5.1.

Parameters	N191	A611	A934	A988
FX energy (±1 meV)	3.483 eV	3.466 eV	3.476 eV	3.493 eV
FX FWHM (±0.3 meV)	8.9 meV	13.8 meV	18.3 meV	16.2 meV
FX lifetime τ (±1 ps)	52 ps	16 ps	36 ps	62 ps

Table 5.1. Summary of the free exciton emission energy, FWHM, and lifetime τ at T = 60 K for the four epilayers discussed in the section.

Following the results presented in Table 5.1, it becomes obvious that the growth conditions and the choice of substrates and/or buffer layers can have a decisive impact on the optical quality of a nitride based heterostructure. The main conclusion that can be drawn from these results is that the inclusion of buffer layers between the substrate and epilayer will inevitably increase the inhomogeneous broadening of the free exciton emission. The increase in broadening is mainly caused by the huge number of threading dislocations that appear at the interfaces between two unmatched layers of a nitride-based heterostructure [49]. These dislocations propagate parallel to the growth direction causing large variations of the epilayer band gap and giving rise to a high density of structural defects. As a consequence, the

broadening of the FX recombination band of sample N191 is smaller with respect to the other samples.

Given the restrictions that apply to the broadening of the exciton and photon modes in order to observe the strong coupling in a semiconductor microcavity (see section §2.4), it is advisable to reduce as much as possible the inhomogeneous broadening of the free exciton in the GaN active layer, which is why the structures presented in the following sections were grown directly on a Si (111) substrate, without any buffer layers in between.

5.2. The DBR (sample 703)

In order to check the optical quality of a DBR, both PL and reflectivity must be performed. The DBR that we studied was made of 8 pairs of $Al_{0.2}Ga_{0.8}N$/AlN λ/4 layers grown on a Si (111) substrate (Fig. 5.5). Although this choice of materials for the DBR will result in a high lattice mismatch between the DBR and the substrate, as well as the DBR and the active region of the microcavity, the emission energy of the intrinsic and extrinsic recombination bands of the two materials making up the DBR must be at a much higher energy than the exciton recombination bands in the active layer. The measurement of the TI PL of this sample did not reveal any type of extrinsic recombination bands in the spectral region corresponding to the emission of the *A* exciton of GaN that would have otherwise rendered difficult the study of the coupling between the exciton and photon modes.

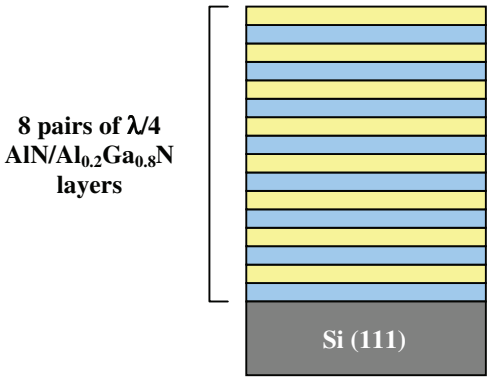

Figure 5.5. Schematic of a bottom DBR grown directly on silicon (Sample 703).

As discussed in section §2.3, one of the most important parameters of a DBR is its stop band, which must exhibit a high reflectivity over a large energy interval in order to provide a good photon confinement and to allow the probing of the polariton dispersion curves through angle resolved PL measurements. The reflectivity spectrum of the DBR at

room temperature is presented in Fig. 5.6. As expected, the reflectivity spectrum of the DBR was found to be independent of the sample temperature.

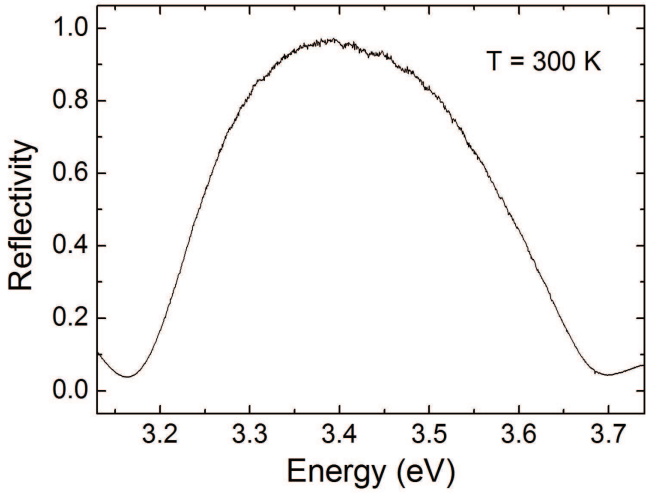

Figure 5.6. Room temperature reflectivity spectrum of a DBR made out of 8 pairs of $Al_{0.2}Ga_{0.8}N$/AlN λ/4 layers grown on Si (111).

Several differences can be noted between the experimental reflectivity spectrum of Fig. 5.6 and the simulated reflectivity spectrum presented in Fig. 2.6 for the same structure. First, for sample 703, the stop band is centered at an energy of ~3.4 eV, which is smaller than the expected energy position of the *A* exciton recombination band in the 10 K - 300 K temperature range (~3.45 ÷ 3.5 eV). This is most likely caused by the fact that the thickness of the λ/4 layers that make up the DBR was higher than the projected thickness, which resulted in a shift of the entire stop band towards lower energy values.

Second, the value of the stop band for this DBR (*i. e.* the spectral region in which the reflectivity $R > 0.9$) was found to be ~150 meV (±10 meV), which is only half of that theoretically predicted in section §2.3 (see Fig. 2.6). In fact, without the use of buffer layers to relax the high tensile strain between the DBR and the substrate, a high number of cracks, through which the strain is relaxed, were found to form during the growth process, as illustrated in Fig. 5.7, with an estimated crack density of ~5×10^2 cracks/mm^2.

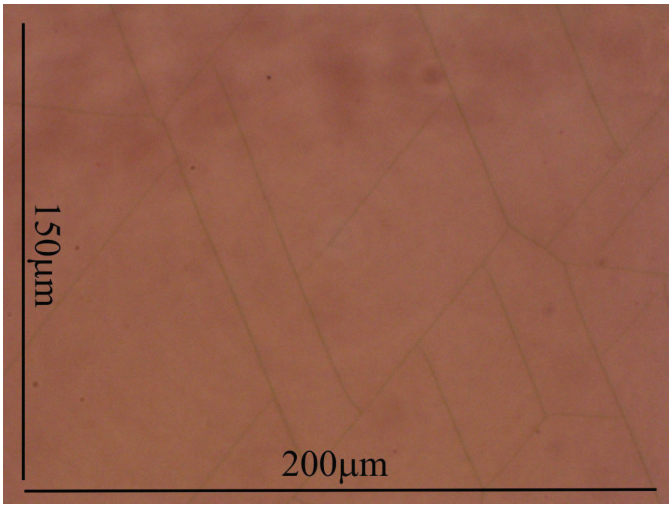

Figure 5.7. Image of the surface of the DBR (sample 703) acquired using an optical microscope.

Although a relaxation of the strain present in the sample is expected due to the formation of such cracks that propagate in the growth direction, these defects act as scattering centers for photons, thus lowering the optical quality of the DBR. The high density of these structural defects explains the strong reduction of the DBR's stop band from the theoretically predicted value of 330 meV to the ~150 meV (±10 meV) measured experimentally.

Therefore, it becomes obvious that an increase of the number of pairs of layers making up the bottom DBR is necessary in order to achieve a broader stop band. Moreover, a finer tuning of the growth parameters must be made in order to reduce the number of cracks which broaden the spectral width of the cavity mode and lower the quality factor of the resonator.

5.3. The half cavity (sample 808hc)

Following the results presented in the previous section, the half cavity was made out of a λ/2 layer of bulk GaN (~64 nm thickness) grown on 10 pairs of AlN/$Al_{0.2}Ga_{0.8}N$ λ/4 layers deposited on a Si (111) substrate (Fig. 5.8). The rotation of the sample was stopped during the deposition of the GaN active layer to allow the formation of a thickness gradient. After the completion of the full microcavity structure, this would allow achieving different detunings between the cavity mode and the exciton mode simply by changing the position of the excitation spot on the sample.

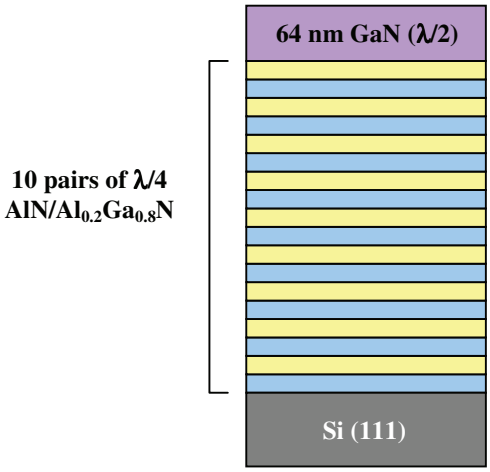

Figure 5.8. Sample 808hc: 64 nm GaN λ/2 + 10 pairs $AlN/Al_{0.2}Ga_{0.8}N$ λ/4 + Si (111).

The optimization of the growth parameters allowed the growth of a sample with fewer structural defects than sample 703, resulting in the reduction of the density of cracks from ~5×10^2 cracks/mm^2 (sample 703) to ~60 cracks/mm^2 (sample 808hc). An image of the surface of the half cavity is presented in Fig. 5.9.

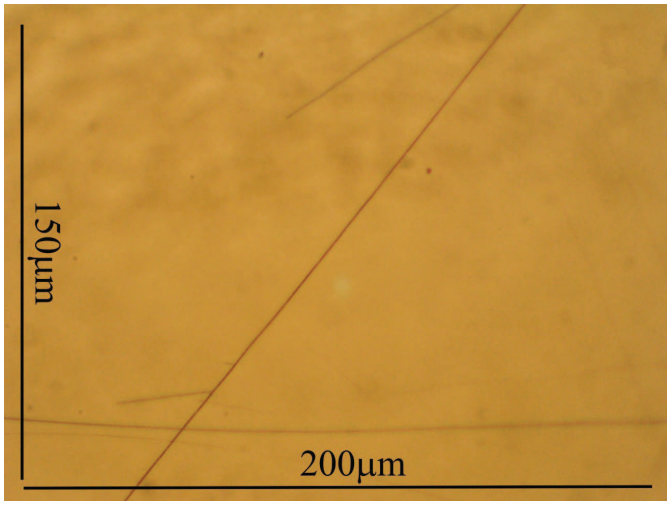

Figure 5.9. Image of the surface of the half cavity (sample 808) acquired using an optical microscope.

In Fig. 5.10 we show the TI PL (semi-logarithmic scale) and reflectivity spectra at T = 10 K taken simultaneously using the first setup described in section §4.3. The different spectra were obtained by scanning the excitation spot across the sample.

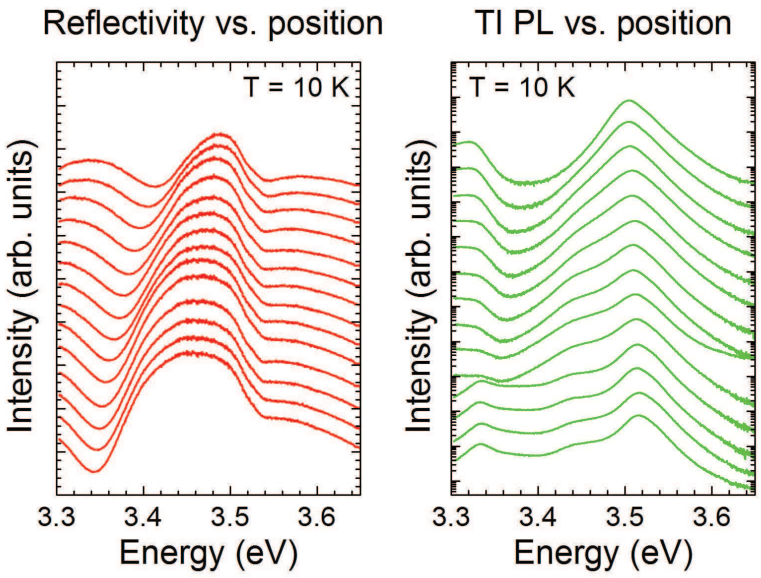

Figure 5.10. Simultaneous reflectivity (left) and TI PL (right) spectra at T = 10 K of the λ/2 GaN half-cavity (sample 808hc) as a function of excitation position. Spectra are shifted in intensity for clarity.

The exciton recombination band in the PL spectra is centered at approximately 3.5 eV, which indicates that the λ/2 active layer is subject to a higher tensile strain than all the GaN epilayers discussed in section §5.1. Moreover, the broadening of the exciton emission band at T = 10 K was found to be on the order of ~35 meV (±0.3 meV) (Fig. 5.12), a value much larger than those found for the epilayers (see Table 5.1). Since the contribution of the thermal (homogeneous) broadening of the exciton at this temperature can be considered negligible, we conclude that the exciton line shape is dominated by very strong inhomogeneous broadening mechanisms. Without the use of buffer layers or lattice matched λ/4 layers in the DBRs, the strain gives rise to numerous threading dislocations causing strong variations of the active region's energy gap resulting in a high inhomogeneous broadening of the emission.

The shape of the stop band of the half cavity's bottom DBR can be partially observed in the reflectivity spectra up to around ~3.5 eV, as a result of the lack of absorption of photons for energies below the band gap of GaN. For energies above the band gap however the light coming from the excitation source is subject to a strong absorption in the λ/2 active layer and the interaction with the bottom DBR is reduced. We also notice an energy shift of the stop band in reflectivity, which is most likely caused by the unintentional creation of a thickness gradient during the growth of the λ/4 layers.

In Fig. 5.11 we present in semi-logarithmic scale the exciton decay profile (red line) extracted from the TR PL measurement of the half cavity at low temperature (T = 10 K). The

non-resonant excitation of the sample was carried out using the 3rd harmonic of the Ti:sapphire laser. While clearly longer than the temporal profile of the laser pulse (black line), the exciton emission lifetime is still short. A value of only ~3 ps (±0.3 ps) was extracted for the lifetime of the exciton in the active layer of the half cavity from the decay profile presented in Fig. 5.11 using a fitting with an exponential decay function. Once again, this value is much smaller than those extracted for the GaN epilayers (see Table 5.1), indicating a major role of non-radiative channels in the recombination kinetics. In fact, a high concentration of impurities is expected in this sample due to the high mobility of silicon atoms at the growth temperature. The combined effect of a high density of structural defects and a high concentration of impurities explains the large inhomogeneous broadening and the very short lifetime of the exciton emission.

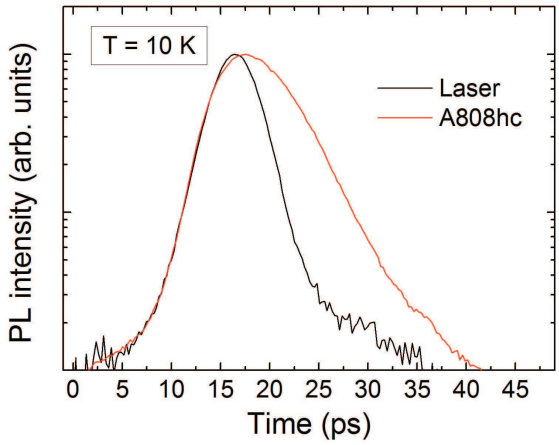

Figure 5.11. Semi-logarithmic representation of the decay profile of sample 808hc (red line) at T = 10 K. The temporal profile of the laser pulse is also reported for comparison (black line). Intensities are normalized.

The emission energy of the exciton peak undergoes a red-shift of ~45 meV in the PL spectra with increasing the sample temperature from 10 K to room temperature (see Fig. 5.12). More importantly, the total broadening of the exciton recombination band increases from 35 meV to 50 meV, while the line shape becomes asymmetrical at room temperature due to the contribution of band-to-band recombinations. Such a large value for the broadening of the emission, which is comparable to the Rabi splitting theoretically estimated in section §2.4 for a complete λ/2 GaN based microcavity, raises concerns about the possibility of achieving strong coupling at room temperature in the complete microcavity structure.

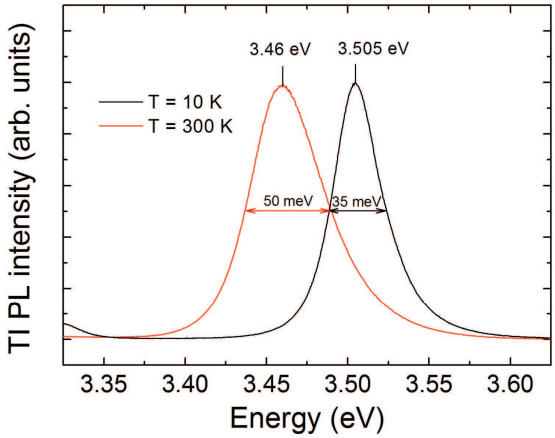

Figure 5.12. TI PL of the λ/2 GaN half-cavity at T = 10 K (black line) and T = 300 K (red line), respectively. Spectra are normalized in intensity.

5.4. The weak coupling

In a first attempt to create a microcavity in the strong coupling regime, a 20 nm Al layer was deposited on the half cavity described in the previous section, resulting in the structure shown in Fig. 5.13 (sample 808Al). The use of a metallic mirror to confine light makes it difficult to model this structure using the transfer matrix formalism described in section §2.2, which is adapted for the propagation of light through dielectric media.

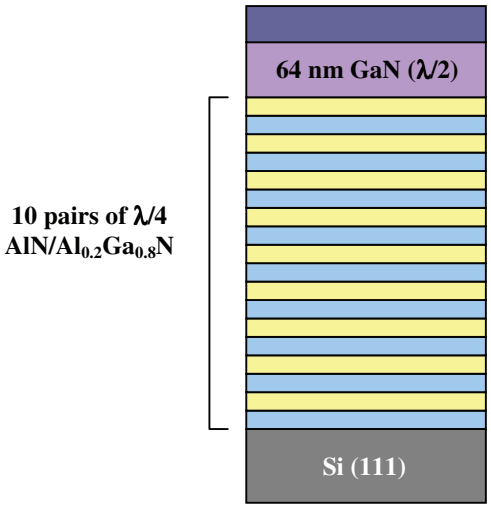

Figure 5.13. Sample 808Al: 20 nm Al + 64 nm GaN λ/2 + 10 pairs $AlN/Al_{0.2}Ga_{0.8}N$ λ/4 + Si (111).

The usage of a metallic top mirror instead of a heteroepitaxial DBR in order to provide a minimum confinement for the light in the active region was motivated by the poor crystalline quality of the underlying half cavity. A top heteroepitaxial dielectric mirror similar

to the bottom DBR did not seem to be a good choice as it would have been subject to an even higher number of structural defects, and hence a very poor optical performance was expected for the full heteroepitaxial microcavity. In fact, such a sample was later grown and its optical quality was indeed much lower than that of sample 808Al, hence we chose not present it in this work.

In Fig. 5.14 we show the TI PL (semi-logarithmic scale) and reflectivity spectra at T = 10 K taken simultaneously in different points along the thickness gradient of the GaN active layer.

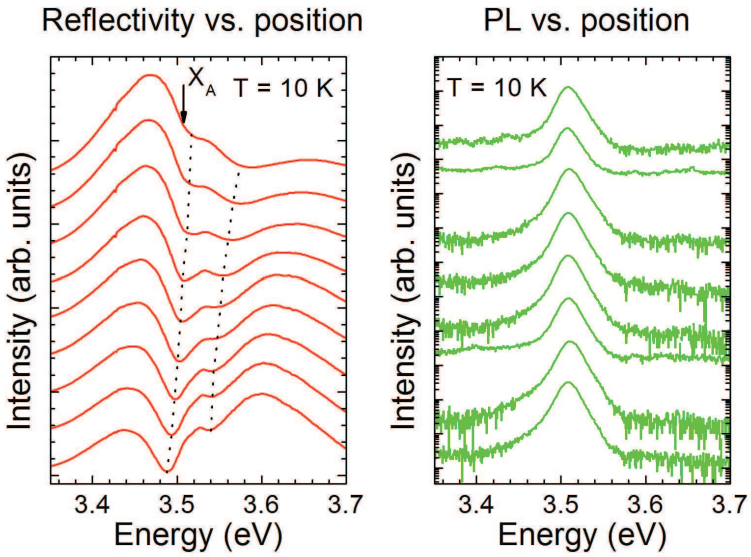

Figure 5.14. Simultaneous reflectivity (left) and TI PL (right) spectra at T = 10 K of sample 808Al as a function of excitation position. Spectra are shifted in intensity for clarity. The dotted lines in the reflectivity spectra are guides to the eye.

The dotted lines in the reflectivity spectra follow the energy positions of two modes that appear to anticross. In fact, the existence of a thickness gradient in the GaN active layer results in a continuous variation of the energy at which the cavity mode is resonant. Hence, by moving the excitation spot along the sample different energy detunings between the cavity mode and the exciton mode are probed. In this respect, the anticrossing of the two features visible in the reflectivity spectra of Fig. 5.14 can be interpreted as a coupling between the two modes. However, the anticrossing behaviour is not visible in the PL spectra, which only exhibit the emission of the bare *A* exciton mode (X_A) at approximately the same energy as that measured for the half cavity discussed in the previous section (~3.51 eV at T = 10 K).

Following the discussion presented in section §4.1, the absence of an anticrossing in the PL spectra rules out the existence of a strong coupling regime. The appearance of an

anticrossing between the photon and exciton modes in reflectivity suggests the presence of a weak coupling, likely due to the reduced *Q* factor of our structure. In fact, the reflectivity of the Al mirror was found to be around ~0.75 (±0.05), a value much lower than those needed for the achievement of a satisfactory quality factor in excess of 100 (see section §2.3). The usage of a metallic mirror instead of a dielectric one also causes a cancellation of the constructive interference mechanism, which is one of the main reasons behind using DBRs to confine light in the cavity region. Hence, a strong coupling between the exciton and photon modes is unlikely to occur in the absence of an amplification of the electric field in the cavity region; therefore, only a weak coupling between the two modes is evidenced in reflectivity.

An additional effect that contributes to the polaritonic features in the PL spectra is the strong localization of the exciton. In fact, the emission energy of 3.508 eV (±1 meV) of the uncoupled *A* exciton (X_A), indicated by an arrow in the reflectivity spectra, is below the energy of both modes seen in reflectivity for several positions on the sample. Since reflectivity measurements can only evidence transitions associated to the absorption of light by free oscillators (see section §4.1), we conclude that the anticrossing pattern observed in the reflectivity spectra of Fig. 5.14 reveals only a weak coupling regime between the cavity mode and the free *A* exciton.

The anticrossing behaviour in the reflectivity spectra is visible up to room temperature, as shown in Fig. 5.15. The reduced number of spectra shown in Fig. 5.15, with respect to Fig. 5.14, is due to the shift of the PL emission towards a lower energy of 3.457 eV (±1 meV) with increasing temperature to 300 K. Hence, the data collected on points with a very positive detuning between the uncoupled cavity and exciton modes was omitted from the representation. At room temperature, the weakly coupled features in the reflectivity spectra appear more washed out. While the quality factor of the cavity is not expected to decrease with increasing temperature, the increased thermal broadening of the exciton mode gives rise to less pronounced features in reflectivity. Still, it is interesting to note that the weak coupling persists up to 300 K.

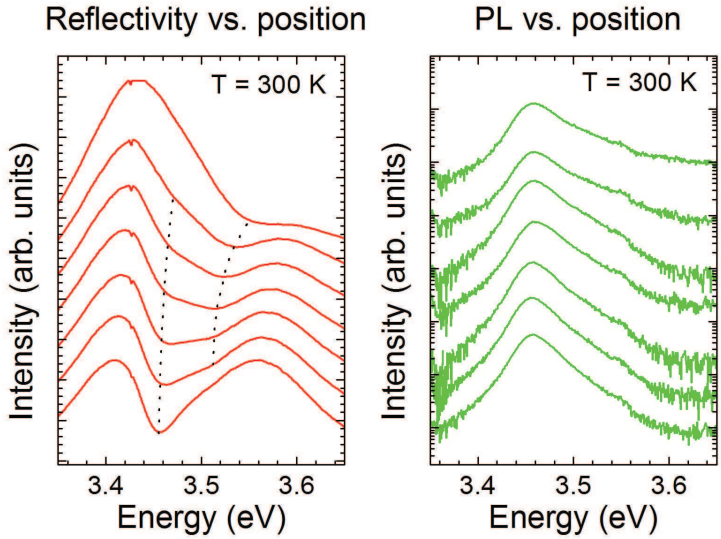

Figure 5.15. Simultaneous reflectivity (left) and TI PL (right) spectra at T = 300 K of sample 808Al as a function of excitation position. Spectra are shifted in intensity for clarity. The dotted lines in the reflectivity spectra are guides to the eye.

As expected, the line shape of the TI PL emission in Fig. 5.15 (right) presents a strong asymmetry at room temperature due to the contribution of band-to-band recombinations. We notice however a change in the shape of the thermal tail with changing detuning, which is most likely due to a filtering effect of the cavity mode.

Even for a weakly coupled system, a narrowing of the spectral width of the emission is still expected with respect to the free space emission of the half-cavity [30] [95] [96]. While the FWHM of the PL line shape increases from 23 meV at T = 10 K to 40 meV at T = 300 K (see Fig. 5.16), both of these values are smaller than those measured for the half cavity (35 meV at 10 K and 50 meV at 300 K, respectively).

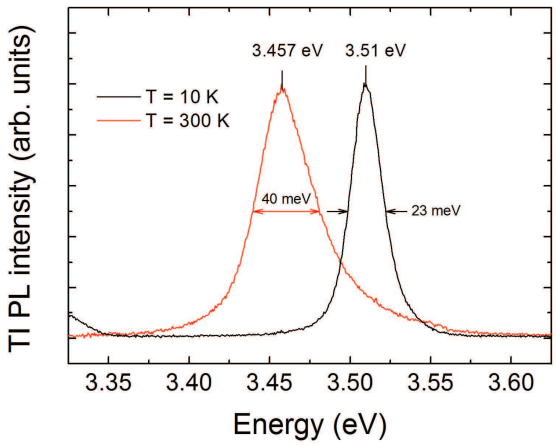

Figure 5.16. TI PL of sample 808Al at T = 10 K (black line) and T = 300 K (red line), respectively. Spectra are normalized in intensity.

The spectral narrowing of the excitonic emission demonstrates the existence of a weak coupling between the exciton and photon modes. The strong coupling of the modes is not observed, most likely due to the very small quality factor of the microcavity, which is estimated to be approximately $Q \approx 35$ from eq. (22), with the reflectivities of the two mirrors taken as $R_{DBR} \approx 0.95$ and $R_{Al} \approx 0.75$, respectively. At this point it became obvious that the reflectivity of the top mirror needed to be improved in order increase the quality factor of the microcavity to values that would allow the observation of strong coupling.

5.5. The strong coupling

As mentioned at the beginning of the previous section, in order to create a top DBR with a satisfactory reflectivity and stop band, the growth of a fully epitaxial microcavity was also attempted by growing 7 pairs of AlN/$Al_{0.2}Ga_{0.8}N$ λ/4 layers on top of the half cavity described in section §5.3. The optical quality of the resulting structure was found to be inferior to that of sample 808Al, and hence a different approach had to be used to complete the microcavity.

The solution lied in using not an epitaxially grown DBR, but one simply made of amorphous dielectric Si_3N_4/SiO_2 λ/4 layers. There are considerable advantages in using amorphous dielectric layers instead of epitaxially grown layers. Firstly, in the case of an epitaxially grown top DBR, the structural defects (cracks, dislocations etc.) present in the underlying structure will not only propagate in the growth direction, but they will also multiply, causing a reduction in the optical quality of each successive λ/4 layer. However, this is not the case for an amorphous dielectric material, as it will not obey the crystalline symmetry of the underlying layer, nor it will be subject to strain effects and structural defects. Secondly, the growth of high quality Si_3N_4 and SiO_2 λ/4 layers is very well mastered and can be easily achieved by metalorganic vapour phase epitaxy (MOVPE), which is a well-established production technology [97]. Finally, the increased refractive index contrast between Si_3N_4 and SiO_2 ($n_{Si_3N_4} / n_{SiO_2} = 1.341$), compared to that of AlN and $Al_{0.2}Ga_{0.8}N$ ($n_{Al_{0.2}Ga_{0.8}N} / n_{AlN} = 1.164$, see section §2.3), results in the achievement of a higher reflectivity and a larger stop band for a Si_3N_4/SiO_2 DBR made of fewer pairs of λ/4 layers than a

AlN/$Al_{0.2}Ga_{0.8}N$ DBR. (The refractive indexes $n_{Si_3N_4} = 2.099$ and $n_{SiO_2} = 1.565$ at 355 nm were extracted from ref. [98].)

Hence, the bulk λ/2 GaN microcavity was completed with the deposition of 8 pairs of Si_3N_4/SiO_2 λ/4 layers on top of the half cavity described in section §5.3 (Fig. 5.17). The structure illustrated in Fig. 5.17 (sample 808) is also known as a *hybrid microcavity* due to the use of both heteroepitaxial and amorphous dielectric materials in its structure.

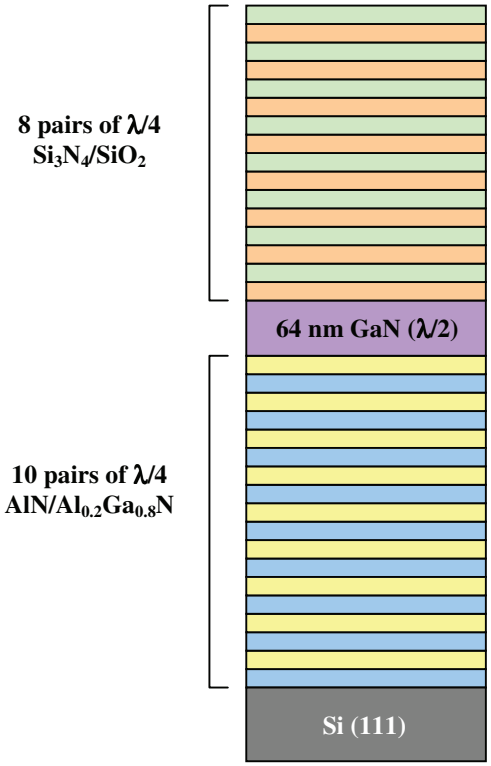

Figure 5.17. Sample 808: 8 pairs of Si_3N_4/SiO_2 λ/4 + 64 nm GaN λ/2 + 10 pairs of AlN/$Al_{0.2}Ga_{0.8}N$ λ/4 + Si (111).

The simultaneous reflectivity and TI PL (semi-logarithmic scale) spectra obtained by scanning the excitation spot along the thickness gradient of the GaN active layer are presented in Fig. 5.18 for a temperature of 10 K. The observation of an anticrossing between the two spectral features in both reflectivity and PL, assigned to the upper and lower polariton, respectively, demonstrates the presence of a strong coupling in the hybrid microcavity at low temperature. The population of the upper polariton, evidenced in the PL spectra, is quite small at T = 10 K. In fact, since the upper polariton is mainly populated through the interaction between acoustic phonons and polaritons in the thermal region of the lower branch (see section §4.2, Fig. 4.4), this is an inefficient process at low temperature, explaining the low upper polariton population for very positive detunings where UP has a high photonic fraction.

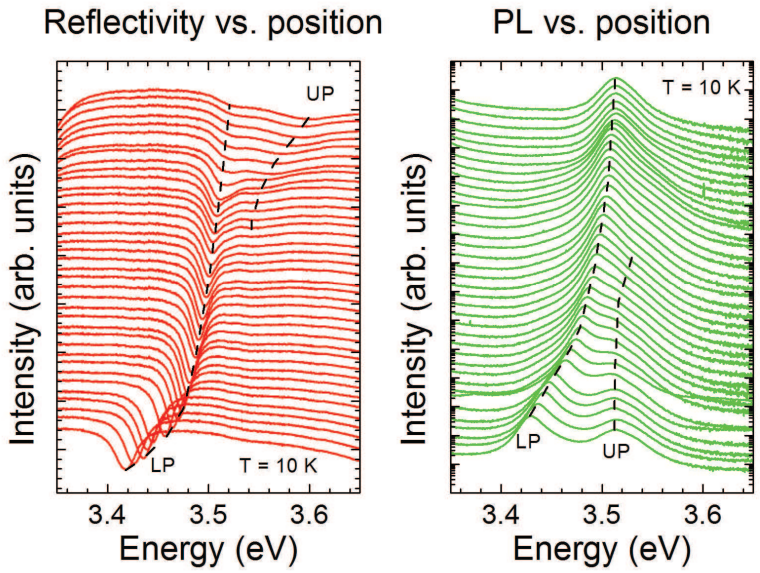

Figure 5.18. Simultaneous reflectivity (left) and TI PL (right) spectra at T = 10 K of the hybrid microcavity (sample 808) as a function of excitation position. Spectra are shifted in intensity for clarity. The dashed lines are guides to the eye.

The quality factor of the microcavity, extracted as the ratio between the cavity polariton energy and its FWHM at very negative detuning, is estimated to be:

$$Q_{808} = \frac{3.43\,\text{eV}}{22\,\text{meV}} \cong 156 \tag{68}$$

A Rabi energy splitting of 30 meV (±1 meV) is extracted for the two polariton modes from the PL spectra, suggesting that the strong coupling should occur even at room temperature. As we have seen in the previous sections, increasing the temperature of the structure from 10 K to 300 K will result in a significant red shift (~45 meV) of the excitonic transitions energy, a value which is larger than the Rabi splitting. As a result, the temperature can be used as an effective way to tune the polariton modes. This method of tuning the polariton branches in the strong coupling regime has been demonstrated previously in GaAs based systems [99] - [101]. Fig. 5.19 shows the temperature-dependent reflectivity and photoluminescence (semi-logarithmic scale) measured in the same point on the sample in the temperature range between 10 K and 300 K.

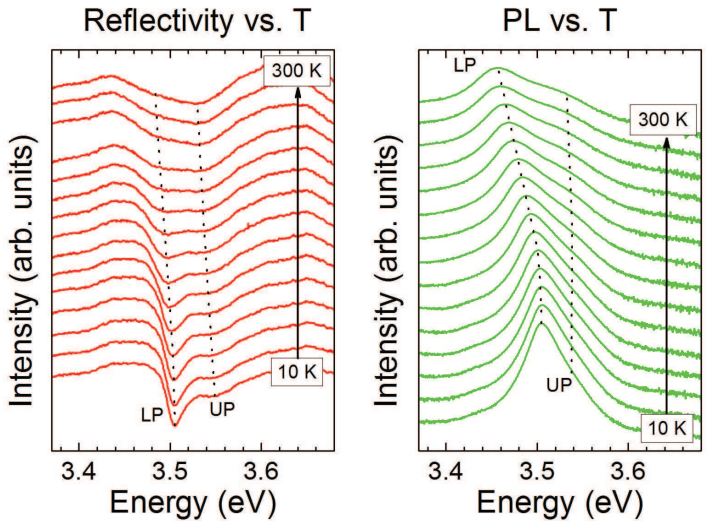

Figure 5.19. Simultaneous reflectivity (left) and TI PL (right) spectra in the same point of the hybrid microcavity (sample 808) as a function of temperature. Spectra are shifted in intensity for clarity. The dotted lines are guides to the eye.

The observation of the upper and lower polariton features up to room temperature in both TI PL and reflectivity demonstrates the existence of a strong coupling regime even at temperatures comparable to the Rabi splitting between the two modes. Moreover, the UP can be observed at 300 K in photoluminescence for very positive detunings, likely due to a stronger interaction of acoustic phonons with polaritons in the thermal region of the lower polariton. The presence of the strong coupling at room temperature, as well as the more efficient population of the upper polariton are clearly demonstrated by the anticrossing patters illustrated in Fig. 5.20.

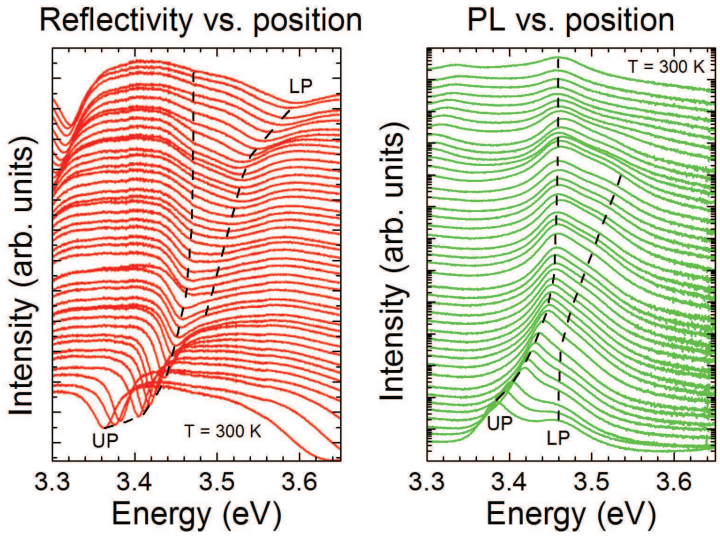

Figure 5.20. Simultaneous reflectivity (left) and TI PL (right) spectra at T = 300 K of the hybrid microcavity (sample 808) as a function of excitation position. Spectra are shifted in intensity for clarity. The dashed lines are guides to the eye.

As a result of the strong coupling, the broadening of the emission from the lower polariton is expected to change with detuning due to a variation of its respective excitonic and photonic fractions (see eq. (65)). Indeed, a significant narrowing of the LP PL is observed for very negative detuning, where the LP has a high photon fraction, whereas for very positive detuning, having a high excitonic fraction, the broadening of the LP recombination band is identical with the one measured for the bare exciton emission of the half cavity at room temperature (Fig. 5.21).

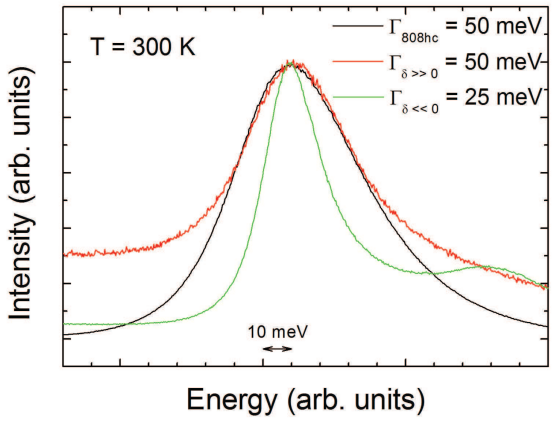

Figure 5.21. Room temperature TI PL of the bare exciton of the half cavity (black line), LP PL at very positive detuning (red line), and LP PL at very negative detuning (green line). Energy scales are shifted for clarity. Intensities are normalized.

Further modifications are expected in the recombination kinetics. The emission lifetime of the polariton must be modified with respect to the bare exciton in the half cavity, as a consequence of the strong electromagnetic coupling that is established between excitons and photons. The photon lifetime simply reflects the escape from the optical resonator and it is usually much shorter than the exciton lifetime. In the case of our present structure, which exhibits a *Q* factor of ~150, the cavity photon lifetime is estimated to be ~0.05 ps. Therefore an increase of the PL lifetime is expected when increasing the cavity detuning from negative to positive values. The experimental decay curves for the lower polariton at three different detunings (red, green, blue) are reported in Fig 5.22 in semi-logarithmic scale and compared with the instrumental resolution (black) and the lifetime of the PL band (cyan) of the active GaN λ/2 layer prior to the deposition of the upper dielectric DBR, for a temperature of 10 K. The emission lifetimes are very short, but the increase of the lower polariton lifetime with its increasing excitonic fraction is clearly observed. As in the case of emission broadening, for a very positive detuning the decay time of the LP coincides with that of the half cavity's bare

exciton. We note that the 2 ps temporal resolution of our streak camera is almost two orders of magnitude longer than the estimated lifetime of the cavity photon; hence we cannot gain access to the real decay profile of the lower polariton when it has a considerable photon fraction, as the measured decay profile is dominated by the time resonse of our acquisition system.

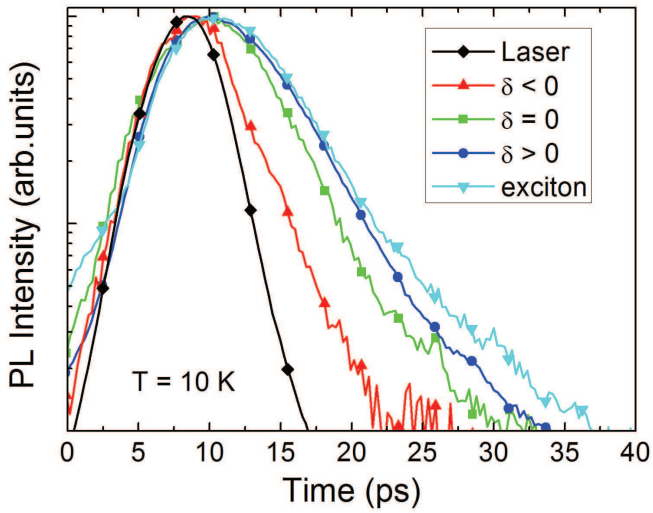

Figure 5.22. Semi-logarithmic representation of the decay profiles of the hybrid microcavity (sample 808) at T = 10 K for negative (red line), zero (green line), and positive detuning (blue line), respectively. The temporal profile of the laser pulse (black line) and the decay profile of the bare exciton of sample 808hc (cyan line) are also reported for comparison. Intensities are normalized.

5.5.1. Thermalization issues

As we have seen, the population of the upper polariton through acoustic phonons interaction is found to be more efficient with increasing temperature. However, the very short lifetime of the lower polariton raised questions about the state of thermalization of the two polariton branches, which is a relevant issue in microcavity physics and applications [30]. This fact encouraged us to study the aspect of thermalization between the upper and lower polariton branches at 300 K, which is the temperature of interest for practical applications. In order to exploit this point, we first used the transfer matrix formalism described in chapter §2 to calculate the reflectivity, absorption, and transmission coefficients of our structure corresponding to the anti-crossing position on the sample at room temperature. Parameters used were a longitudinal transverse splitting ω_{LT} = 1 meV, exciton inhomogeneous

broadening Γ_{inh} = 25 meV and exciton homogeneous broadening at room temperature Γ_{hom} = 30 meV; the values for the two broadenings are extracted from the PL of the half cavity (sample 808hc) and the highest quality epilayer (N191), respectively. Experimental and simulated reflectivities are found to be in good agreement (Fig. 5.23 (a)), considering that neither the *B* or *C* excitons, nor interband transitions were considered in our model. The deduced absorption spectra calculated as A = 1 - R - T is depicted in Fig. 5.23 (b) and compared with A' = 1 - R, which is an experimentally accessible data; here T and R are the transmitted and reflected power densities normalized to the incident power density. Although quantitatively there is a factor of ~25% between A' and A, both spectra are quite similar in terms of shape. Thus, from a qualitative point of view, the contribution given by the transmission can be neglected. This is also sustained by the fact that absorption will suffer a large rescaling when fitted over data inferred from experimented PL. These considerations allow us to extract absorption directly from the experimental reflectivity as A = 1 - R, without having to go through a fitting procedure.

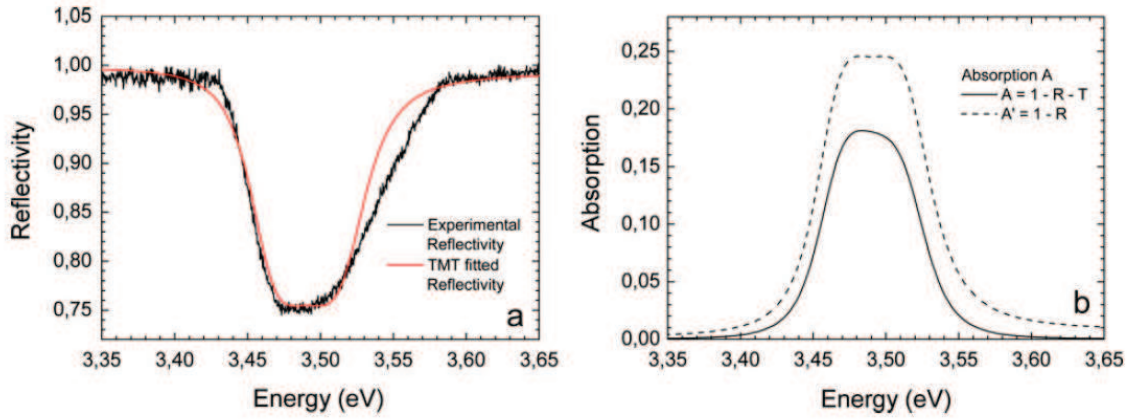

Figure 5.23. (a) Reflectivity spectra corresponding to the anti-crossing position in detuning (black line) for T =300 K fitted with a transfer matrix simulation (red line). **(b)** Absorption spectra corresponding to the anti-crossing position in detuning, obtained with and without the contribution of transmission.

In order to determine the extent to which one can say that polariton populations of the two branches are thermalized, absorption obtained as A = 1 - R was multiplied by a Boltzmann filling factor corresponding to a temperature of 300K and compared with experimental PL, as seen in Fig. 5.24 (a). Fig. 5.24 (b) follows the reverse procedure, *i. e.* experimental absorption is fitted with experimental PL divided by the same Boltzmann filling factor. The strong signal fluctuations visible in Fig. 5.24 (a) at low energies are due to the multiplication of the experimental absorption with an exponentially increasing filling factor, resulting in the strong amplification of its background noise. Differences between the two

spectra are small and we find a good agreement between absorption calculated by either reflectivity or PL (up to a Boltzmann filling factor), given the roughness of our assumptions. No adjustable parameters were used in the comparison.

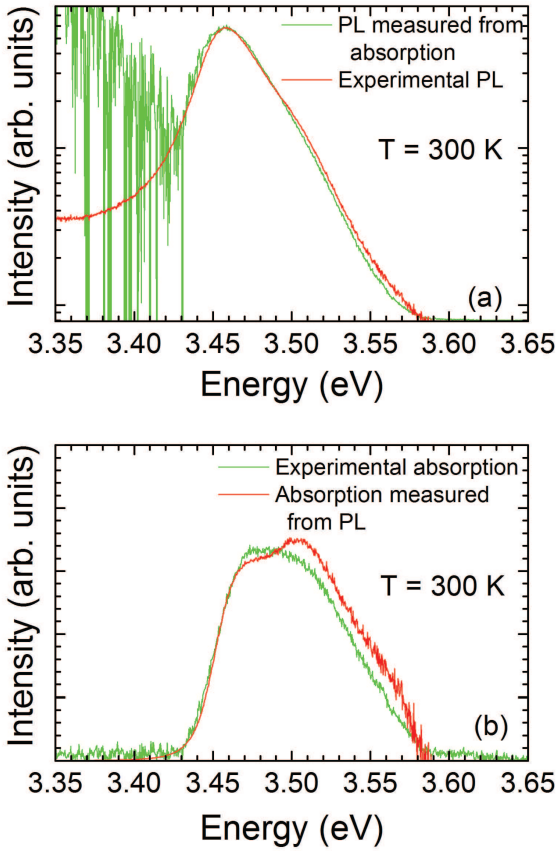

Figure 5.24. (a) Absorption multiplied by a Boltzmann filling factor (green line) compared with experimental PL (red line). **(b)** Experimental absorption (green line) compared with PL divided by the same Boltzmann factor (red line). Intensities are normalized.

Hence, the room temperature polariton emission of the hybrid microcavity (sample 808) reveals thermalized populations between the two polariton branches, despite the very short lifetimes (see Fig. 5.22). This denotes very efficient energy relaxation processes in the LP, as well as an efficient population of the UP states through acoustic phonon interactions in our bulk GaN microcavity, an aspect which is in sharp contrast with the findings on GaAs based microcavities where a strong polariton bottleneck was found to inhibit polariton relaxation [17] [18].

5.5.2. Suppression of the relaxation bottleneck

As already mentioned in the introduction, in the case of non-resonant optical excitation of GaAs QW microcavities, acoustic phonon scattering rates from the thermal region into the strong coupling region are found to be small due to the large energy transfer required compared to the typical acoustic phonon energies of 1 meV. Furthermore, the strongly coupled states have very short radiative lifetime (~1 ps) due to their high photon fraction, thus leading to a non-thermal polariton population and the occurrence of a relaxation bottleneck [17] [18]. Trying to overcome this bottleneck by increasing excitation densities in order to stimulate exciton - exciton scattering resulted in the collapse of strong coupling, and the achievement of conventional photon lasing (VCSEL) [19] [20]. On the other hand, due to the small exciton binding energy and Rabi splitting (~5 meV), it was not possible to increase the sample temperature in order to stimulate a more efficient relaxation of polaritons through acoustic phonon interactions, as this would have resulted in the ionization of excitons and the destruction of the strong coupling regime. Thus, it becomes obvious that the existence of a polariton relaxation bottleneck in a semiconductor microcavity can have important consequences on its performances, which motivated us to study this phenomenon in our hybrid bulk GaN microcavity.

In GaAs based microcavities, the relaxation bottleneck manifests itself as a strong increase of the LP PL intensity at emission angles corresponding to the anticrossing between the two polariton branches (*i. e.* resonance of the uncoupled exciton and photon modes) at low temperature and low excitation power density [18]. In order to check for the existence of a relaxation bottleneck in our GaN microcavity (sample 808), we performed angle resolved PL measurements (using the setup described in section §4.3) at various temperatures and different detunings, which allows us to determine the occupancy of the polariton branches. We chose to work at three negative detunings δ between the uncoupled photon and exciton modes at $k = 0$, in order to be able to observe the anticrossing of the polariton dispersion curves at resonance. The typical anticrossing behaviour of the lower and upper polariton modes in PL (semi-logarithmic scale) is illustrated in Figs. 5.25 (a) - (c), corresponding to the three negative detunings considered, with approximate values of: (a) δ = -10 meV, (b) δ = -40 meV, and (c) δ = -80 meV, respectively. While the anticrossings of the two features are observed even for low temperatures, we chose to present the angle resolved PL spectra for higher temperatures due to the increased visibility of the upper polariton. As discussed previously, the energy

positions of the upper and lower polariton emissions in the angle resolved spectra allow the extraction of the polariton dispersion curves as a function of the external emission angle θ.

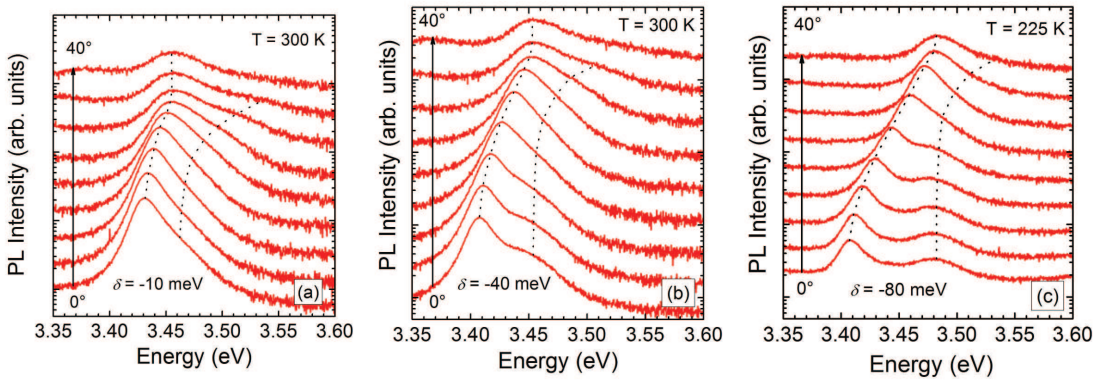

Figure 5.25. Angle resolved PL spectra of sample 808 (in semi-logarithmic scale) for emission angles from 0° to 40° corresponding to: **(a)** δ = -10 meV, T = 300 K; **(b)** δ = -40 meV, T = 300 K; **(c)** δ = -80 meV, T = 225 K. The spectra are shifted in intensity for clarity. The dotted lines are guides to the eye, indicating the positions of the LP and UP emissions.

Fig. 5.26 depicts the intensity variation of the LP mode with the external angle of detection θ at different temperatures for an incident power density of 10 W/cm^2.

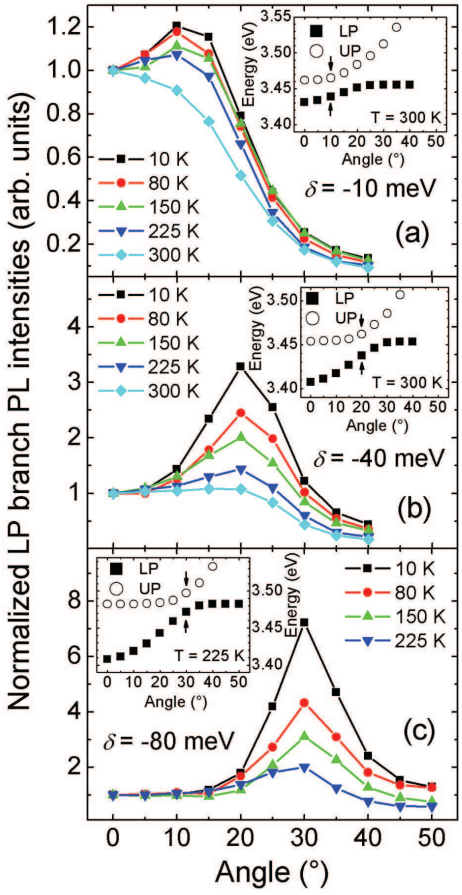

Figure 5.26. Experimental LP PL intensities as a function of the external detection angle at different temperatures for a given initial detuning δ of **(a)** δ = -10 meV, **(b)** δ = -40 meV, **(c)** δ = -80 meV, respectively. The insets represent the LP and UP dispersion curves at 300 K for **(a)** and **(b)**, and at 225 K for **(c)**. The intensities are normalized to unity for 0° detection angle.

The same three detunings between the uncoupled photon and exciton modes at $k = 0$ were considered, with approximate values of: (a) -10 meV, (b) -40 meV, and (c) -80 meV. Peak intensities were normalized to unity for 0°, and the $1/\cos(\theta)$ correction was also considered. In order to keep the initial detuning constant at all temperatures, the position on the sample was adjusted accordingly, taking advantage of the wedged profile of our microcavity. In Fig. 5.26 (c), the dependence at 300 K is not shown since a negative detuning of -80 meV could not be achieved for the sample at this temperature. The insets show the polaritonic dispersion curves, extracted from Figs. 5.25 (a) - (c), at 300 K for Figs. 5.26 (a) and (b), and at 225 K for Fig. 5.26 (c), as a function of the external emission angle for the three initial detunings. The energy positions of the two polaritonic features are reported within an error of ±0.3 meV. The arrows indicate the angles at which the two modes anticross.

At low temperatures, a maximum of the LP intensity versus angle is observed in Figs. 5.26 (a) - (c) at 10°, 20° and 30°, respectively. The enhancement of the emission corresponds to the angles at which the two branches anticross and, according to our previous discussion, can be considered an experimental demonstration [18] of the presence of a relaxation bottleneck, *i. e.* the inefficient scattering of high k polaritons into lower k states. Although a suppression of the relaxation bottleneck has been achieved in GaAs and II-VI MCs for high excitation densities through exciton - exciton scattering mechanisms [17, 24], these systems offer little insight onto the possibility of studying a phonon mediated bottleneck suppression due to the loss of strong coupling at non-cryogenic temperatures. Since in GaN MCs the strong coupling is observed up to room temperature, this allows us to study relaxation mechanisms through exciton - phonon interaction. In Figs. 5.26 (a) - (c), for all detunings, we observe a reduction in the emission enhancement at resonance with increasing temperature. We also notice that the reduction is more significant for a large initial detuning (Fig. 5.26 (c)), where the LP dispersion curve is much steeper around the anticrossing position and hence a stronger bottleneck effect is expected to be present, and less significant for a small initial detuning (Fig. 5.26 (a)) that gives rise to a less steep dispersion curve. In all cases, near room temperature (Fig. 5.26 (c)) and at room temperature (Figs. 5.26 (a) and (b)), the polariton relaxation bottleneck is almost completely washed out.

Our experimental findings are supported by theoretical results reported in Fig. 5.27, which were obtained by our colleagues from the University Blaise Pascal in Clermont Ferrand. Simulations of the LP emission as a function of angle at temperatures and detunings identical to the experimental ones were performed by solving semi-classical Boltzmann equations, using a model developed to describe the emission of bulk GaN microcavities [102]:

$$\frac{\mathrm{d}n_k}{\mathrm{d}t} = P_k - \Gamma_k n_k - n_k \sum_{k'} W_{k\to k'}(n_{k'}+1) + (n_k+1)\sum_{k'} W_{k'\to k} n_{k'} \qquad (69)$$

In this equation, n_k is the occupation number of a state with wave vector k; the P_k and $\Gamma_k n_k$ terms describe the pumping and decay of the particles. The scattering rates $W_{k\to k'}$ take into account the exciton - phonon interaction (LO phonons by Frölich interaction, acoustic phonons by deformation potential and piezoelectric interaction) and exciton - exciton interaction (in the Born approximation). Details of the simulation, the expression giving the scattering rates, and the material parameters can be found in ref. [102], and references within. The specificity of the present structure, namely the cavity photon lifetime of ~0.05 ps, the experimentally estimated non-radiative exciton lifetime of 3 ps, and the inhomogeneous broadening of the exciton line of ~25 meV, were all taken into consideration. The emission intensity was calculated by integrating the occupation coefficients over the first 50 ps after the arrival of the exciting pulse and taking into account the photonic fraction of the corresponding states.

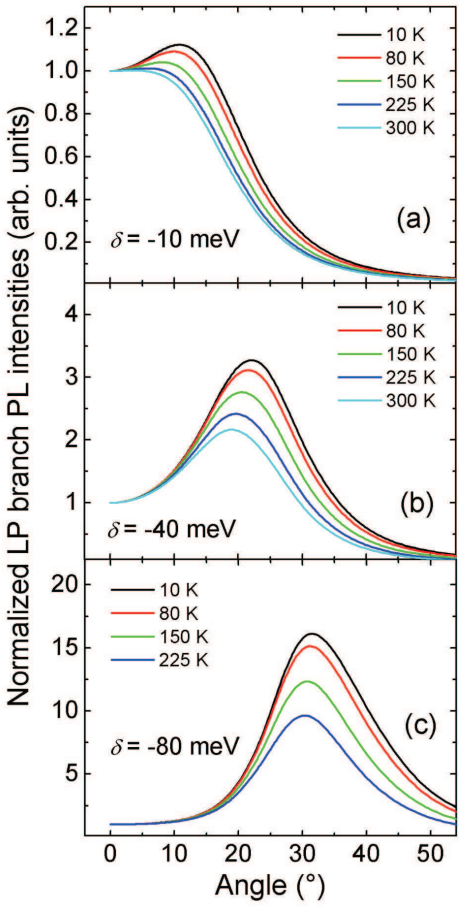

Figure 5.27. Theoretical simulations of the LP PL intensities as a function of angle. The lines are obtained as solutions of semi-classical Boltzmann equations using the initial detuning δ of the experimental data presented in Fig. 5.26: **(a)** δ = -10 meV, **(b)** δ = -40 meV, and **(c)** δ = -80 meV. The intensities are normalized to unity for 0° detection angle.

The theoretical simulations performed confirm three very important aspects of our experimental findings: (i) the enhancement of the PL emission at those angles where we observe the anticrossing of the LP and UP branches; (ii) the increase at low temperature of the ratio between the PL intensity maxima and the PL intensity at $k = 0$ as the detuning between the uncoupled photon and exciton modes becomes more negative; (iii) the suppression of the bottleneck with increasing temperature. The significant agreement between experiment and theory indicate a clear understanding of the main physical mechanisms involved. Nevertheless, we also note that the theoretical predictions show a larger ratio between the PL intensity maxima and the PL intensity at $k = 0$ with respect to the experimental findings, especially at large negative detunings. We attribute this discrepancy to disorder effects, known to play an important role in nitrides, and to an underestimation of the exciton - carrier and exciton - exciton scatterings. In fact, since GaN grown on Si (111) via AlN layers is very resistive and due to the difficulty in estimating the unintentional carrier doping in our structure, the exciton-carrier scattering was not considered in the simulation. Furthermore, the excitation power density of around 10 W/cm^2 used in our measurements cannot be considered negligible.

In order to check the role of exciton - exciton scattering, in Fig. 5.28 we show the experimental LP PL intensity dependence with angle at 80 K (Fig. 5.28 (a)) and 150 K (Fig. 5.28 (b)) for an initial detuning of -40 meV and for incident power densities ranging from 10 to 80 W/cm^2.

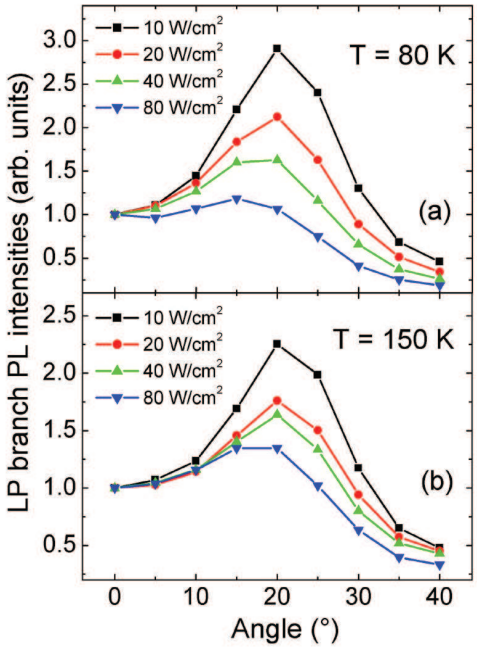

Figure 5.28. Experimental LP PL intensities as a function of external detection angle for different excitation power densities at: **(a)** 80 K and **(b)** 150 K, respectively. The detuning between the uncoupled photon and exciton modes at $k = 0$ is -40 meV. Intensities are normalized to unity for 0° detection angle.

We find a small superlinear increase of the emission at small angles with increasing excitation and a suppression of the relaxation bottleneck, likely driven by the exciton - exciton scattering processes. This suppression effect is more pronounced at 80 K than at 150 K, because the reduced weight of exciton - phonon scattering in the relaxation of lower polaritons. We conclude that even at 10 W/cm^2, the exciton - exciton relaxation mechanism may play a role in our system, thus explaining the slightly reduced bottleneck suppression in the theoretical simulations at higher temperatures when compared to the experimental data.

Therefore, we find that, despite the small density of states and a PL lifetime of only 3 ps, the thermal suppression of the LP relaxation bottleneck implies that at 300 K exciton - acoustic phonon scattering in GaN MCs is the dominant relaxation mechanism through which the lower *k* states are populated. Hence, while angle resolved measurements reveal a significant relaxation bottleneck in bulk GaN based microcavities at low temperature, the scattering of high *k* polaritons towards lower *k* states becomes more efficient with increasing temperature, and a complete suppression of the relaxation bottleneck is found at room temperature. The remarkable energy relaxation of the LP branch at 300 K within the very short polariton lifetime denotes an efficient polariton - acoustic phonon scattering. This is supported by a fully comprehensive theory based on the Boltzmann equations that reproduces qualitatively, and semi-quantitatively, the experimental data.

To conclude this section, we demonstrated the presence of a strong coupling regime in our bulk λ/2 GaN microcavity, and we found important differences in the dynamics of polaritons with respect to the GaAs counterparts in terms of thermalization of the upper and lower polariton populations, and in the possibility to achieve a suppression of the relaxation bottleneck without the destruction of the strong coupling regime.

5.6. Conclusions of the chapter

In this chapter we followed the development of bulk GaN microcavities from their basic constituents (active layer, DBR) into complete structures. We have shown how the improvement of their quality factor resulted in the transition from weak coupling to strong coupling. We examined the peculiarities of the strong coupling in our hybrid microcavity, placing a special emphasis on the 'natural' relaxation of the relaxation bottleneck at room

temperature, a clear advantage of GaN based microcavities when considering the realization of a room temperature operating polariton laser.

However, the lack of a marked superlinear increase of the emission at $k = 0$ when increasing power density above a threshold, denoting the formation of a polariton condensate similar to the one observed for II-VI MCs [24], is an indication of the strong disorder still present in GaN microstructures, mainly caused by strain related effects. Therefore, uncertainties in controlling strain effects during the growth process still limit the optical quality of GaN based microcavities, strongly affecting their polariton recombination dynamics.

While a considerable progress in the optimization of growth parameters was achieved over the course of this study, at the same time the growth of GaN QWs has also seen important improvements, especially in the control of QCSE related effects discussed in subsection §1.3.2, which led the scientific community to reconsider them for the realization of the active region of a microcavity. In fact, the increased exciton binding energy and oscillator strength with respect to bulk GaN make them the prime candidates for the realization of a room temperature operating polariton laser. The following chapter is dedicated to the study of state-of-the-art GaN/AlGaN quantum wells.

6. Optical properties of state-of-the-art GaN/AlGaN quantum wells

As discussed in section §3.2, for a number of years the achievement of GaN/AlGaN quantum wells with an optical quality comparable to that of GaN epilayers faced a lot of difficulties due to the limited *know-how* that the growers had in controlling structural defects. The large inhomogeneous broadening of the PL [31] [74], and the decrease of the exciton binding energy and oscillator strength below values measured for bulk GaN [78] needed to be addressed through sample design and optimization of growth parameters. The samples studied in this chapter were provided to us by our colleagues from EPFL, Lausanne, Switzerland.

6.1. Description of samples

In this chapter we will refer to two types of samples, which are GaN/$Al_xGa_{1-x}N$ quantum wells with small Al content in the barriers (x = 5%, and 9%, respectively). The idea behind using such a small Al concentration in the confining layers was to reduce the lattice mismatch between the barriers and the GaN well region. The minimization of such strain was a key factor in reducing the QCSE associated to the strong piezoelectric field to allow for a better control of all the unwanted effects discussed in subsection §1.3.2.

One of the main advantages in the growth of the samples was the use of the same technique utilized for the dielectric DBR (see section §5.5), which is MOVPE, a well-established production technology [97]. The samples were grown on high quality 3 μm thick GaN templates on *c*-plane sapphire substrates. Single QWs were grown on a 200 nm thick $Al_xGa_{1-x}N$ layer and then capped with a 50 nm thick $Al_xGa_{1-x}N$ layer, with x = 5% or x = 9%, respectively. A detailed description of the growth process and optimization of the interfaces is provided in Ref. [103]. We would just like to mention that the optimization of interfaces between barriers and well proved to be crucial in reducing the alloy fluctuations in the barriers, which, as we will see, resulted in a significant decrease of the inhomogeneous broadening of the emission compared to previous samples. The growth of the well region was performed to produce a thickness gradient across the sample. Well thicknesses were found to

be in the range from 3 monolayers (MLs) to 10 MLs (*i. e.* 15 ÷ 50 Å) for the two samples. As a result, the energy of the exciton recombination could be efficiently tuned on the samples.

6.2. Recombination kinetics of biexcitons

As discussed in section §1.2, the exciton is a free particle which, similar to atoms in gas phase, may interact to produce exciton molecules, *i. e.* biexcitons. A relevant requirement for the observation of the biexciton formation in a QW is the high optical quality of the structure. The in-plane structural disorder produces exciton localization (which strongly reduces the probability of biexciton formation) and it determines the inhomogeneous broadening of the exciton optical resonance (which may mask the biexciton recombination). Hence, the investigation of the biexciton recombination is a very simple and straightforward way to assess the optical quality of our QWs.

A lot of studies on biexciton properties in III-V semiconductors have been performed in GaAs based QWs [104] - [106], where the optical quality is nowadays extremely high. However, a relevant drawback of GaAs QWs is that the biexciton binding energy is in the range of 1 meV. As a consequence, the biexciton gas thermalizes with the excitons resulting in a common averaged kinetics [106]. In ionic II-VI QWs, the biexciton energy increases up to about 10 meV and stable excitons are observed. These are found to play a key role in the stimulated emission process [107]. Despite this, little work has been dedicated to the biexciton kinetics in II-VI QWs [108] [109], also because the large inhomogeneous broadening commonly observed tends to mix exciton and biexciton emissions [108]. GaN based QWs offer the advantage of an increased exciton binding energy, estimated to be larger than 30 meV in low Al content narrow GaN/AlGaN QWs [25], but on the other hand the presence of a built-in electric field affects the exciton and biexciton kinetics, so it is of relevance to investigate the drawbacks associated to the QCSE.

Fig. 6.1 (a) shows, in semi-logarithmic scale, the TI PL spectra measured at 10 K on the GaN/$Al_{0.05}Ga_{0.95}N$ QW at an estimated well thickness of ~2.6 nm, for different excitation power densities. The peak at 3.575 eV (±1 meV) corresponds to the recombination from the $Al_{0.05}Ga_{0.95}N$ barrier and the peak at 3.559 eV (±1 meV) is the excitonic recombination (X) from the GaN QW, showing an overall broadening as small as 5.4 meV (±0.3 meV) (for details, see Fig. 6.12).

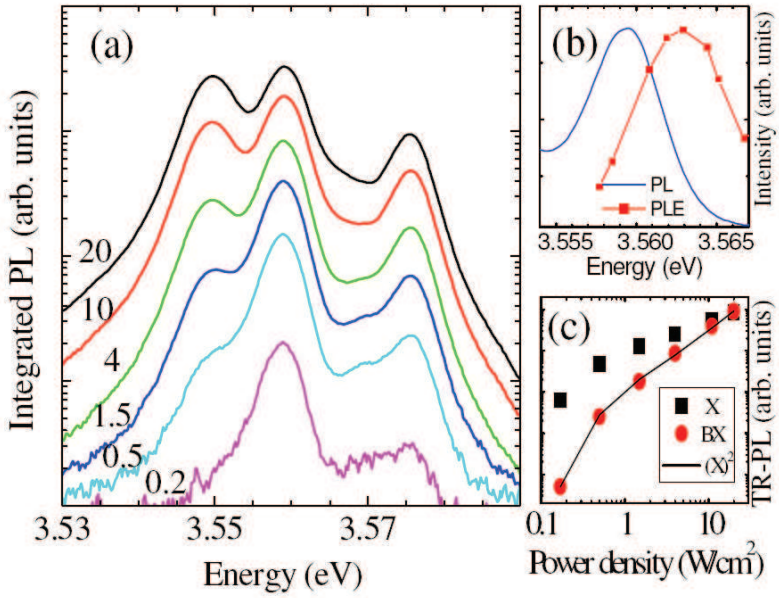

Figure 6.1. (a) TI PL spectra of the 2.6 nm thick GaN/$Al_{0.05}Ga0_{.95}N$ QW measured at 10 K for different excitation power densities (reported in W/cm^2) in semilogarithmic scale. **(b)** Comparison between PL and PLE spectra measured at 10 K. **(c)** Comparison of the X and BX TR PL intensities in logarithmic scale. The line is the square of the X TR PL intensity scaled in order to fit with the BX data.

We report in Fig. 6.1 (b) the comparison between TI PL and PL excitation (PLE) spectra measured at 10 K, denoting a Stokes shift of only 3.6 meV (±0.3 meV), which indicates the high sample quality, even if it is definitely higher respect to the values of GaAs based QWs. When increasing the pump intensity, a peak at about 9 meV (±0.3 meV) below the exciton peak grows superlinearly with the excitation power. This trend is not consistent with bound exciton recombination - in agreement with the low impurity content, the estimated *n*-type background doping being as low as 10^{16} cm^{-3} - which should instead saturate at high excitation. The PL superlinearity is the fingerprint of the biexciton recombination (BX), whose density is predicted to scale quadratically with the exciton population. In order to carefully analyze this point, in Fig. 6.1 (c), we compare the initial exciton and biexciton populations, as obtained from the emission intensity of TR PL spectra with a time window of 70 ps (see also Fig. 6.3) at the PL peak. As expected [105], the exciton recombination exhibits a sublinear increase with increasing excitation power density, while the biexciton perfectly follows the law $BX \propto X^2$. The huge biexciton binding energy very likely reflects both the strong Coulomb interaction in nitrides and, to a lesser extent, the enhancement of the Haynes factor associated with localization due to structural disorder [110].

Let us now address the interplay between biexciton formation and ionization by means of PL spectra taken at different temperatures. TI PL data are shown in Fig 6.2. Very small changes are found between 10 and 20 K, both for X and BX. At 30 K, the X emission intensity is only slightly decreased, while the emission of the BX band is already reduced, and for higher temperatures, the exciton emission also starts to quench.

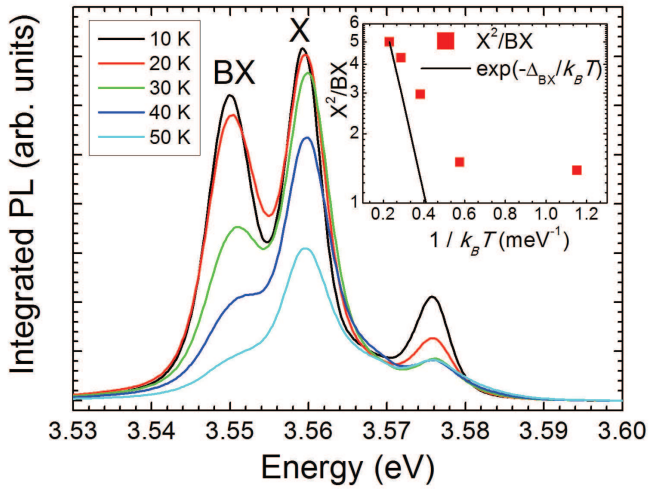

Figure 6.2. TI PL spectra of the 2.6 nm thick GaN/$Al_{0.05}Ga_{0.95}N$ QW measured at different temperatures for a power density of 20 W/cm^2 in a linear scale. Inset semi-logarithmic plot of the ratio between the square of the integrated PL intensity at the X band divided by the BX integrated PL intensity as a function of $1/k_BT$. The dependence expected for the mass law expressed in eq. (70) is also reported for comparison.

As a matter of fact, a thermodynamic and chemical equilibria between X and BX have been observed in GaAs QWs [106], due to the very fast thermalization process as compared with the recombination one. This leads to a mass action law expressed as:

$$\frac{n_X^2}{n_{BX}} \propto \exp\left(-\Delta_{BX}/k_BT\right), \tag{70}$$

where Δ_{BX} is the BX binding energy and n_X and n_{BX} are the exciton and biexciton densities, respectively [106]. The 9 meV biexciton binding energy, to be compared with 1.5 meV in GaAs QWs [105], suggests a much longer time for the biexciton dissociation at low temperatures in GaN QWs, and therefore a different interplay between X and BX is expected. The semi-logarithmic plot of the ratio between the square of the integrated PL intensity at the X band divided by the BX integrated PL intensity is reported as a function of $1/k_BT$ in the inset of Fig. 6.2. Clearly, the BX and X populations are not thermalized at low T, and

eventually, the biexciton ionization starts to play a role, throughout the exciton lifetime, only for temperatures higher than 30 K. Therefore, we can use the TR PL data measured at 10 K to determine the rates for the formation and recombination of the X and BX bands.

The image of the TR PL measured under non-resonant excitation (at ~267 nm, that is, more than 1 eV above the QW exciton transition) is shown in Fig. 6.3 (a), as measured by the streak camera apparatus.

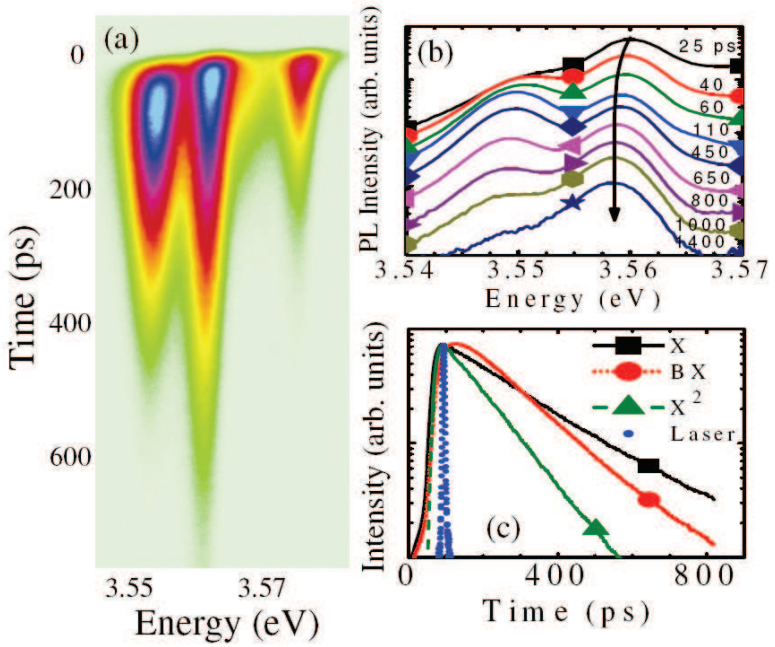

Figure 6.3. (a) Streak image of the TR PL of the 2.6 nm thick GaN/$Al_{0.05}Ga_{0.95}N$ QW measured at 10 K and a power density of 20 W/cm^2 under non-resonant excitation at ~267 nm. **(b)** TR PL spectra at different time delays with time step reported in picoseconds, in semi-logarithmic scale. The line is a guide to the eye. **(c)** Decays of the exciton and biexciton emissions in semi-logarithmic scale. The square of the exciton emission is also reported for comparison, as well as the instrumental response (Laser).

The TR PL spectra, obtained as horizontal cuts of the streak image at different time steps, are reported in Fig. 6.3 (b), showing an energy shift of the X line of approximately 1 meV in the initial dynamics. We found that the observed shift does not depend on the excitation power, as it was found even for the lowest excitation power density of 0.2 W/cm^2 (see Fig. 6.4), and therefore it cannot be attributed to the screening of the piezoelectric field (see subsection §1.3.2). If fact, the estimated carrier density (~2.5×10^{11} cm^{-2}) at the highest excitation power used is well below that where screening effects are expected to occur [111]. As discussed below, we attribute this shift to acoustic phonon mediated relaxation between excitonic localized states.

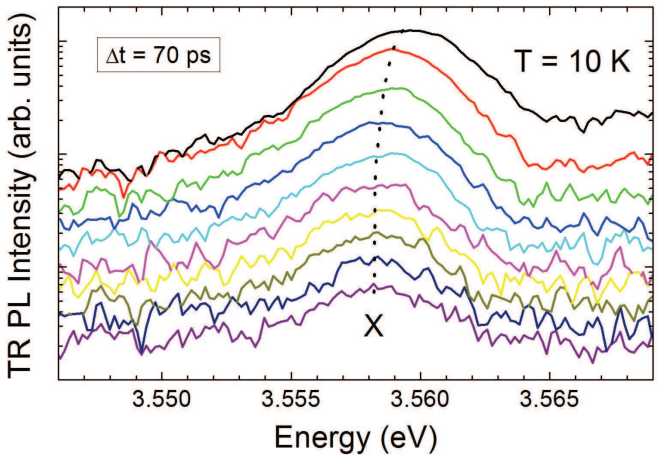

Figure 6.4. TR PL spectra of the 2.6 nm thick GaN/$Al_{0.05}Ga_{0.95}N$ QW measured at 10 K and an excitation power density of 0.2 W/cm^2 in semi-logarithmic scale. The dotted line is a guide to the eye illustrating the red-shift of the X recombination band.

In addition, the X and BX emissions follow different recombination kinetics. This is further elucidated by the time evolution of the X and BX emissions, reported in Fig. 6.3 (c). Clearly, the BX band shows a longer rise time (35 ps (±1 ps)) and a faster decay time (145 ps (±5 ps)) as compared to the excitonic emission (10 ps (±1 ps) rise time, and 210 ps (±5 ps) decay time, respectively). In Fig. 6.3 (c), the square of the excitonic emission is reported for comparison. Such a trend would be expected for the BX time evolution on the basis of thermodynamic equilibrium between X and BX, as already observed in GaAs QWs [106]. Obviously, the BX time evolution in our GaN QW does not support the equilibrium condition. At the same time, assuming that the biexciton will continuously form from excitons with a formation probability proportional to n_X^2, the BX rise time would be given by half the exciton decay time, which is much longer than the experimental findings. This means that the BX formation only occurs during the early stage of the exciton recombination kinetics.

In order to asses the interplay between the biexciton formation and the exciton recombination kinetics, we performed TR PL measurements under resonant excitation. The image of the TR PL, as measured by the streak camera apparatus, is shown in Fig. 6.5 (a) for the detection channel cross polarized with respect to the excitation. The laser energy is tuned at 4 meV above the excitonic PL and appears as a bright spot on the image. The comparison between the time evolutions of the BX (X) emission for resonant and non-resonant excitations is reported in Fig. 6.5 (b) (Fig. 6.5 (c)).

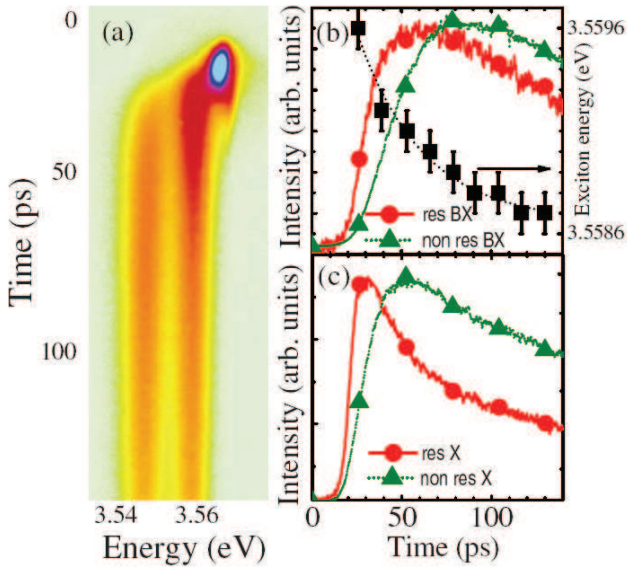

Figure 6.5. (a) Streak image of the TR PL of the 2.6 nm thick GaN/$Al_{0.05}Ga_{0.95}N$ QW measured at 10 K and a power density of 20 W/cm^2 under resonant excitation at ~348 nm. **(b)** Comparison of the BX time evolution for resonant and non-resonant excitation, in linear scale. The energy shift (squares) of the X line under non-resonant excitation, with energy positions extracted from Fig. 6.4, is also shown together with an exponential fit (dotted line). **(c)** Comparison of the X time evolution for resonant and non-resonant excitations in linear scale. The resonant decay corresponds to a detection energy 4 meV below the laser excitation.

In the case of resonant excitation, we directly photogenerated excitons and faster rise times are observed with respect to the non-resonant excitation (where free carriers are photoinjected) for both the X and BX bands. In particular, for resonant excitation, the X band shows a fast initial decay which corresponds to the BX rise time. We attribute this fast initial decay (which is of the order of 20 ps (±1 ps)) to the early stage exciton recombination before thermalization and localization occur. By resonant excitation, the photogenerated excitons undergo radiative recombination in competition with thermalization and acoustic phonon mediated relaxation into localized states at lower energies [112]. On the contrary, in the case of non-resonant excitation, the excitonic formation occurs from photogenerated free carriers, possibly also in high energy exciton states, and therefore exciton recombination arises from a different distribution of excitonic states, which also corresponds to different recombination kinetics, as observed in our samples. The fast initial decay, observed in the case of resonant excitation, cannot be attributed to resonant Rayleigh scattering [112] [113], our excitation being 4 meV above the detected PL. Note that in Fig. 6.5 (a), at the laser energy, we observe a large Rayleigh contribution, dominated by non-resonant elastic scattering, likely due to surface roughness. Finally, the lifetime measured at longer delays nicely corresponds to the one observed for non-resonant excitation, denoting that after interacting with acoustic

phonons, excitons eventually reach a similar distribution, for both resonant and non-resonant excitation conditions.

At the same time, we conclude that the biexciton formation only involves free excitons. Once excitons localize, due to structural disorder in the QW plane, the biexciton formation is quenched and the two populations of X and BX decay with their own radiative lifetimes. This picture is strongly supported by the fact that the exciton energy shift and the BX rise time after non-resonant excitation (see Fig. 6.5 (b)) occur on very similar time scales. It is well known that the TR PL shift indicates that excitons get progressively localized. In this respect, a 35 ps (±1 ps) decay time is found for the X energy shift, which nicely corresponds to the BX rise time under non-resonant excitation. Note also that the dynamical PL shift (less than 1 meV) is, as it applies in our case, only a fraction of the measured Stokes shift between PL and PLE spectra [114]. Another confirmation of our picture arises from the very similar decay time of the exciton band at different excitation powers (not shown here), from values where the BX recombination is very weak to the highest excitation. This means that the biexciton formation involves only exciton states which are not populated at long delays.

Hence, the uncoupled recombination dynamics of X and BX in GaN QWs, associated with the small BX ionization rate, allows us to extract the recombination lifetime of the BX, which is not accessible in GaAs QWs due to the efficient thermalization processes. Theoretically, in quasi-two-dimensional systems, the giant oscillator strength model gives fairly comparable radiative decay rates for excitons and biexcitons [115], while the bipolariton model [116] predicts a very fast decay of biexcitons into interface polaritons. Experimentally, in GaAs QWs, TR PL only reflects the thermal equilibrium [106], whereas four wave mixing experiments show a BX radiative rate which is only slightly larger than the exciton radiative rate [109] [117]. In this respect, the present data would also support the first model, likely due to the fact that the exciton recombination occurs from localized states.

Although in the case of the QW with 9% Al content in the barrier the biexciton binding energy is found to increase up to 12 meV (Fig. 6.6), the recombination scheme is more complicated due to the very rapid localization of the exciton emission. We also notice a significant increase of the emission broadening, of the order of 10 meV (see the following section), likely caused by a higher strain between barriers and well leading to larger band gap variations with respect to the GaN/$Al_{0.05}Ga_{0.95}$N QW. In Fig. 6.6 we show the TR PL spectra under non-resonant excitation at 10 K and at a power density of 20 W/cm^2 for the GaN/$Al_{0.09}Ga_{0.91}$N QW with a time window of ~190 ps between the spectra. While the biexciton recombination band is still present, the X band is found to quickly localize, and only

the localized emission (LX) is visible at longer delays. The strong localization of the emission is most likely due to a higher disorder with respect to the sample with 5% Al content in the barriers, resulting from the higher lattice mismatch between barriers and well layer.

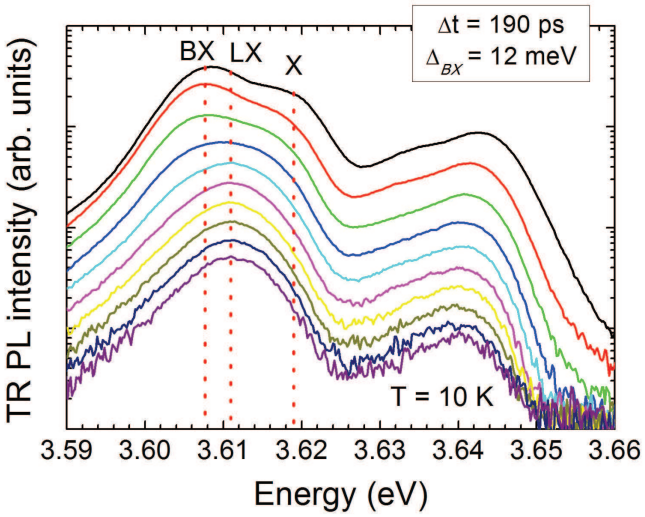

Figure 6.6. TR PL spectra (in semi-logarithmic scale) of the GaN/$Al_{0.09}Ga_{0.91}N$ QW measured at 10 K and at a power density of 20 W/cm^2 under non-resonant excitation at ~267 nm. The dotted lines are guides to the eye indicating the energy positions of the three recombination bands.

While a localization energy of 6 meV (±0.3 meV) is extracted from Fig. 6.6 for the LX band, we find that increasing the sample temperature from 10 K to 30 K is enough to increase the acoustic phonons interaction that leads to a complete delocalization of the LX band (Fig. 6.7). We also note that, as a result of the increased biexciton energy with respect to the GaN/$Al_{0.05}Ga_{0.95}N$ QW, the exchange of population between the X and BX remains negligible at 30 K. Hence, the data obtained at 30 K should be used to draw relevant conclusions on the state of the thermodynamic equilibrium and recombination kinetics of X and BX in the GaN/$Al_{0.09}Ga_{0.91}N$ QW.

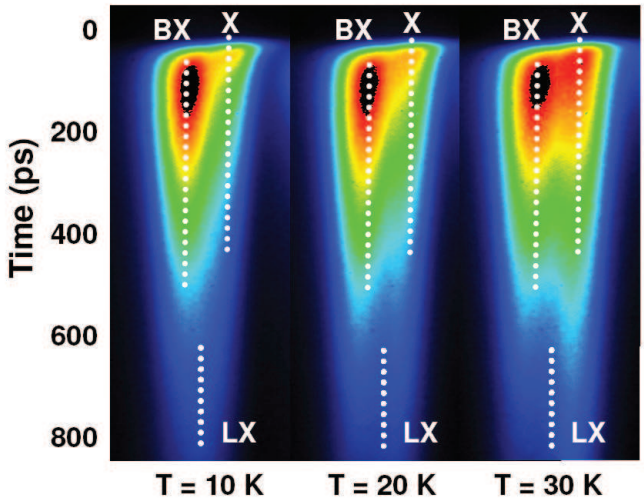

Figure 6.7. Streak images of the TR PL of the GaN/$Al_{0.09}Ga_{0.91}N$ QW measured at 10 K, 20 K, and 30 K, respectively, and a power density of 20 W/cm^2 under non-resonant excitation at ~267 nm.

Following the procedure described for the GaN/$Al_{0.05}Ga_{0.95}N$ QW (Fig. 6.1 (c)) the expected quadratic dependence of the biexciton population on the exciton one is easily verified at 30 K (Fig. 6.8).

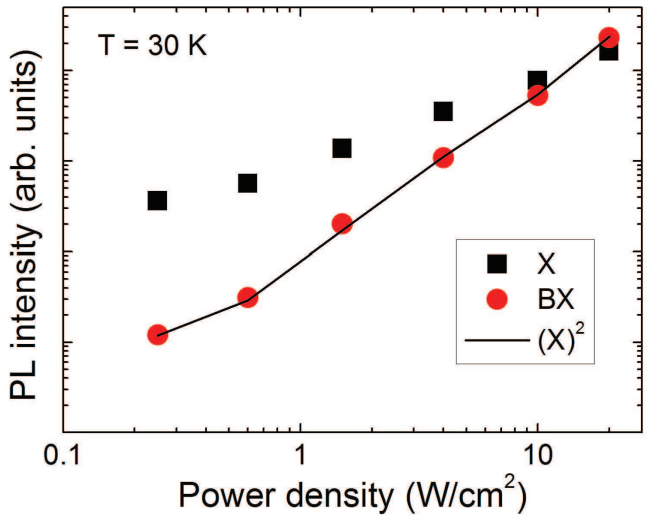

Figure 6.8. Comparison of the X and BX TR PL intensities in logarithmic scale for the GaN/$Al_{0.09}Ga_{0.91}N$ QW at 30 K. The line is the square of the X TR PL intensity scaled in order to fit with the BX data.

In the absence of the localized emission band, we can properly extract radiative lifetimes of the X and BX bands from their decay profiles in order to study the degree of thermalization between them. The results are similar to those obtained for the GaN/$Al_{0.05}Ga_{0.95}N$ QW. A rise time of 10 ps (30 ps) (±1 ps) and a decay time of 390 ps (280 ps) (±5 ps) are extracted for the X (BX) band from the decay profiles shown in Fig. 6.9. We

also report the square of the excitonic emission in Fig. 6.9, which depicts the expected trend for the evolution of a BX population in thermodynamic equilibrium with the X population. Once again, our data do not support the equilibrium condition. The longer lifetimes of the X and BX recombination bands, with respect to the GaN/$Al_{0.05}Ga_{0.95}N$ QW, are a consequence of the increased QCSE present in this structure, resulting in a decreased overlap of the exciton and hole wavefunctions in the well region (see subsection §1.3.2), and, as a consequence, the decrease of their recombination rates.

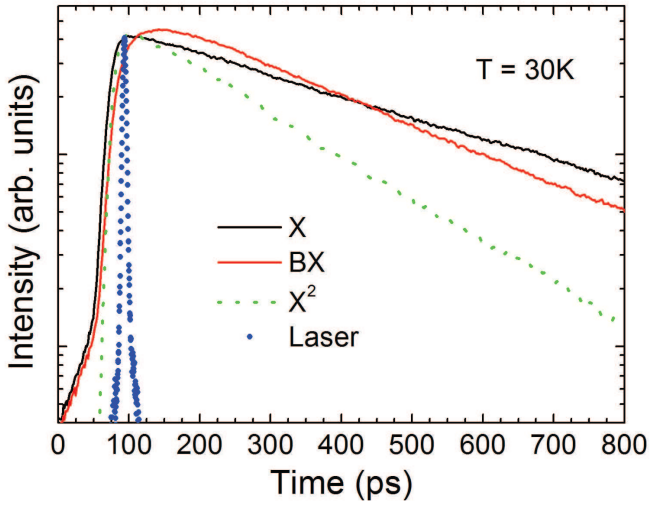

Figure 6.9. Decay profiles of the X (black line) and BX (red line) recombination bands (semi-logarithmic scale) measured at 30 K and at a power density of 20 W/cm^2 for the GaN/$Al_{0.09}Ga_{0.91}N$ QW. The square of the excitonic emission is also reported for comparison (green dotted line), as well as the instrumental response (blue circles).

To conclude this section, we have shown the presence of biexciton recombination in high quality GaN/AlGaN single QWs. We want to emphasize that it is one of the first reports on nitride based nanostrucutre. The observed large biexciton binding energy inhibits the BX ionization during its lifetime, allowing us to elucidate its radiative kinetics. We have also demonstrated that GaN QWs have reached an optical quality equivalent to that of GaAs based nanostructures, allowing us to study the excitonic and biexcitonic formations and recombinations. The increasing biexciton binding energy with increasing Al content in the barriers, which agrees with the findings in AlGaN epilayers [118], can make possible the investigation of biexciton physics above liquid nitrogen temperature (which is also of interest for fundamental physics and applications). Therefore, these findings appear very promising in view of realizing more efficient optoelectronic devices, as well as fundamental studies of the electron-hole correlations in GaN based nanoscale systems. Of particular interest to us is the possibility of using such high quality QWs to investigate the strong coupling regime and the

related properties of high occupancy coherent polariton states in nitride-based QW microcavities in order to overcome the deficiencies presented by bulk GaN MCs in achieving such states (see section §5.5).

Although a good control of the unwanted effects resulting from the presence of QCSE was achieved, we have seen that its effects on the radiative recombination of the X and BX populations in GaN/AlGaN QWs are not negligible, even for thin wells with low Al content in the barriers, and we will discuss these effects in the following sections.

6.3. Impact of quantum confinement and QCSE on biexciton binding energy

The joint action of quantum confinement and QCSE in the two types of GaN/AlGaN QWs (with Al contents in the barrier of 5% and 9%, respectively), discussed in the previous section, was investigated through TR PL measurements by taking advantage of the thickness gradient of the well region.

Images of the TR PL for the two samples, as recorded by the streak camera, are shown in Fig. 6.10. These images were obtained by scanning the excitation spot across the two samples. The spectra in Figs. 6.10 (a) - (c) were taken at a temperature of 10 K and correspond to the sample with 5% Al in the barriers. For the sample with 9% Al content in the barriers, we chose to present the spectra taken at 30 K (Figs. 6.10 (d) - (f)), because of the significant localization of the exciton at a temperature of 10 K, as discussed in the previous section. In Figs. 6.10 (c) and (f), the unmarked bands at higher energy correspond to the PL emission from the $Al_xGa_{1-x}N$ barriers.

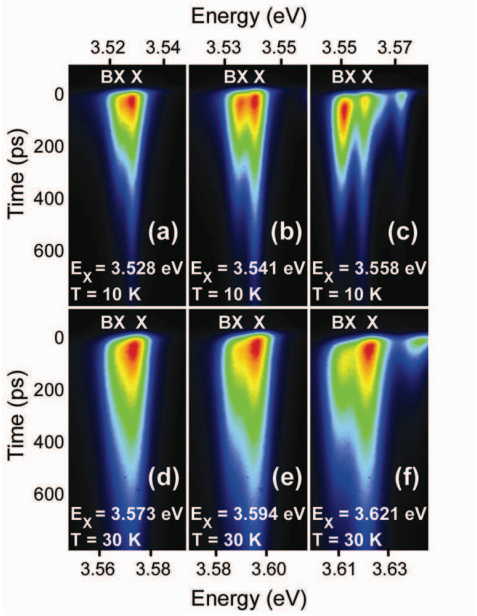

Figure 6.10. TR PL images recorded by the streak camera. The energy of the exciton recombination band E_X is indicated in each figure. **(a) - (c)** Images taken for the GaN/$Al_{0.05}Ga_{0.95}N$ QW at a temperature of 10 K, for different positions on the sample. **(d) - (f)** Images taken for the GaN/$Al_{0.09}Ga_{0.91}N$ QW at a temperature of 30 K, for different positions on the sample. Excitation densities were 80 W/cm^2 for the sample with 5% Al content in the barriers and 15 W/cm^2 for the sample with 9% Al content in the barriers.

As expected, the exciton emission energy increases with decreasing well thickness, *i. e.* increasing quantum confinement. The biexciton emission can be easily distinguished in these images, either as a prominent recombination band in the case of strong confinement (Figs. 6.10 (c) and (f)), or as a shoulder on the lower energy side of the exciton band, for the wider well regions (Figs. 6.10 (a) and (d)). Thus, the increase of the energy splitting between the exciton and biexciton with increasing quantum confinement appears as a straightforward result from the TR PL measurements, and it is a consequence of the confinement enhanced wave function overlap between the excitons, an effect already reported in ZnO/ZnMgO multiple QWs [118].

In the previous sections we already covered fundamental aspects of biexcitons in narrow GaN/AlGaN QWs with low Al content in the barriers, such as the lack of thermalization between excitons and biexcitons at low temperature, and the early stage formation of biexcitons from free excitons. In this section we will focus on the impact of quantum confinement and QCSE on the binding energy of biexcitons in these structures. An important point we would like to address at this stage is the very notion of biexciton "binding energy". In the case of high quality III-V [106] and II-VI [107] QWs, Δ_{BX} is considered as the energy difference between the exciton and biexciton recombination bands in the PL emission

spectra. In the case of ZnO based QWs however, localization effects acting on excitons and biexcitons prevent a precise determination of Δ_{BX} from PL spectroscopy [118]. In fact, values of 50 meV Stokes shift for the exciton recombination band are reported, which are comparable to Δ_X in these systems [118]. In order to clarify this point, we performed simultaneous reflectivity and PL measurements on the same point of the sample. Well resolved structures are found in reflectivity, for both A and B excitons, revealing the intrinsic energy positions of the excitons. A negligible Stokes shift is observed for the A exciton between the reflectivity and the PL spectra (Fig. 6.11), denoting a very small localization effect. Thus, we can properly extract Δ_{BX} by evaluating the energy difference between the exciton and biexciton recombination bands.

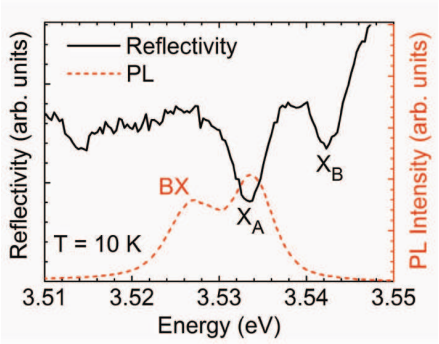

Figure 6.11. Reflectivity (full line) and PL (dashed line) spectra taken in the same point of the GaN/$Al_{0.05}Ga_{0.95}N$ QW at 10 K. The A exciton (X_A) is clearly visible in both spectra at 3.533 eV. The biexciton is only observable in PL.

In order to extract the energy positions of the exciton and biexciton recombination lines, we used the TR PL spectra with a time window of 70 ps after the excitation pulse. Such a value for the time window allows us to avoid the contribution of localized states to the PL, which become dominant at long delays. The experimental data (squares) were fitted using two Gaussian line shapes. The results are presented in Fig. 6.12, with spectra in Fig. 6.12 (a) (Fig. 6.12 (b)) associated to the recombinations depicted in the streak images of Figs. 6.10 (a) - (c) (Figs. 6.10 (d) - (f)), respectively.

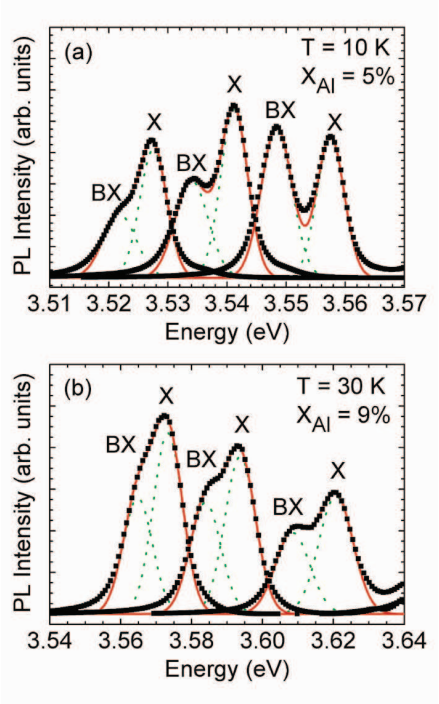

Figure 6.12. Experimental TR PL spectra measured at short delay (squares) relative to Fig. 6.10. The full lines are the sum of the fitting Gaussian line shapes (dotted lines).
(a) From low energy to high energy, spectra associated with Figs. 6.10 (a) - (c).
(b) From low energy to high energy, spectra associated with Figs. 6.10 (d) - (f).

A linewidth of 5.4 meV (±0.3 meV) was extracted from the fit of the exciton band of the GaN/$Al_{0.05}Ga_{0.95}N$ QW, while for the biexciton band we estimated a broadening of 6.6 meV. Equal line broadening values were used to fit the X and BX bands for the GaN/$Al_{0.09}Ga_{0.91}N$ QW, but their value was found to vary across the sample, and they turned out to be larger than the ones used for the GaN/$Al_{0.05}Ga_{0.95}N$ QW. In fact, as discussed in the previous section, a higher Al content in the barrier, with respect to the sample with 5% Al, leads to an increased impact of alloy disorder, thereby increasing the inhomogeneous broadening of the X and BX bands. These fluctuations have a higher weight for smaller well widths, and hence the linewidths used to fit the two recombination bands in Fig. 6.12 (b) increase from 9.8 meV for the lower energy spectrum, to 11.4 meV (±0.3 meV) for the higher energy one. For both samples, the energy difference between the Gaussian fits of the X and BX bands was taken as the biexciton binding energy.

This fitting procedure was repeated for all the spectra acquired along the thickness gradient of the two samples. The resulting biexciton binding energies as a function of the exciton energy and QW thickness are depicted in Figs. 6.13 (a) and (b), respectively. The latter set of data has been deduced by modeling QW interband transitions using envelope

function calculations including an electric field of 270 and 500 kV/cm for the samples with 5% and 9% Al content in the barriers, respectively [119].

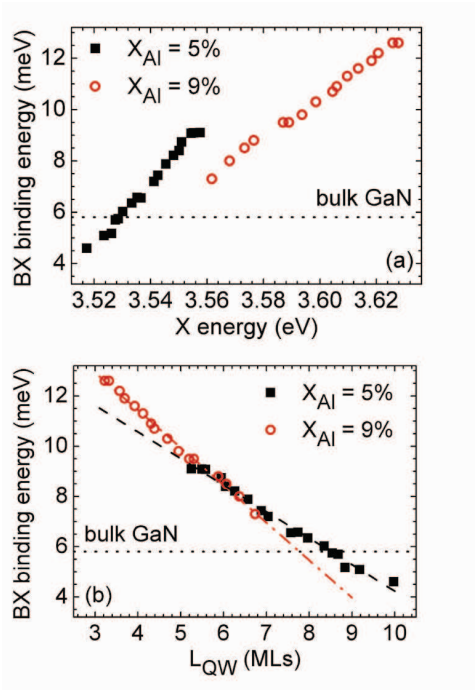

Figure 6.13. Biexciton binding energy as a function of **(a)** exciton emission energy and **(b)** the QW thickness for various points on the sample, for the two GaN/AlGaN QWs with 5% As content in the barriers (squares) and 9% Al content in the barriers (circles), respectively. Least square linear fits of the two sets of data in Fig. 6.13 (b) are represented as a dashed line (5%) and a dash dotted line (9%), respectively. The biexciton binding energy of the GaN buffer layer is represented as a dotted line.

For each barrier height, Δ_{BX} increases monotonously with increasing quantum confinement, up to a limit where the exciton emission energy is very close to the emission from the AlGaN barrier. The highest measured values of biexciton binding energies are 9.1 meV for the GaN/$Al_{0.05}Ga_{0.95}N$ QW, and 12.6 meV for the GaN/$Al_{0.09}Ga_{0.91}N$ QW. An interesting result to note is the smallest measured biexciton binding energy, of only 4.6 meV in the GaN/$Al_{0.05}Ga_{0.95}N$ sample, which is below the 5.8 meV BX binding energy measured in the 3 µm GaN buffer layer (dotted line) of the same structure. The crossover from Δ_{BX} values exceeding that measured in bulk GaN to values lower than the latter occurs at a QW thickness of about 9 monolayers (MLs), *i. e.* a thickness close to that where a similar transition is reported for the case of QW interband transition energies [119]. This can be attributed to the significant QCSE present in GaN based QWs [120]. Even for a small Al concentration in the barriers (5%), this field is strong enough to reduce the biexciton binding energy below that of bulk GaN, although the energy of the exciton recombination band is slightly higher than that of bulk GaN. Note also that the knowledge of Δ_{BX} gives access to an indirect estimate of Δ_X,

as the latter has been shown to be linked to Δ_{BX} in two-dimensional systems through the ratio $\Delta_{BX}/\Delta_X = 0.228$ [121]. Such an expression is expected to be valid even in the presence of an electric field. In the present case, it would lead to exciton binding energies spanning from 20 meV for the largest well thickness investigated here to 55 meV for the thinnest one. We note that, due to strong QCSE present in the thick GaN/$Al_{0.09}Ga_{0.91}$N QW, we find that not only the biexciton binding energy, but also the exciton binding energy is below that of bulk GaN, as predicted [78].

Finally, we point out that for QWs larger than 3 MLs, theoretical calculations indicate that Δ_X starts to be strongly affected by the QCSE, thereby inducing an increased electron-hole pair separation, which results in a decrease of Δ_{BX} proportional to the internal electric field present in the QWs [122]. Hence, the crossing between the two sets of data in Fig. 6.13 (b) (as emphasized by the least square linear fits) suggests that for thin QWs, where the quantum confinement dominates, Δ_{BX} will be larger for the structure with 9% Al content in the barriers. Conversely, for thick QWs, Δ_{BX} will be larger for the structure with 5% Al content in the barriers, as the impact of the QCSE is smaller in these wells.

To conclude this section, TR PL measurements performed in two types of GaN/Al_xGa_{1-x}N QWs with low Al content in the barriers reveal an increase of the biexciton binding energy with increasing quantum confinement. For low quantum confinement values, the BX binding energy is found to decrease in the GaN/$Al_{0.05}Ga_{0.95}$N QW below that of bulk GaN. This result is a fingerprint of the strong QCSE present in these structures.

We would also like to note at this point the observation of a feature in the reflectivity spectra of the GaN/$Al_{0.05}Ga_{0.95}$N QW (Fig. 6.11), attributed to the *B* exciton (X_B). The clear observation of the *B* exciton absorption line was likely made possible by the very small disorder, leading to sharp excitonic transitions, in the GaN/$Al_{0.05}Ga_{0.95}$N QW. This is a result which, to our knowledge, has not been reported previously in literature, and therefore it triggered our interest to gain a deeper insight on the physics behind the *B* exciton transition in our sample, and it is the topic discussed in the following section.

6.4. *B* exciton recombination kinetics and impact of quantum confinement on *A* and *B* exciton energy splitting

In order to gain access to the *B* exciton recombination kinetics a suitable point on the GaN/$Al_{0.05}Ga_{0.95}N$ QW needed to be found, in which the recombination from the barrier would not mask the X_B band. In Fig. 6.14 we present the TR PL spectra with a time delay of 30 ps at 10 K and at a power density of 80 W/cm^2 under non-resonant excitation at ~267 nm corresponding to an energy of the X_A recombination band of ~3.527 eV (±1 meV). The X_B recombination is clearly visible as a shoulder on the higher energy side of the spectra, approximately 10 meV above the X_A band, which is a value estimated from the reflectivity measurement taken in the same point of the sample (not shown here).

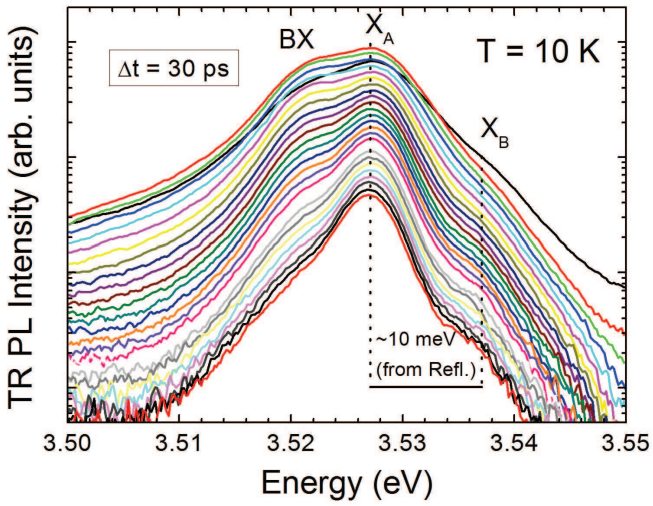

Figure 6.14. TR PL spectra (in semi-logarithmic scale) of the GaN/$Al_{0.05}Ga_{0.95}N$ QW with a time window of 30 ps taken at 10 K and at a power density of 80 W/cm^2 under non-resonant excitation at ~267 nm.

From each of the TR PL spectrum in Fig. 6.14 we subtracted an exponential decay that fits the shoulder of X_A, as illustrated in the inset of Fig. 6.15. We point out that a background was added to the fitting of the exponential decay to account for the background signal in the PL spectra. The spectra resulting from this subtraction procedure are presented in Fig. 6.15, and they represent the evolution of the X_B recombination band at each time step.

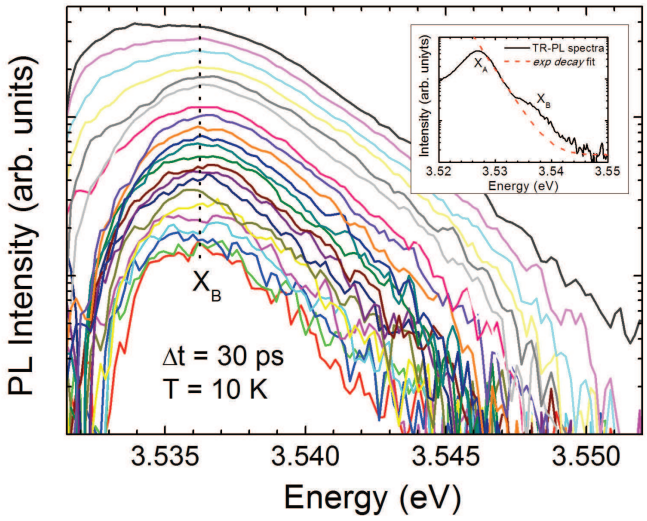

Figure 6.15. TR PL spectra of the X_B recombination band extracted from Fig. 6.13 following the subtraction procedure illustrated in the inset.

A shoulder can be seen on the higher energy side of the X_B band for short delays because we kept the same decay constant in the subtracted exponential decay throughout the fitting procedure, although the shoulder of the X_A band changes inclination, likely due to an instrumental effect. However, we consider that this fitting approach gives a fairly good estimate for the time evolution of the X_B recombination band. The time dependence of the X_B band intensities, as extracted from Fig. 6.15, is reported in Fig. 6.16 in semi-logarithmic scale.

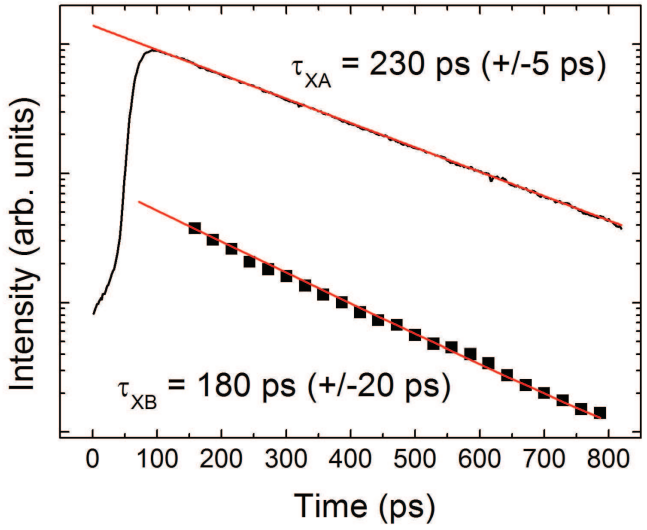

Figure 6.16. Decay profiles (in semi-logarithmic scale) of the X_B recombination band (black squares) and X_A recombination band (black line), and their respective exponential decay fits (red lines).

We retrieve a 180 ps (±20 ps) lifetime for the *B* exciton recombination band (τ_{XB}) from the partial decay of Fig. 6.16. We also report the decay profile of the X_A band for comparison, which is found to have a lifetime of 230 ps (±5 ps) (τ_{XA}) in this point of the sample using an exponential decay fit. The similar decay times of the two populations reflect similar recombination kinetics, as well as a strong interaction between the two states, as evidenced by TR PL measurements with the energy of the excitation resonant with the X_A band. In fact, we find identical contributions of the X_B recombination band in the PL spectra for both X_A-resonant and non-resonant excitation (not shown here), indicating a possible thermodynamic equilibrium between the two populations.

The remarkable observation of the *B* exciton recombination band in both reflectivity and PL was made possible by the high optical quality of our GaN/$Al_{0.05}Ga_{0.95}$N QW, resulting in a small inhomogeneous broadening of the excitonic transitions and a reduced influence of the QCSE. However, as we have seen for biexcitons, the variation of quantum confinement and QCSE with well thickness can give rise to interesting effects. In the following we will investigate the effect of quantum confinement of the A-B excitonic splitting.

In Fig. 6.17 we present the reflectivity (dotted line) and PL (solid line) spectra taken in the same point of the GaN/$Al_{0.05}Ga_{0.95}$N QW at 10 K, with X_A at 3.533 eV (±1 meV). As mentioned previously, a negligible Stokes shift is observed for X_A between the reflectivity and the PL spectra, denoting a very small localization effect. While prominent features can be observed for X_A in both reflectivity and PL, X_B is quite visible in reflectivity, and it only appears as a shoulder on the high energy side of X_A (marked by an arrow) in PL, likely due to the thermalization effects already discussed. The presence of the biexciton (BX) in the QW emission spectrum has been discussed in the previous sections of this chapter. The features visible on the low energy side of Fig. 6.17 correspond to the *A* and *B* excitons and to the biexciton of the GaN buffer layer, but they were left unmarked to avoid confusion.

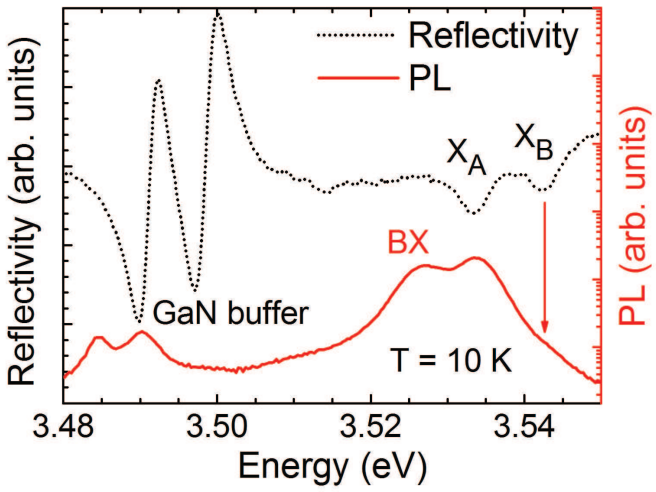

Figure 6.17. Reflectivity (dotted line) and photoluminescence (solid line) spectra taken in the same point of the GaN/$Al_{0.05}Ga_{0.95}N$ QW at T = 10 K. On the high energy side of the plot, X_A (X_B) designates the A (B) exciton feature of the QW, while BX refers to the biexciton emission from the QW observable only in PL. On the low energy side of the plot, similar features can be seen for the GaN buffer layer.

From the reflectivity spectrum displayed in Fig. 6.17, we extract a 7.3 meV (±0.3 meV) energy splitting between the *A* and *B* excitons of the GaN buffer layer, a value which is consistent with those found by other authors for GaN layers grown on *c*-plane sapphire substrates [40] [41] [123]. However, the value extracted for the energy splitting between X_A and X_B corresponding to the QW is found to be 9.1 meV (±0.3 meV), which is a clear indication of the effect of quantum confinement on the energy splitting between these two excitons.

In order to extract the variation of the energy splitting between X_A and X_B with quantum confinement, we took advantage of the thickness gradient of the well region, and we acquired several reflectivity spectra at different positions across the sample (Fig. 6.18). As expected, the energy positions of X_A and X_B increase with increasing quantum confinement, whereas the energies of the GaN buffer features (*buffer* in Fig. 6.18) and $Al_{0.05}Ga_{0.95}N$ barriers (*barrier* in Fig. 6.18) remain unchanged. This proves that a change in quantum confinement is caused by a change of the well width, and not by a variation of the barrier height (*i. e.* a variation of the Al content in the barriers).

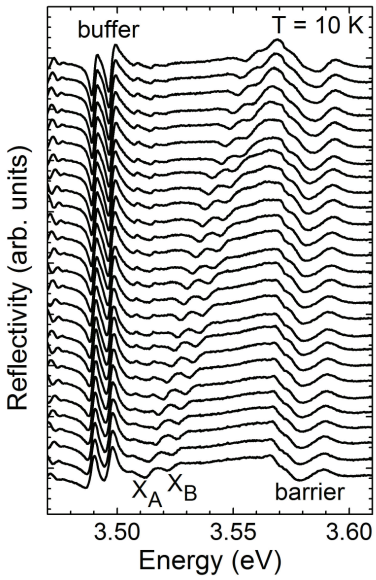

Figure 6.18. Reflectivity spectra taken in different positions across the well thickness gradient of the GaN/$Al_{0.05}Ga_{0.95}N$ QW at T = 10 K. The spectra are shifted in intensity for the sake of clarity.

Fig. 6.19 shows the energy splitting between X_A and X_B, as extracted from the reflectivity spectra of Fig. 6.18, as a function of X_A (squares).

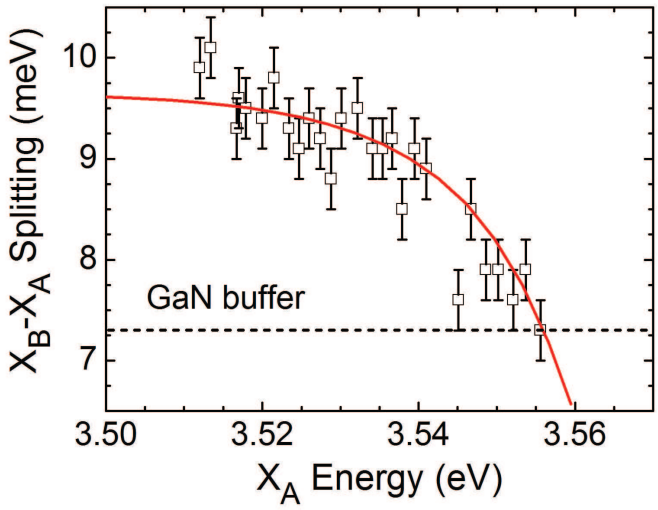

Figure 6.19. Energy splitting between X_A and X_B of the GaN/$Al_{0.05}Ga_{0.95}N$ QW as a function of the A exciton energy position (squares), as deduced from the reflectivity spectra in Fig. 6.17. The theoretical fit to the experimental data is shown as a full line. The value of the energy splitting between the A and B excitons of the GaN buffer layer of our sample is reported as a dotted line.

The clear enhancement of the energy splitting between the two excitons is attributed to the presence of quantum confinement in our quantum well. The impact of quantum

confinement is stronger for X_B which corresponds to a higher state than X_A, hence the increase of the energy splitting from 7.3 meV measured for our GaN buffer layer (dotted line) up to around 10 meV measured for the thicker well achieved in our sample. Ideally, if the two excitons were placed in a QW with infinite barriers, their energy splitting should increase with increasing confinement (*i. e.* when reducing well width). However, in our case, the decreasing trend of the energy splitting between X_A and X_B can be explained by the presence of AlGaN barriers with only 5% Al content. Hence, when decreasing the well thickness, while the energies of both X_A and X_B increase, X_B approaches the barrier limit before X_A does, so that the electron and hole wavefunctions of X_B are more sensitive to delocalization effects outside the well region making the overall energy enhancement due to the increase in quantum confinement smaller than for X_A. Eventually, for the largest confinement values obtained on the sample, the energy splitting between X_A and X_B approaches that of bulk AlGaN barriers.

The decreasing trend of the splitting with increasing quantum confinement is in good agreement with theoretical simulations performed by our colleagues at the University of Rome "Tor Vergata" using the TiberCAD simulation tool [124] [125]. In these calculations, a strain model is applied [126], based on the continuous elasticity theory, which allows to include the effects of strain, piezo and spontaneous polarization fields in the Poisson equation. Surface states are taken into account by imposing a Fermi level pinning boundary condition to the AlGaN layer. Then, quantized states are obtained by using an 8-band $\boldsymbol{k} \cdot \boldsymbol{p}$ approximation [127] with the parameters reported in Ref. [33]. For the theoretical curve reported in Fig. 6.19 (solid line), a valence band offset (VBO) of 30% and a 35 meV average exciton binding energy, for both X_A and X_B, were considered. We also note that, quantitatively, the variation of the theoretical splitting between X_A and X_B was found to be of the order of 3% when changing the VBO between 25% and 32%.

To conclude this section, the recombination kinetics of the *B* was extracted from the TR PL spectra at low temperature for the GaN/$Al_{0.05}Ga_{0.95}N$ QW, while reflectivity measurements performed showed an enhancement of the energy splitting between the A and B excitons, with respect to a bulk GaN structure, due to the presence of quantum confinement. However, with reducing well width, the effect of the finite barriers causes a larger delocalization of the electron and hole wavefunctions of X_B, and, consequently, a reduction of the energy splitting between X_A and X_B, in very good agreement with theoretical simulations.

6.5. Conclusions of the chapter

The very high optical quality of the state-of-the-art samples discussed in this chapter allowed us to gain insights on fundamental physical properties never observed before in GaN based quantum wells. The use of barriers with low Al content, together with an optimized growth of thin well regions, proved crucial in reducing the negative effects related to alloy fluctuations in the barrier and the presence of QCSE. This made possible the first observation of the biexciton recombination in nitride based quantum wells, a fingerprint of their very high quality, comparable to that of their GaAs counterparts. Moreover, the large biexciton binding energy allowed the determination of the intrinsic radiative rates of the X and BX populations directly from TR PL measurements, something that was not possible for GaAs QWs due to the existence of a thermodynamic equilibrium between the two populations.

While a strong enhancement of the binding energies of excitons and biexcitons with increasing quantum confinement was observed, the QCSE was also found to have a significant impact for increased thicknesses of the well region (> 9 MLs), resulting in a reduction of their values below those of bulk GaN. Finally, owing to the very small inhomogeneous broadening of the excitonic transitions, the presence of the *B* exciton was resolved for the first time in such a structure, both in PL and reflectivity, and the dependence of the *A*-*B* exciton energy splitting with quantum confinement was measured.

The increased exciton binding energy, high oscillator strength, and small inhomogeneous broadening of the emission of such thin GaN/AlGaN QWs with low Al content in the barriers are strong arguments in favour of their integration as active media in GaN based QW microcavities for the achievement of a strong coupling regime, and, eventually, of a polariton condensate. However, at the time this study was realized, such a structure was not available for us to investigate.

7. Conclusions

In this work we presented an experimental study of two types of GaN based nanostructures: bulk GaN microcavities (and related heterostructures) and GaN/AlGaN quantum wells with low Al content in the barriers. The driving force behind the study of such structures was the achievement of a GaN based microcavity exhibiting the formation of a polariton condensate at room temperature.

The first chapter emphasizes the advantages of the excitonic properties of bulk GaN and GaN quantum wells over more traditional materials, such as GaAs based nanostructures. In fact, the existence of a direct band gap at the Γ valley favouring optical transitions, the possibility of tuning the emission from IR to deep UV, when ternary and quaternary alloys with Al and In are considered, and a large binding energy that allows excitons to be stable up to room temperature (and beyond) suggest that GaN related materials are indeed the best choice for the realization of next generation optoelectronic devices. As a matter of fact, GaN related nanostructures have dominated the market of optoelectronics ever since the 1990s, with the realization of the first GaN based commercial LEDs, up until the present day, with the implementation of GaN based laser diodes in high-tech devices such as the Blu-ray Disc.

While these devices have largely overcome the physical limitations of their arsenide counterparts, the high strain was shown to give rise to numerous structural defects, which raised questions about the possibility of achieving subtle quantistic effects such as the Bose-Einstein condensation of polaritons in a GaN based quantum well microcavity. The presence of disorder and QCSE proved to have a strong negative impact on the excitonic properties of GaN/AlGaN single QWs alone, which led growers to discard them as possible active media in a GaN based microcavity, in a first approach, and to consider bulk GaN instead.

Thus, the transfer matrix formalism presented in the second chapter was adapted to describe the coupling of excitons and photons in a Fabry-Pérot-like resonator considering a bulk GaN active layer as the source of excitation. We presented simulations of optical parameters (reflectivity, quality factor), specific of the heteroepitaxial components making up the resonator (DBRs) that would accommodate a bulk GaN active layer. Important conclusions were drawn, such as the number of $\lambda/4$ layers that should be used for a DBR in order to achieve a satisfactory reflectivity. We have also shown how the strong coupling between excitons and cavity photons strongly modify their dispersion curves giving rise to a

new particle - the *polariton* - which is a linear superposition of the two uncoupled states. We estimated a Rabi splitting of the order of 35 meV for a fully epitaxial bulk GaN microcavity, considering the 1 meV longitudinal transverse splitting reported in literature. Such a large value for the Rabi splitting, compared to that of 5 - 7 meV for GaAs MCs, assures the stability of polaritons at room temperature, providing a perspective to achieve a polariton condensate at this temperature.

However, because of the strong strain effects lowering the optical quality of GaN based heterostructures, the practical achievement of the predicted room temperature strong coupling in a bulk λ/2 GaN microcavity proved to be a lengthy process that required a continuous optimization and reevaluation of the growth parameters. The experimental results presented in chapter §5 trace the evolution of microcavity related heterostructures into complete bulk GaN microcavity structures. We showed that even for simple nanostructures such as GaN epilayers the design of the sample has a decisive effect on its optical quality, due to uncertainties in controlling strain related effects during the growth process. The broadening of the free excitonic emission was found to increase up to a factor of two when using buffer layers in order to relief the strain between the substrate and the epilayer. Hence, the introduction of additional structural defects through the use of buffer layers outweighed the benefits of having a more relaxed epilayer. Moreover, the need to achieve structures that could be easily adapted for large scale production and integration into practical devices led to the growth of subsequent microcavities and related heterostructures without the use of buffer layers.

Strain related defects were still found to have an important influence on the optical properties of our samples, accounting for the strong reduction of the AlN/$Al_{0.2}Ga_{0.8}N$ bottom DBR's stop band from the theoretically predicted value of 330 meV to the ~150 meV (±10 meV) measured experimentally, as well as the very short exciton lifetime (~3 ps) in the active layer of the λ/2 GaN half cavity indicating a major role of non-radiative channels in the recombination kinetics. In fact, the defect density in a fully epitaxial bulk GaN microcavity was so high that no coupling between the exciton and photon modes was observed. The first breakthrough towards the coupling of the two modes was achieved by employing a top Al mirror instead of an epitaxial one, but this allowed only the weak coupling of the two states, resulting in a decreased broadening of the emission from the cavity, in agreement with theoretical predictions.

A major step in increasing the quality factor of the resonator was the replacement of the top Al mirror with a dielectric DBR made of amorphous Si_3N_4/SiO_2 λ/4 layers. Their increased refractive index ratio $n_{Si_3N_4}/n_{SiO_2}=1.341$, compared to $n_{Al_{0.2}Ga_{0.8}N}/n_{AlN}=1.164$, as well as the fact that these layers were not subject to the same strain related structural defects as the underlying heteroepitaxial λ/2 GaN half cavity resulted in an increase of the microcavity quality factor from ~35, in the case of the Al top mirror, to ~150. This allowed the observation of a clear anticrossing of the polariton modes in both reflectivity and photoluminescence measurements from 10 K to 300 K, demonstrating the presence of a strong coupling even at room temperature. The strong coupling was also evidenced by the decrease of the emission broadening and lifetime of the lower polariton with increasing its photonic fraction.

While the population of the upper polariton through acoustic phonon interactions was found to be more efficient with increasing temperature, the very short lifetime of the emission from the lower polariton (< 3 ps) raised questions about the state of thermalization of the two polariton branches. This point was elucidated by comparing the experimental LP PL spectra at resonance with the PL deduced from the absorption spectra in the same point of the sample multiplied by a Boltzmann filling factor corresponding to a temperature of 300K. The very good agreement between the two spectra demonstrates the existence of very efficient energy relaxation processes in our bulk GaN microcavity, mainly through acoustic phonon interactions. This aspect is in sharp contrast with the findings on GaAs based microcavities where a strong polariton bottleneck was found to inhibit the relaxation of lower polaritons towards low *k* state, thus forbidding the formation of a condensate in non-resonant excitation conditions.

In order to check for the existence of a relaxation bottleneck in our GaN microcavity, we performed angle resolved PL measurements at various temperatures and different detunings, which allowed us to determine the occupancy of the polariton branches. At low temperatures we find an enhancement of the LP PL at angles where the two modes anticross, denoting the presence of the relaxation bottleneck in our structure. However, a reduction of the emission enhancement is observed with increasing the temperature of the sample, and a complete suppression of the relaxation bottleneck is found at room temperature. We conclude that at room temperature the exciton - acoustic phonon interaction is the dominant relaxation mechanism through which the lower *k* states are populated, as supported by theoretical simulations based on semi-classical Boltzmann equations.

In spite of the significant advantages that our bulk GaN microcavity seems to offer over GaAs based MCs, such as the stability of the strong coupling at 300 K and the very efficient energy relaxation of the lower polariton, we do not find a marked superlinear increase of the LP emission at $k = 0$ when increasing power density. This is an indication that the strong disorder still present in our structure, mainly caused by strain related effects, prevents the achievement of a polariton condensate.

The subsequent study of narrow GaN/AlGaN quantum wells with low Al content in the barriers was motivated by the need to improve the excitonic properties of existing microcavity structures. The first observation of biexciton recombination in these wells, a proof of their very high optical quality, denoted a major breakthrough in controlling the alloy fluctuations and the QCSE. The observed large biexciton binding energy (up to ~12 meV) inhibits the biexciton ionization during its lifetime for low temperatures, allowing us to elucidate its radiative kinetics. This proved to be an interesting aspect which could not be resolved in GaAs-based and II-VI QWs due to the presence of thermodynamic equilibrium between the two populations and/or large emission broadenings.

While a strong enhancement of the binding energies of excitons (up to ~55 meV) and biexcitons with increasing quantum confinement was observed, the QCSE was also found to have a significant impact for increased thicknesses of the well region (> 9 MLs), resulting in a reduction of their values below those of bulk GaN.

We also pointed out that the small broadening of the *A* exciton recombination band, of the order of ~5 meV in the QW with 5% Al content in the barrier, allowed the first observation of the *B* exciton in such a structure, both in PL and reflectivity. While the *A*-*B* exciton energy splitting was found to be enhanced by the quantum confinement, with respect to the bulk case, the effect of the finite barriers causes a larger delocalization of the electron and hole wavefunctions of the *B* exciton, and, consequently, a reduction of the energy splitting, in very good agreement with theoretical simulations.

The remarkable optical properties of these structures establish them as the state-of-the-art in the field of GaN based single QWs and recommend them for further integration in GaN based QW microcavities for the achievement of a strong coupling regime, and, eventually, of a polariton condensate.

Perspectives

Although in this study we were not able to present the achievement of a coherent emission arising from a polariton condensate, room temperature polariton lasing was eventually demonstrated very recently both for a bulk GaN microcavity [128] and a GaN/AlGaN multiple QW microcavity [129]. The improved optical quality of these MCs however came at the expense of realizing more elaborate structures. The use of lattice matched λ/4 layers in the bottom DBR resulted in a decreased refractive index ratio of these layers, and hence ~3 times as many layers were employed for the bottom DBR with respect to our bulk GaN MC. Moreover, the samples were deposited on high-quality GaN templates, grown on sapphire, making them expensive to realize and difficult to integrate in optoelectronic devices.

In order to obtain a structure that is feasible for mass production and easy integration, on the basis of the research presented in this thesis, a different design can be proposed that assumes that the entire growth is done by MOVPE instead of MBE. Also, this structure must allow a precise control of doping, which is hard to achieve if the DBRs are made out of heteroepitaxially grown layers. The proposed design assumes a full hybrid microcavity that has both the top and bottom DBRs made of Si_3N_4/SiO_2 λ/4 layers. The first DBR should be deposited on a high quality GaN bulk layer or multiple QW structure. Next, the substrate/buffer should be removed, and the bulk/QW active layer should be etched down to a desired thickness of $m\lambda/2$. The microcavity should be completed by the deposition of another Si_3N_4/SiO_2 DBR on the etched side of the active layer. Very high quality GaN based microcavities would be eventually obtained through this approach, which also allow an efficient control of their doping properties, making them easy to integrate in optoelectronic devices.

List of publications

[P1] I. R. Sellers, F. Semond, M. Leroux, J. Massies, M. Zamfirescu, F. Stokker-Cheregi, M. Gurioli, A. Vinattieri, M. Colocci, A. Tahraoui, and A. A. Khalifa, Phys. Rev. B **74**, 193308 (2006).

[P2] I. R. Sellers, F. Semond, M. Zamfirescu, F. Stokker-Cheregi, P. Disseix, M. Leroux, J. Leymarie, M. Gurioli, A. Vinattieri, F. Réveret, G. Malpuech, A. Vasson, and J. Massies, Phys. Stat. Sol. B **244**, 1882 (2007).

[P3] M. Gurioli, M. Zamfirescu, F. Stokker-Cheregi, A. Vinattieri, I. R. Sellers, F. Semond, M. Leroux, and J. Massies, Superlattices Microstruct. **41**, 284 (2007).

[P4] F. Stokker-Cheregi, M. Zamfirescu, A. Vinattieri, M. Gurioli, I. R. Sellers, F. Semond, M. Leroux, and J. Massies, Superlattices Microstruct. **41**, 376 (2007).

[P5] F. Stokker-Cheregi, A. Vinattieri, E. Feltin, D. Simeonov, J.-F. Carlin, R. Butté, N. Grandjean, and M. Gurioli, Phys. Stat. Sol. C **5**, 2254 (2008).

[P6] F. Stokker-Cheregi, A. Vinattieri, M. Colocci, F. Semond, M. Leroux, J. Massies, I. R. Sellers, and M. Gurioli, Phys. Stat. Sol. C **5**, 2257 (2008).

[P7] F. Stokker-Cheregi, A. Vinattieri, E. Feltin, D. Simeonov, J.-F. Carlin, R. Butté, N. Grandjean, and M. Gurioli, Phys. Rev. B **77**, 125342 (2008).

[P8] F. Stokker-Cheregi, A. Vinattieri, F. Semond, M. Leroux, I. R. Sellers, J. Massies, D. Solnyshkov, G. Malpuech, M. Colocci, and M. Gurioli, Appl. Phys. Lett. **92**, 042119 (2008).

[P9] F. Stokker-Cheregi, A. Vinattieri, E. Feltin, D. Simeonov, J. Levrat, J.-F. Carlin, R. Butté, N. Grandjean, and M. Gurioli, Appl. Phys. Lett. **93**, 152105 (2008).

Participation to conferences

[C1] 6th International Conference on Physics of Light and Matter Coupling in Nanostructures (PLMCN6), September 2006, Magdeburg, Germany. (poster)

[C2] 7th International Conference on Physics of Light and Matter Coupling in Nanostructures (PLMCN7), April 2007, Havana, Cuba. (poster)

[C3] 7th International Conference on Nitride Semiconductors (ICNS7), September 2007, Las Vegas, USA. (2 oral presentations)

[C4] New Frontiers in Micro and Nano Photonics, April 2008, Florence, Italy. (oral)

Acknowledgements

I would like to thank Prof. Massimo Gurioli for the invaluable support he provided me throughout my stage.

I must acknowledge the European Community for the funding provided through the EC-TRN 'CLERMONT2' program, contract no. MRTN-CT-2003-503667, without which my stay in Florence would not have been possible.

Thanks to Prof. Marcello Colocci for giving me the possibility to work in the department conducted by him and for making me feel welcome.

I acknowledge the fruitful collaborations with our colleagues from the CLERMONT2 project, particularly the groups of CRHEA-CNRS, EPFL, LASMEA CNRS, and University of Rome "Tor Vergata".

Thanks to Marian Zamfirescu for his patience in guiding my first steps in the world of microcavities and ultra-fast spectroscopy.

I am grateful to Marco Abbarchi for helping me out with all the little things that tend to be forgotten at the end of the day.

List of abbreviations

ABE - acceptor bound exciton

BEC - Bose-Einstein condensation

BX - biexciton

CCD - charged coupled display

CW - continuous wave

DBE - donor bound exciton

DBR - distributed Bragg reflector

FWHM - full width at half maximum

FX - free exciton

LP - lower polariton

LX - localized exciton

MBE - molecular beam epitaxy

MC - microcavity

MOVPE - metalorganic vapour phase epitaxy

PL - photoluminescence

QCSE - quantum confined Stark effect

QW - quantum well

TR - time resolved

TI - time integrated

UHV - ultrahigh vacuum

UP - upper polariton

UV - ultraviolet

VBO - valence band offset

VCSEL - vertical cavity surface emitting laser

X - exciton

X_A - *A* exciton

X_B - *B* exciton

References

[1] C. Weisbuch, M. Nishioka, A. Ishikawa, and Y. Arakawa, Phys. Rev. Lett. **69**, 3314 (1992).

[2] R. Houdré, R. P. Stanley, and M. Ilegems, Phys. Rev. A **53**, 2711 (1996).

[3] R. Houdré, C. Weisbuch, R. P. Stanley, U. Oesterle, P. Pellandini, and M. Ilegems, Phys. Rev. Lett. **73**, 2043 (1994).

[4] V. Savona, L. C. Andreani, P. Schwendimann, and A. Quattropani, Solid State Commun. **93**, 733 (1995).

[5] R. P. Stanley, S. Pau, U. Oesterle, R. Houdré, and M. Ilegems, Phys. Rev. B **55**, R4867 (1997).

[6] R. P. Stanley, R. Houdré, C. Weisbuch, U. Oesterle, and M. Ilegems, Phys. Rev. B **53**, 10995 (1996).

[7] F. Tassone, C. Piermarocchi, V. Savona, A. Quattropani, and P. Schwendimann, Phys. Rev. B **56**, 7554 (1997).

[8] F. Tassone, C. Piermarocchi, V. Savona, A. Quattropani, and P. Schwendimann, Phys. Rev. B **53**, R7642 (1996).

[9] J. Bloch, and J. Y. Marzin, Phys. Rev. B **56**, 2103 (1997).

[10] M. Muller, J. Bleuse, and R. André, Phys. Rev. B **62**, 16886 (2000).

[11] J. Wainstain, C. Delalande, D. Gendt, M. Voss, J. Bloch, V. Thierry-Mieg, and R. Planel, Phys. Rev. B **58**, 7269 (1998).

[12] B. Sermage, S. Long, I. Abram, J. Y. Marzin, J. Bloch, R. Planel, and V. Thierry-Mieg, Phys. Rev. B **53**, 16516 (1996).

[13] J. Bloch, V. Thierry-Mieg, R. Planel, B. Sermage, S. Long, and I. Abram, Solid State Electronics **40**, 487 (1996).

[14] A. Imamoglu, R. J. Ram, S. Pau, and Y. Yamamoto, Phys. Rev. A **53**, 4250 (1996).

[15] M. Saba, C. Cuiti, J. Bloch, V. Thierry-Mieg, R. André, L. S. Dang, S. Kundermann, A. Mura, G. Biongiovanni, J. L. Stadehli, and B. Deveaud, Nature (London) **414**, 731 (2001).

[16] P. G. Savvidis, J. J. Baumberg, R. M. Stevenson, M. S. Skolnick, D. M. Whittaker, and J. S. Roberts, Phys. Rev. Lett. **84**, 1547 (2000).

[17] F. Tassone and Y. Yamamoto, Phys. Rev. B **59**, 10830 (1999).

[18] A. I. Tartakovskii, M. Emam-Ismail, R. M. Stevenson, M. S. Skolnick, V. N. Astratov, D. M. Whittaker, J. J. Baumberg, and J. S. Roberts, Phys. Rev. B **62**, R2283 (2000).

[19] R. Butté, G. Delalleau, A. I. Tartakovskii, M. S. Skolnick, V. N. Astratov, J. J. Baumberg, G. Malpuech, A. Di Carlo, A. V. Kavokin, and J. S. Roberts, Phys. Rev. B **65**, 205310 (2002).

[20] D. Bajoni, P. Senellart, A. Lemaître, and J. Bloch, Phys. Rev. B **76**, 201305(R) (2007).

[21] A. I. Tartakovskii, D. N. Krizhanovskii, G. Malpuech, M. Emam-Ismail, A. V. Chernenko, A. V. Kavokin, V. D. Kulakovskii, M. S. Skolnick, and J. S. Roberts, Phys. Rev. B **67**, 165302 (2003).

[22] D. Bajoni, P. Senellart, E. Wertz, I. Sagnes, A. Miard, A. Lemaître, and J. Bloch, Phys. Rev. Lett. **100**, 047401 (2008).

[23] L. S. Dang, D. Heger, R. André, F. Bouef, and R. Romestain, Phys. Rev. Lett. **81**, 3920 (1998).

[24] J. Kasprzak, M. Richard, S. Kundermann, A. Baas, P. Jeambrun, J. M. J. Keeling, F. M. Marchetti, M. H. Szymańska, R. André, J. L. Staehli, V. Savona, P. B. Littlewood, B. Deveaud, and L. S. Dang, Nature (London) **443**, 409 (2006).

[25] P. Bigenwald, A. Kavokin, B. Gil, and P. Lefebvre, Phys. Rev. B **61**, 15621 (2000).

[26] G. Malpuech, A. Di Carlo, A. Kavokin, J. J. Baumberg, M. Zamfirescu, and P. Lugli, Appl. Phys. Lett. **81**, 412 (2002).

[27] S. Nakamura, G. Fasol, and S. J. Pearton, *The Blue Laser Diode: The Complete Story*, 2nd ed. (Springer, Berlin, 2000).

[28] S. F. Chichibu, A. Uedono, T. Onuma, B. A. Haskell, A. Chakraborty, T. Koyama, P. T. Fini, S. Keller, S. P. DenBaars, J. S. Speck, U. K. Mishra, S. Nakamura, S. Yamaguchi, S. Kamiyama, H. Amano, I. Akasaki, J. Han, and T. Sota, Nat. Mater. **5**, 810 (2006).

[29] S. F. Chichibu, A. Uedono, T. Onuma, T. Sota, B. A. Haskell, S. P. DenBaars, J. S. Speck, and S. Nakamura, Appl. Phys. Lett. **86**, 021914 (2005).

[30] R. Houdré, Phys. Stat. Sol. B **242**, 2167 (2005).

[31] H. Teisseyre, C. Skierbiszewski, B. Łucznik, G. Kamler, A. Feduniewicz, M. Siekacz, T. Suski, P. Perlin, I. Grzegory, and S. Porowski, Appl. Phys. Lett. **86**, 162112 (2005).

[32] A. Morel, P. Lefebvre, S. Kalliakos, T. Taliercio, T. Bretagnon, and B. Gil, Phys. Rev. B **68**, 045331 (2003).

[33] I. Vurgaftman and J. R. Meyer, J. Appl. Phys. **94**, 3675 (2003).

[34] F. Bernardini, V. Fiorentini, and D. Vanderbilt, Phys. Rev. B **56**, R10024 (1997).

[35] P. Y. Yu and M. Cardona, *Fundamentals of Semiconductors* (Springer, 1994).

[36] C. F. Klingshirn, *Semiconductor Optics*, (Springer, 1995).

[37] M. Suzuki and T. Uenoyama, *Group III Nitride Semiconductor Compounds*, edited by B. Gil (Clarendon, Oxford 1998).

[38] A. V. Rodina, M. Dietrich, A. Göldner, L. Eckey, A. Hoffman, Al. L. Efros, M. Rosen, and B. K. Meyer, Phys. Rev. B **64**, 115204 (2002).

[39] S. Chichibu, T. Azuhata, T. Sota, and S. Nakamura, J. Appl. Phys. **79**, 2784 (1996).

[40] M. Tchounkeu, O. Briot, B. Gil, J. P. Alexis, and R.-L. Aulombard, J. Appl. Phys. **80**, 5352 (1996).

[41] D. Volm, K. Oettinger, T. Streibl, D. Kovalev, M. Ben-Chorin, J. Diener, B. K. Meyer, J. Majewski, L. Eckey, A. Hoffman, H. Amano, I. Akasaki, K. Hiramatsu, and T. Detchprohm, Phys. Rev. B **53**, 16543 (1996).

[42] K. Kornitzer, T. Ebner, K. Thonke, R. Sauer, C. Kirchner, V. Schwegler, M. Kamp, M. Leszczynski, I. Grzegory, and S. Porowski, Phys. Rev. B **60**, 1471 (1999).

[43] S. Rudin, T. L. Reinecke, and B. Segall, Phys. Rev. B **42**, 11218 (1990).

[44] C. Weisbuch and B. Vinter, *Quantum Semiconductor Structures* (Academic Press, 1991).

[45] G. Bastard, Phys. Rev. B **24**, 5693 (1981); G. Bastard, Phys. Rev. B **25**, 7594 (1982).

[46] E. O. Kane, J. Phys. Chem. Solids **1**, 249 (1957).

[47] S. R. White and L. S. Sham, Phys. Rev. Lett. **47**, 879 (1981).

[48] F. Bernardini and V. Fiorentini, Phys. Rev. B **57**, R9427 (1998).

[49] F. A. Ponce in *GaN and Related Materials*, edited by S. J. Pearton (Gordon and Breach Science Publishers, 1997).

[50] S. D. Lester, F. A. Ponce, M. G. Craford, and D. A. Steigerwald, Appl. Phys. Lett. **66**, 1249 (1995).

[51] S. Chichibu, T. Azuhata, T. Sota, and S. Nakamura, Appl. Phys. Let. **69**, 4188 (1996).

[52] M. Osinski, P. Perlin, P. G. Eliseev, J. Lee, and V. Smagley, J. Cryst. Growth **189/190**, 803 (1998).

[53] F. Della Sala, A. Di Carlo, P. Lugli, F. Bernardini, V. Fiorentini, R. Scholz, and J.-M. Jancu, Appl. Phys. Lett. **74**, 2002 (1999).

[54] O. Svelto, *Priciples of Lasers* (Springer, 1998).

[55] E. Hecht, *Optics* (2nd Ed., Addison Wesley, 1987).

[56] N. Antoine-Vincent, F. Natali, M. Mihailovic, A. Vasson, J. Leymarie, P. Disseix, D. Byrne, F. Semond, and J. Massies, J. Appl. Phys. **93**, 5222 (2003).

[57] J. Humlicek, M. Garriga, M. I. Alonso, and M. Cordona, J. Appl. Phys. **65**, 2827 (1989).

[58] P. Yeh, *Optical Waves in Layered Media* (Wiley, New York, 1988).

[59] S. Pau, G. Björk, J. Jacobson, H. Cao, and Y. Yamamoto, Phys. Rev. B **51**, 14437 (1995).

[60] M. S. Skolnick, T. A. Fisher, and D. M. Whittaker, Semicond. Sci. Technol. **13**, 645 (1998).

[61] G. Panzarini, L. C. Andreani, A. Armitage, D. Baxter, M. S. Skolnick, V. N. Astratov, J. S. Roberts, A. V. Kavokin, M. R. Vladimirova, and M. A. Kaliteevski, Phys. Rev. B **59**, 5082 (1999).

[62] R. Houdré, R. P. Stanley, O. Oesterle, M. Ilegems, and C. Weisbuch, Journal de Physique IV **3**, 51 (1993).

[63] Y. Zhu, D. J. Gauthier, S. E. Morin, Q. Wu, H. J. Carmichael, and T. M. Mossberg, Phys. Rev. Lett. **64**, 2499 (1990).

[64] R. Butté, G. Christmann, E. Feltin, J.-F. Carlin, M. Mosca, M. Ilegems, and N. Grandjean, Phys. Rev. B **73**, 033315 (2006).

[65] J. J. Hopfield, Phys. Rev. **112**, 1555 (1958).

[66] B. Gil, Superlattices Microstruct. **43**, 408 (2008).

[67] I. R. Sellers, F. Semond, M. Leroux, J. Massies, M. Zamfirescu, F. Stokker-Cheregi, M. Gurioli, A. Vinattieri, and M. Colocci, Phys. Rev. B **74**, 193308 (2006).

[68] A. Einstein, Sitzunberg. Preuss. Akad. Wiss. **1925**, 3 (1925).

[69] P. Littlewood, P. Eastham, J. Keeling, F. Marchetti, and M. Szymanska, J. Phys.: Cond. Matt. **16**, 3597 (2004).

[70] G. Malpuech, Y. Rubo, F. Laussy, P. Bigenwald, and A. Kavokin, Semicond. Sci. Technol. **18**, S395 (2003).

[71] C. R. Abernathy in *GaN and Related Materials*, edited by S. J. Pearton (Gordon and Breach Science Publishers, 1997).

[72] K. Motoki, T. Okahisa, N. Matsumoto, M. Matsushima, H. Kimura, H. Kasai, K. Takemoto, K. Uematsu, T. Hirano, M. Nakayama, S. Nakahata, M. Ueno, D. Hara, Y. Kumagai, A. Koukitu, and H. Seki, Jpn. J. Appl. Phys. **40**, L140 (2001).

[73] H. Ibach and H. Lüth, *Solid-State Physics* (Springer Verlag, 2003).

[74] N. Grandjean, J. Massies, and M. Leroux, Appl. Phys. Lett. **74**, 2361 (1999).

[75] G. D. Chen, M. Smith, J. Y. Lin, H. X. Jiang, Su-Huai Wei, M. Asif Khan, and C. J. Sun, Appl. Phys. Lett. **68**, 2784 (1996).

[76] E. Kuokstis, C. Q. Chen, M. E. Gaevski, W. H. Sun, J. W. Yang, G. Simin, M. A. Khan, H. P. Maruska, D. W. Hill, M. C. Chou, J. J. Gallagher, and B. Chai, Appl. Phys. Lett. **81**, 4130 (2002).

[77] M. D. Craven, P. Waltereit, J. S. Speck, and S. DenBaars, Appl. Phys. Lett. **84**, 496 (2004).

[78] M. Zamfirescu, B. Gil, N. Grandjean, G. Malpuech, A. Kavokin, P. Bigenwald, and J. Massies, Phys. Rev. B **64**, 121304 (2001).

[79] S. Chichibu, T. Azuhata, T. Sota, and S. Nakamura, Appl. Phys. Lett. **70**, 2822 (1996).

[80] J. Li, K. B. Nam, K. H. Kim, J. Y. Lin, and H. X. Jiang, Appl. Phys. Lett. **78**, 61 (2001).

[81] T. Takeuchi, H. Amano, K. Hiramatu, N. Sawaki, and I. Akasaki, J. Cryst. Growth **115**, 634 (1991).

[82] S. Guha and N. A. Bojarczuk, Appl. Phys. Lett. **72**, 415 (1998).

[83] F. Semond, B. Damilano, S. Vézian, N. Grandjean, M. Leroux, and J. Massies, Appl. Phys. Lett. **75**, 82 (1999).

[84] B. Monemar, J. P. Bergman, and I. A. Buyanova in *GaN and Related Materials*, edited by S. J. Pearton (Gordon and Breach Science Publishers, 1997).

[85] D. C. Reynolds, D. C. Look, W. Kim, Ö. Aktas, A. Botchkarev, A. Salvador, H. Morkoç, and D. N. Talwar, J. Appl. Phys. **80**, 594 (1996).

[86] B. Gil, O. Briot, and R. L. Aulombard, Phys. Rev. B **52**, R17028 (1995).

[87] B. Gil, F. Hamdani, and H. Morkoç, Phys. Rev. B **54**, 7678 (1996).

[88] A. Shikanai, T. Azuhata, T. Sota, S. Chichibu, A. Kuramata, K. Horino, and S. Nakamura, J. Appl. Phys. **81**, 417 (1997).

[89] W. R. L. Lambrecht, B. Segall, J. Rife, W. R. Hunter, and D. K. Wickenden, Phys. Rev. B **51**, 13516 (1995).

[90] T. Kawashima, H. Yoshikawa, S. Adachi, S. Fuke, and K. Ohtsuka, J. Appl. Phys. **82**, 3528 (1997).

[91] J. Shah, *Ultrafast Spectroscopy of Semiconductors and Semiconductor Nanotrusctures* (Springer, 1996).

[92] B. H. Armstrong, J. Quant. Spectrosc. Radiat. Transfer **7**, 61 (1967).

[93] P. S. Zory, *Quantum Well Lasers* (Academic Press, 1993).

[94] S. J. Pearton, *GaN and Related Materials* (Gordon and Breach Science Publishers, 1997).

[95] J. P. Wittke, RCA Review **36**, 655 (1975).

[96] D. J. Heinzen, J. J. Childs, J. E. Thomas, and M. S. Feld, Phys. Rev. Lett. **58**, 1320 (1987).

[97] G. B. Stringfellow, *Organometallic Vapor-Phase Epitaxy: Theory and Practice*, 2nd ed. (Academic Press, 1999).

[98] E. D. Palik. *Handbook of Optical Constants of Solids* (Academic Press, 1998).

[99] T. A. Figher, A. M. Afshar, D. M. Whittaker, M. S. Skolnick, J. S. Roberts, G. Hill, and M. A. Pate, Phys. Rev. B **51**, 2600 (1995).

[100] J. P. Reithmaier, G. Sek, A. Loffler, C. Hofmann, S. Kuhn, S. Reitzenstein, L. V. Keldysh, V. D. Kulakovskii, T. L. Reinecke, and A. Forchel, Nature **432**, 197 (2004).

[101] E. Peter, P. Snellart, D. Martrou, A. Lemaître, J. Hours, J.-M. Gérard, and J. Bloch, Phys Rev. Lett. **95**, 067401 (2005).

[102] D. Solnyshkov and G. Malpuech, Superlattices Microstruct. **41**, 279 (2007).

[103] E. Feltin, D. Simeonov, J.-F. Carlin, R. Butté, and N. Grandjean, Appl. Phys. Lett. **90**, 021905 (2007).

[104] D. J. Lovering, R. T. Phillips, G. J. Denton, and G. W. Smith, Phys. Rev. Lett. **68**, 1880 (1992).

[105] R. T. Phillips, D. J. Lovering, G. J. Denton, and G. W. Smith, Phys. Rev. B **45**, 4308 (1992).

[106] J. C. Kim, D. R. Wake, and J. P. Wolfe, Phys. Rev. B **50**, (1994).

[107] F. Kreller, M. Lowisch, J. Puls, and F. Henneberger, Phys. Rev. Lett. **75**, 2420 (1995).

[108] Y. Yamada, T. Mishina, Y. Masumoto, Y. Kawasaki, S. Yamaguchi, K. Ichino, S. Fujita, and T. Taguchi, Supperlattices Microstruct. **15**, 33 (1994).

[109] J. Puls, V. V. Rossin, F. Kreller, H. J. Wunsche, S. Renisch, N. Hoffmann, M. Rabe, and F. Henneberger, J. Cryst. Growth **159**, 784 (1996).

[110] W. Langbein and J. M. Hvam, Phys. Rev. B **59**, 15405 (1999).

[111] V. Fiorentini, F. Bernardini, F. Della Salla, A. Di Carlo, and P. Lugli, Phys. Rev. B **60**, 8849 (1999).

[112] G. Kocherscheidt, W. Langbein, U. Woggon, V. Savona, R. Zimmermann, D. Reuter, and A. D. Wieck, Phys. Rev. B **68**, 085207 (2003).

[113] M. Gurioli, F. Bogani, S. Ceccherini, and M. Colocci, Phys. Rev. Lett. **78**, 3205 (1997).

[114] Y. Masumoto, S. Shionoya, and H. Kawaguchi, Phys, Rev. B **29**, 2324 (1984).

[115] D. S. Citrin, Phys. Rev. B **50**, 17655 (1994).

[116] A. L. Ivanov, H. Haug, and L. V. Keldysh, Phys. Rep. **296**, 237 (1998).

[117] W. Langbein and J. M. Hvam, Phys. Rev. B **61**, 1692 (2000).

[118] C. H. Chia, T. Makino, K. Tamura, Y. Segawa, M. Kawasaki, A. Ohmoto, and H. Koinuma, Appl. Phys. Let. **82**, 1848 (2003).

[119] N. Grandjean, B. Damilano, S. Dalmasso, M. Leroux, M. Laügt, and J. Massies, J. Appl. Phys. **86**, 3714 (1999).

[120] M. Leroux, N. Grandjean, M. Laügt, J. Massies, B. Gil, P. Lefebvre, and P. Bigenwald, Phys. Rev. B **58**, R13371 (1998).

[121] A. Thilagam, Phys. Rev. B **56**, 4665 (1997).

[122] P. Bigenwald, P. Lefebvre, T. Bretagnon, and B. Gil, Phys. Stat. Sol. B **216**, 371 (1999).

[123] C. Brimont, M. Gallart, O. Crégut, B. Hönerlage, and P. Gilliot, Phys. Rev. B **77**, 125201 (2008).

[124] M. Auf der Maur, M. Povolotski, F. Sacconi, and A. Di Carlo, Superlattices Microstruct. **41**, 381 (2007).

[125] TiberCAD simulation package, http://www.tibercad.org.

[126] M. Povolotski and A. Di Carlo, J. Appl. Phys. **100**, 063514 (2006).

[127] S. L. Chuang and C. S. Chang, Phys. Rev. B **54**, 2491 (1996).

[128] S. Christopoulos, G. Baldassarri Höger von Högersthal, A. J. D. Grundy, P. G. Lagoudakis, A. V. Kavokin, J. J. Baumberg, G. Christmann, R. Butté, E. Feltin, J.-F. Carlin, and N. Grandjean, Phys. Rev. Lett. **98**, 126405 (2007).

[129] G. Christmann, R. Butté, E. Feltin, J.-F. Carlin, N. Grandjean, Appl. Phys. Lett. **93**, 051102 (2008).